GENE DUPLICATION AND FUSION: STRATEGY FOR ACTIVE SITE CONTROL AND STARTING POINT FOR NEW CATALYSTS

by

Yu Wang

A dissertation submitted to the Graduate Faculty of
Auburn University
in partial fulfillment of the
requirements for the Degree of
Doctor of Philosophy

Auburn, Alabama
Dec 8, 2012

Keywords: catalase-peroxidase, KatG, folding platform, heme protein,
C-terminal domain, gene duplication and fusion

Approved by

Douglas Goodwin, Chair, Professor of Biochemistry
Holly Ellis, Professor of Biochemistry
Evert Duin, Professor of Biochemistry
Christian Goldsmith, Professor of Chemistry

Abstract

Catalase–peroxidases (KatGs) have two peroxidase-like domains. The N-terminal domain contains the heme-dependent, bifunctional active site. Though the C-terminal domain lacks the ability to bind heme or directly catalyze any reaction, it has been proposed to serve as a platform to direct the folding of the N-terminal domain. Toward such a purpose, its I′-helix is highly conserved and appears at the interface between the two domains. Single and multiple substitution variants targeting highly conserved residues of the I′-helix were generated for intact KatG as well as the stand-alone C-terminal domain ($KatG^C$). Single variants of intact KatG produced only subtle variations in spectroscopic and catalytic properties of the enzyme. However, the double and quadruple variants showed spectroscopic and catalytic properties similar to that observed for the N-terminal domain on its own ($KatG^N$). The analogous variants of $KatG^C$ showed a much more profound loss of function as evaluated by their ability to return $KatG^N$ to its active conformation. These results suggest that the I′-helix is central to direct structural adjustments in the adjacent N-terminal domain. In particular, substitution of E695, a strictly conserved residue of the I'helix was especially destructive to KatG active site integrity. Available structures of KatG indicate that E695 is a central component of several hydrogen-bonded networks that also include strictly conserved R126 and W159 from the adjacent N-terminal domain. Both W159 (N-terminus of the D-helix) and R126 (BC helical connecting loop) are part of core structures of the peroxidase-like N-terminal domain with connections to the active site. This points to a potential connection between the I'-helix and its influence on active site conformation and function. To

evaluate this hypothesis, we replaced R126, W159 and E695 with alanine, singly and in combination, not only for intact KatG, but also for the stand-alone $KatG^N$ or $KatG^C$, as appropriate. Single variants of intact KatG showed a substantial loss of stability, particularly at the active site. The analogous variants of $KatG^C$ and $KatG^N$ showed a profound loss of function as evaluated by the return $KatG^N$ (or its variants) to a functional conformation, suggesting C-terminal domain through these interactions directs active site structural adjustments that are essential for catalytic function in the active site 25 Å away. The C-terminal domain not only directs conformational adjustments in its N-terminal domain partner, but due to its origin from gene duplication, also still retains the helical architecture of a typical peroxidase active site. This site lacks the residues necessary for catalytic activity or even heme binding. As such, the C-terminal domain appears to provide an ideal "blank slate" for engineering new heme-dependent catalysts. Spectroscopic measurements showed that a M616G/R617H variant of $KatG^C$ was sufficient to restore heme binding, producing a hexacoordinate low-spin ferric state. Additional modifications produced spectra very similar to those observed for $KatG^N$.

Acknowledgments

The research conducted in this dissertation would not have been possible without the help and support of many people whom I wish to thank. Listed here are only a few of those. First, I would like to thank my advisor Dr. Douglas Goodwin. He guided me through my whole research, trained me to be an independent researcher. He had a significant influence on my future career and personal life. To me he is more than an advisor; without his encouragement, I could not have reached today's achievement. I wish I will continue to make him proud. Second, I would like to thank Dr. Holly Ellis for taking the time to review every manuscript I have written. Dr. Evert Duin has been of great assistance with EPR. Third, I would like thank all my co-workers at Auburn University, especially Robert Moore and Carma Cook. They provided great help and assistance when I first started my research. I also feel lucky to have worked with Shalley Kudalkar, Ellizebeth Ngwane and Haijun Duan. Especially I thank my family for their continuous understanding, help, support and encouragement for these five years. Finally, I would like to thank NSF, the Department of Chemistry and Biochemistry, Auburn University's graduate school, and COSAM for their funding support.

Table of Contents

List of Figures

List of Tables

CHAPTER ONE

LITERATURE REVIEW

The central proposes of the research described in this dissertation are to evaluate the role of the C-terminal domain in catalase-peroxidase (KatG) enzymes, and to borrow this structure as a template for engineering new heme-dependent catalysts. The two-domain structure of KatG is a novel feature in comparison to other members of its superfamily as is its bifunctional catalytic capability. The connection between KatG's structure and its function remains poorly defined, but its contrast against other structurally similar but functionally distinct relatives, provides an excellent opportunity to evaluate the mechanism by which structures peripheral to and distant from an active site influence structure and function. More than this, it affords an ideal system to apply the information and strategy toward engineering new heme enzymes. This chapter will first establish the importance of catalases and peroxidases in nature, and then discuss the catalytic mechanisms employed by these H_2O_2-degrading enzymes by comparing their structures and functions in order to understand the importance of the two-domain structure, bifunctionality and molecular phylogeny of the catalase-peroxidases. Furthermore, discussion focused on the structure and function relationships of various heme-dependent peroxidases will shed light on the structural basis and strategy for engineering the KatG C-terminal domain to a new heme-dependent catalyst, building on its unique origin and features.

1.1 Hydrogen peroxide and its scavengers in cells:

Hydrogen peroxide is one of the most common reactive oxygen species that aerobic organisms encounter. For example, in well-fed aerobic *E.coli* cells, H_2O_2 is formed at a constant rate of 10-15 μM/s [1]. This endogenous H_2O_2 is primarily formed from reduction of O_2 by flavoproteins [2]. Exogenous H_2O_2 derived from environmental sources is also an issue because H_2O_2 can penetrate cell membranes. Exogenous sources of H_2O_2 include the NADPH oxidase-based response of plants and animials to infection, H_2O_2-excreting microbes, extracellular oxidation at anoxic/oxic interfaces, and photochemically-driven oxidations [2]. Due to its ability to initiate damage to biomolecules, excessive H_2O_2 is toxic for living cells. In particular, it can destroy iron-sulfur proteins involved in energy production and biosynthesis [3], and deactivate other enzymes that rely on ferrous iron as a cofactor [4]. The reduction of H_2O_2 by ferrous iron produces the highly reactive hydroxyl radical (·OH) by the well-known Fenton reaction. The unregulated generation of such a reactive oxidant is known to result in damage to all classes of biological molecules. Therefore, rapid and efficient removal of excess H_2O_2 is essential for all organisms that are to survive in an aerobic enviornment. In most organisms, H_2O_2 is scavenged by peroxidases and/or catalases. The latter show a striking ability to disproportionate H_2O_2 to water concomitant with the generation of dioxygen, according to reaction **(1)**. Enzymes with catalase activity are predominantly found in three gene families: typical (i.e., monofunctional) catalases, catalase-peroxidases (KatGs), and manganese (non-heme) catalases [5]. Among these, the large majority are heme-containing enzymes, and these are widely distributed among prokaryotes and eukaryotes. Manganese catalase is a minor gene group only present in bacteria; they are less proficient catalysts than typical catalases and catalase-peroxidases [5]. Though important, the manganese catalases are not particularly relevant to this discussion and will not be

covered further.

$$2\,H_2O_2 \longrightarrow O_2 + 2\,H_2O \qquad (1)$$

1.2 Typical (i.e., monofunctional) catalases:

Phylogenetic analyses indicate that there are three main evolutionary clades, which were segregated in an early stage of evolution by way of several gene-duplication events [5, 6]. Clade 1 catalases are small-subunit proteins with heme *b* as the prosthetic group. They are distributed among bacteria, algae and plants. Clade 2 contains the large-subunit catalases, and these primarily use heme *d* as prosthetic group and contain an additional "flavodoxin-like" domain. These are widely distributed among bacteria and fungi. Clade 3 is the most widely distributed; being abundant in archaebacteria, fungi, protists, plants and animals. These are typically small-subunit catalases that contain heme *b* and NADPH as cofactors.

1.2.1 Structure and active site of monofunctional catalases:

The monofunctional catalase from *E. coli,* hydroperoxidase II (HPII), is a tetrameric large-subunit catalase (Fig. 1.1A) found in clade 2 of the typical catalase family. Available crystal structures indicate that HP II is composed of five different tertiary structural regions or domains, including 1) the amino terminal arm, 2) an antiparallel eight-stranded β-barrel, 3) an extended wrapping loop, 4) a helical domain, and 5) a C-terminal, flavodoxin-like domain [7]. The core of the protein is similar in structure and sequence to those of small subunit catalases; however the 75-80 residues of the amino-terminal arm and the flavodoxin-like domain are unique to HPII and other clade 2 enzymes (Fig. 1.1B). It has been proposed that both structural elements are dedicated to facilitating the folding and oligomerization process [7, 8].

Although significant differences exist in the overall folding between small- and large-subunit catalases, the active site residues are strictly conserved among all three clades (Fig. 1.1C) [5]. These include Asn 201 and His 128 (HPII numbering) in the distal site, and Tyr 415, which ligates the iron on the heme's proximal side. Asn 201 is proposed to stabilize the peroxide [9]. The imidazole ring of His 128 is situated 3.5 Å above and parallel to the plane of the heme, allowing for an H-bond with a conserved Ser 167 [7, 10]. The coplanar position of the imidazole ring contrasts with the perpendicular orientation of this group in peroxidases. This is proposed to allow the second oxygen of the peroxide to form an H-bond with the imidazole during catalysis, facilitating O_2 production [5]. In all monofunctional catalases, a tyrosine has been identified as the proximal heme iron ligand in contrast to a histidine in plant peroxidases. The strong anionic character of the ligand is expected to favor the oxidized heme species [11]. Interestingly, a unique feature for *E. coli* HPII is a covalent bond between the proximal Tyr ligand and an adjacent imidazole ring from His 392 [12]. This has been proposed to enhance resistance to peroxide-dependent deactivation by preventing formation of compound II, an intermediate that is not part of the enzyme's catalytic cycle [5].

Another feature typical of monofunctional catalases is a long, narrow substrate access channel leading to the deeply buried active site heme group [7]. In contrast, typical peroxidases usually provide more open access to the heme cofactor. In *E.coli* HPII, two major channels can be defined: one has small diameter and is full of hydrophobic residues, leading H_2O_2 to the heme distal pocket; the other is a large funnel-shaped opening positioned near residues 590 and 595 and leads to the vicinity of Asn 201 [7]. The shape and size of these channels are essential for selectively directing substrates, particularly H_2O_2, to the active site [7, 13].

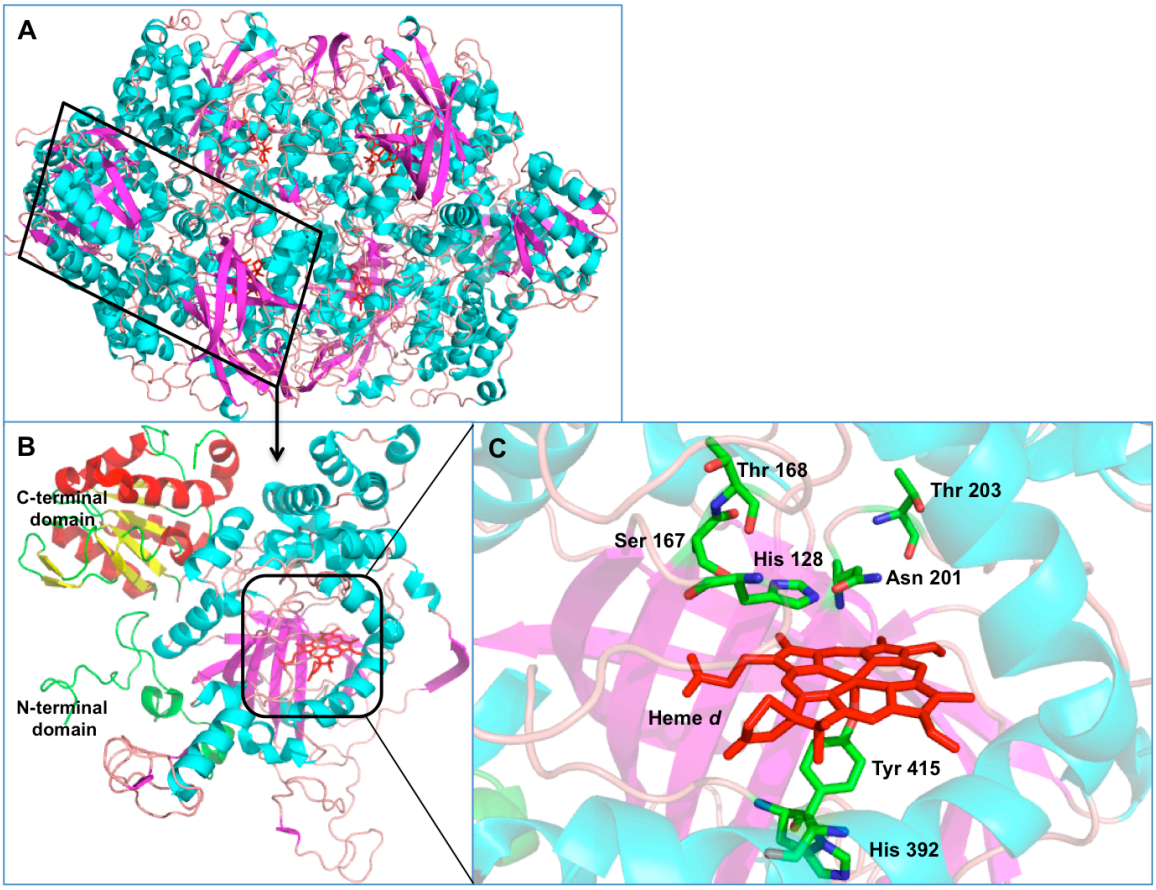

Figure 1.1: Overall structure (A), one subunit (B) and the active site (C) of the *E.coli* catalase (HP II) (PDB: 1GGE).

1.2.2 The catalytic mechanism of typical catalases:

The catalase cycle starts with the oxidation of the heme iron along with the heterolytic cleavage of the O-O bond of hydrogen peroxide. This process produces a ferryl-oxo porphyrin π-cation radical ([Por $^{\cdot}$+] Fe^{IV}=O) intermediate known as compound I with the concomitant production of a water molecule (Fig. 1.2) [9]. Kinetics studies [14] indicate that once compound I forms, it is rapidly and efficiently reduced back to the resting (i.e., ferric) enzyme by reacting with a second equivalent of H_2O_2, generating H_2O and O_2 [15]. Two mechanisms have been proposed for O_2 production and the return of the ferric state: 1) a His-mediated mechanism, or 2) a direct mechanism involving radical formation (Fig. 1.2) [16]. The radical mechanism posits a radical intermediate generated upon hydrogen atom transfer from H_2O_2 to the ferryl heme intermediate. This bears some resemblance to the mechanism proposed for alkane hydroxylation by cytochrome P450 [17]. In contrast, the His-mediated mechanism shows the participation of ionic species resulting from an initial proton abstraction carried out with the assistance of the distal His as the general base. A recent study of the catalase mechanism by QM/MM Car-Parrinello Metadynamics simulations highlight the key role of distal residues acting as an acid/base catalyst [15], lending credence to the His-mediated mechanism.

1.3 Peroxidases:

The first part of this section will be dedicated to the structure and function relationships of heme dependent peroxidases from all five different superfamilies/families where the activity is

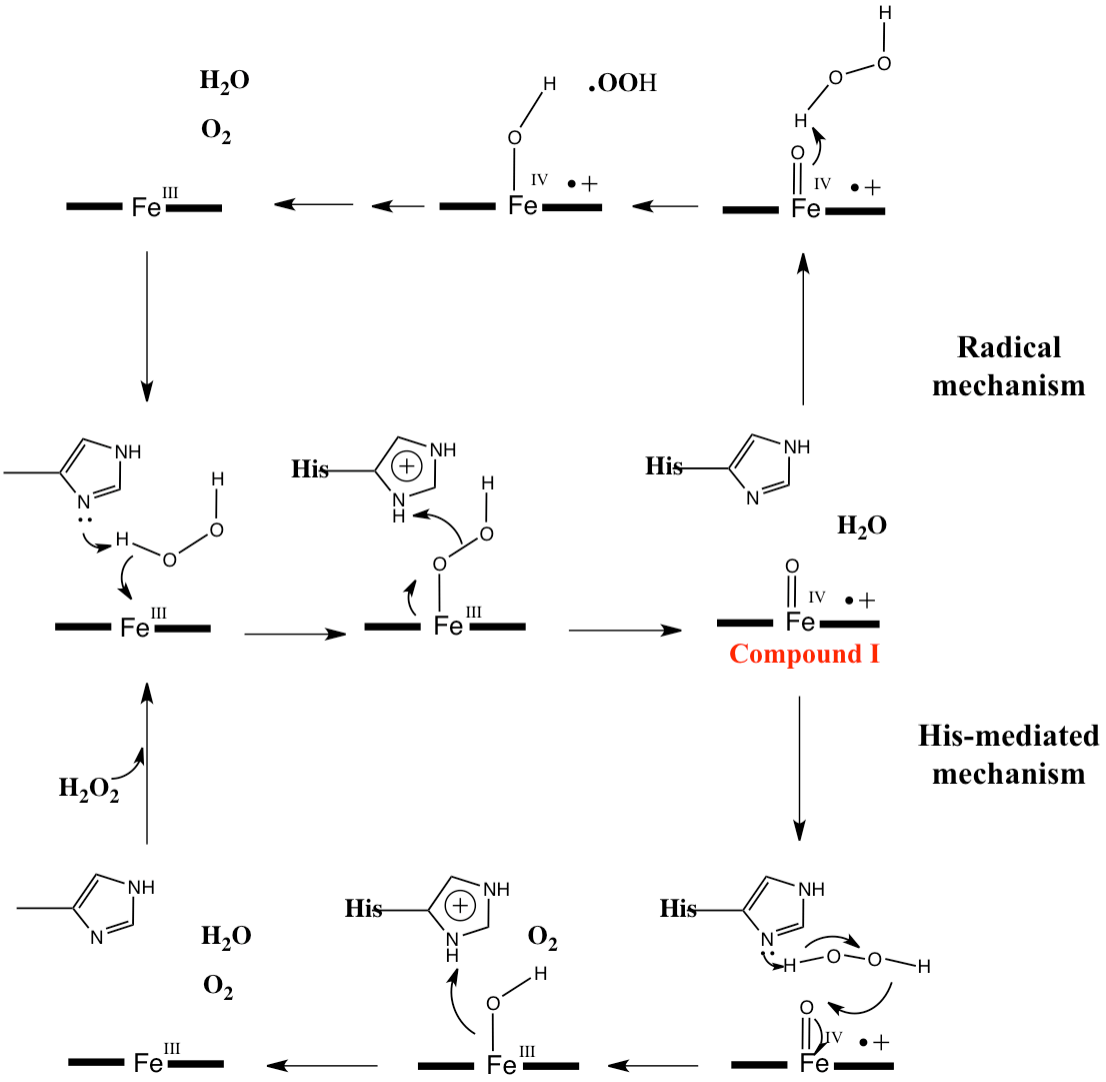

Figure 1.2: Catalytic mechanism of typical catalases.

found. Understanding these will provide a structural backdrop for understanding both the diversity and the commonalities of mechanisms and strategies by which heme-dependent peroxidase activity is accomplished. Because catalase-peroxidases (KatGs) fall into the peroxidase-catalase superfamily, the second part will progressively introduce members in this superfamily by discussing their phylogenic relationships and comparing their structures and functions with KatGs in order to understand the importance of the unique two-domain structure observed in KatGs. Together, these sections will lay the groundwork for evaluating the mechanisms by which the C-terminal domain modulates the conformation and performance of an active site that is sequestered in the N-terminal domain ≥ 30 Å away. They will also highlight strategies for using the stand-alone C-terminal domain as a scaffold for engineering new heme-dependent catalysts.

1.3.1 Systematic Classification of Peroxidases:

Peroxidases are capable of reducing H_2O_2 to water with the concomitant one- or two-electron oxidation of various organic and inorganic substrates according to reactions **(2)** and **(3)** [18]. Currently, 15 different Enzyme Commission (EC) numbers from **EC 1.11.1.1** to **EC 1.11.1.16** have been assigned to peroxidases [19]. Although there are heme and non-heme examples of peroxidases, the most abundant are those containing heme as the prosthetic group. As of January 2012 PeroxiBase (a database dedicated to cataloging genomic and other data on peroxidases), nearly 75% of all genes encoding enzymes with peroxidase activity are the heme-containing variety [20]. Traditionally, heme peroxidases have been divided into "plant" and "animal" groups, but the influx of new of genomic data has rendered such schemes obsolete. According to the current scheme, available heme peroxidase gene sequences are grouped

phylogenetically into three families (the di-heme peroxidases, the DyP-type peroxidases and the heme-haloperoxidases) and two superfamilies (the peroxidase-cyclooxygenase superfamily and the peroxidase-catalase superfamily) (Fig. 1.3) [21]. The majority of sequences fall into one of the two superfamilies, and the remaining sequences are distributed among the three families.

$$H_2O_2 + 2\,AH_2 \longrightarrow 2\,H_2O + 2\cdot AH \qquad (2)$$

$$H_2O_2 + X^- \longrightarrow H_2O + OX^- \qquad (3)$$

1.3.2 Di-heme peroxidases family:

1.3.2.1 Structure and function of di-heme peroxidases:

Representatives of this family are found predominantly in bacteria with some members found in achaea. A detailed phylogeny has been proposed based on sequence data available with most of the sequences derived from the di-heme cytochrome *c* peroxidases (DiHCcP) [21]. As the name suggests these enzymes contain two hemes. They are typically periplasmic where they catalyze reduction of hydrogen peroxide to water using single electron donors such as cytochrome c or cupredoxin [22]. Though DiHCcPs bear no sequential or topological resemblance to KatGs, all of them have been shown to be dimeric where each subunit (35-40 kDa) is composed of two domains [23], similar to the two-domain structure of KatGs. In contrast to KatGs where only one domain (the N-terminal domain) is catalytic active, both domains of DiHCcPs participate in catalytic events. There is an electron-transferring heme (E heme) domain and a peroxidatic heme (P heme) domain [23]. Both hemes are of the *c*-type in that they are covalently linked to the polypeptide chain by way of cysteine side chains [24]. In contrast, the

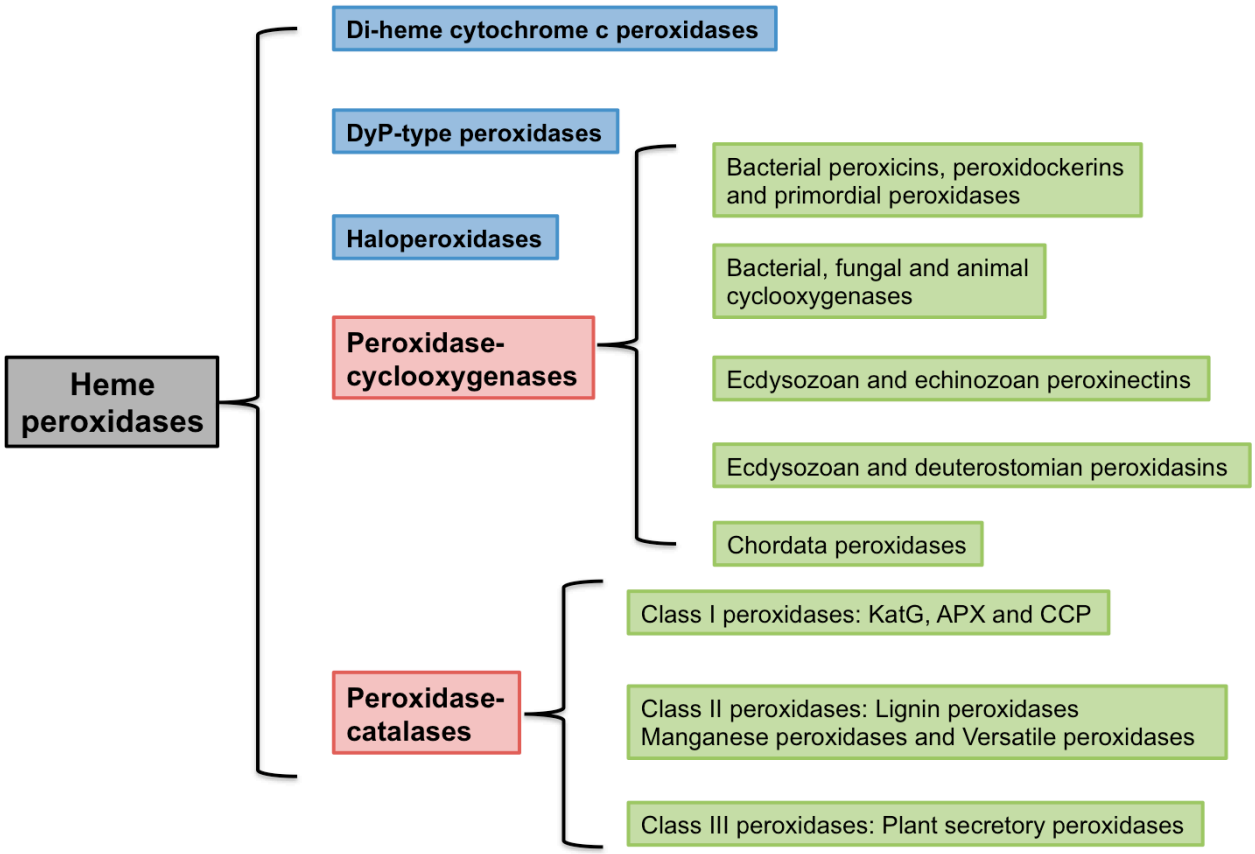

Figure 1.3: Overview of the classification of heme peroxidases (super) families.

canonical eukaryotic cytochrome *c* peroxidase (from the peroxidase-catalase superfamily) contains a single *b*-type heme in its active site.

The P heme is a low-potential center where H_2O_2 is reduced. The E heme is a high-potential center that serves to transfer electrons from soluble electron-shuttle proteins such as cytochrome *c* or azurin to the peroxidatic site [25-27]. The P heme is coordinated by two axial histidine ligands, whereas the E heme is ligated by one His and one Met residue [23, 24, 27-31]. Crystal structures of DiHCcP from *Pseudomonas aeruginosa* reveal that a single Ca^{2+} ion is tightly bound at the domain interface of both fully oxidized and mixed-valence forms of the enzyme. This Ca^{2+} is absolutely required for catalytic activity [23]. The role of the Ca^{2+} ion is unresolved, but it is proposed to maintain the structural integrity of the enzyme and/or modulate electron transfer between the two domains [23, 24, 27-31].

1.3.2.2 Catalytic cycle and heme function:

In most known bacterial DiHCcP enzymes, the inactive resting state can be converted to the active mixed-valence state by reduction of the E heme [32]. A mechanism proposed for the enzyme is shown in Fig. 1.4 [25]. The enzyme is isolated in an inactive state (state I) where both hemes are in a hexacoordinate ferric form. An electron (from ascorbate or the enzyme's physiological substrates) is transferred to the E heme (step A). E heme reduction triggers a Ca^{2+}-dependent conformational change (step B) that results in the removal of the distal histidine from the iron coordination sphere where it is replaced by a water molecule [26, 32, 33]. This produces the active form of the enzyme (state III). State III is then oxidized by H_2O_2 at the P heme producing a ferryl intermediate and a ferric E heme. This would be roughly analogous to the

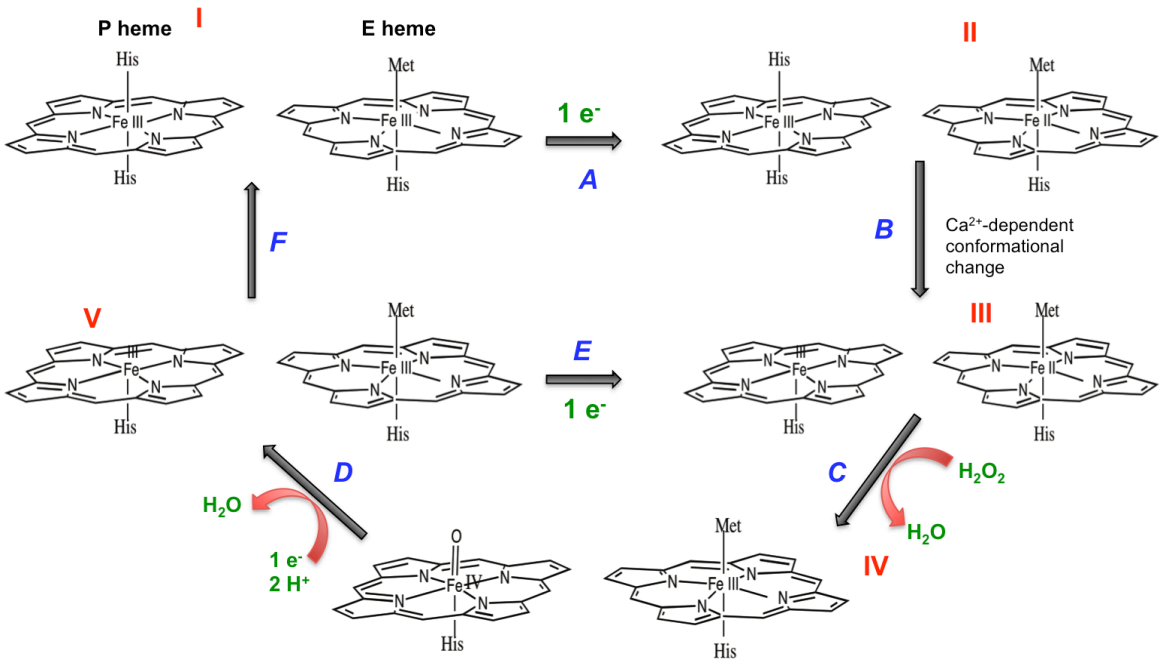

Figure 1.4: Catalytic cycle of bacterial diheme cytochrome *c* peroxidase.

compound I state of the monoheme peroxidases of eukaryotes (step C). The catalytic cycle is completed by the delivery of two electrons in single-electron steps (steps D and E) from cytochrome *c* or other substrates. Stage V is electronically equivalent to the resting enzyme, but its P heme is accessible to ligands. Relaxation back to the resting state is likely to be a slow process. It has been proposed that this step is only observed when insufficient reductant is present [32].

1.3.2.3 Enzyme structure and conformational changes during catalytic cycle:

As described earlier, the bacterial DiHCcP is composed of two heme-containing domains [23, 24, 27-31]. Both oxidized and mixed-valence forms of the enzyme share similar topological structures (Fig. 1.5). In the E heme-containing domain, the coordination of the heme remains unchanged by oxidation state. Conversely, the changes of the orientation of heme D-ring propionate group leads to a loss of an H-bond with the Leu 216, and in the mixed-valence state, Leu 216 moves away from the proximal heme site. The A-ring propionate group linked to Ca^{2+} ion does not change under activation. In the P heme-containing domain, more dramatic changes occur during activation. The loop carrying His 71 moves toward the dimer interface concomitant with relocation of the aromatic side chain of Trp 73. The movement of this loop allows for the occupation of peroxidatic site by a water molecule, and the introduction of two other conserved residues Gln 104 and Glu 114, which have been suggested to play critical roles in the formation and stabilization of the oxy-ferryl intermediate [23, 27].

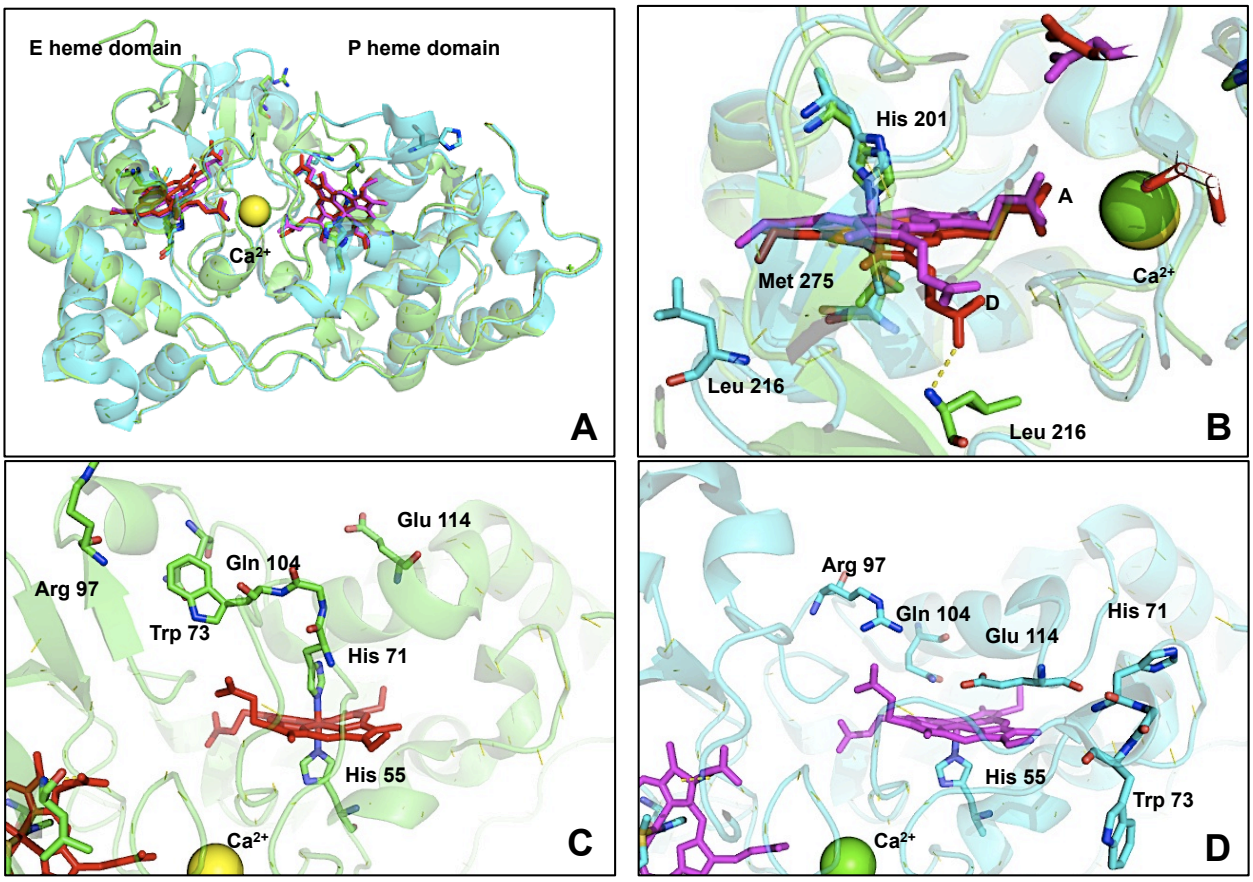

Figure 1.5: Structure of di-heme-cytochrome *c* peroxidase and conformational changes during catalysis.

The overall structure of di-heme cytochrome *c* peroxidase from *Pseudomonas aeruginosa* (A); the conformational change in the E heme domain (B); the oxidized state of P heme domain (C); the mixed-valence state of P heme domain (D). The spheres represent Ca^{2+}. The protein structure colored by green and heme highlighted by red represents the oxidized state (PDB: 1eb7) [27]; the protein structure colored by canyon and heme highlighted by hot pink represents the mixed-valance state (PDB: 2vhd) [27].

1.3.3 DyP-type peroxidase family:

Dye-decolorizing peroxidase (DyP) was discovered in the basidiomycete *Thanatephorus cucumeris,* and it has been shown that this enzyme has the ability to decolorize 18 types of reactive, acidic and dispersive dyes, most of which are xenobiotics [34]. It is a member of a newly discovered and intriguing family of heme peroxidases, the DyP-type peroxidase family. So far, these enzymes have been found only in bacteria and fungi [35]. In this family, four distinct subfamilies (from A to D) can be identified, and it has been surmised that through evolution, subfamilies A and B first diverged from C and D; subsequently, produced the four noted subfamilies [21]. DyP is a member of subfamily D, whereas TyrA, which we will introduce later, belongs to subfamily B.

1.3.3.1 Structures of DyP-type peroxidases:

Consistent with its identity as a peroxidase, DyP contains a heme cofactor and requires H_2O_2 for all reactions. However, DyP has several characteristics that distinguish it from other typical peroxidases. The level of sequence homology with other peroxidases is very low. It is capable of using a wide range of substrates and is tuned to operate at a surprisingly low pH (optimum 3 - 3.2) [36, 37]. Initially, DyP was considered to be a class II member of the peroxidase-catalase superfamily, however, it became increasingly apparent that the primary structure was distinct. Indeed, DyP even lackes the active site signature motif R-X-X-F/W-H that is a hallmark of the peroxidase-catalase superfamily [38]. However, discussion of their structure and function points toward a strategy that might be employed for engineering the C-terminal domain of KatG into a new low pH peroxidase.

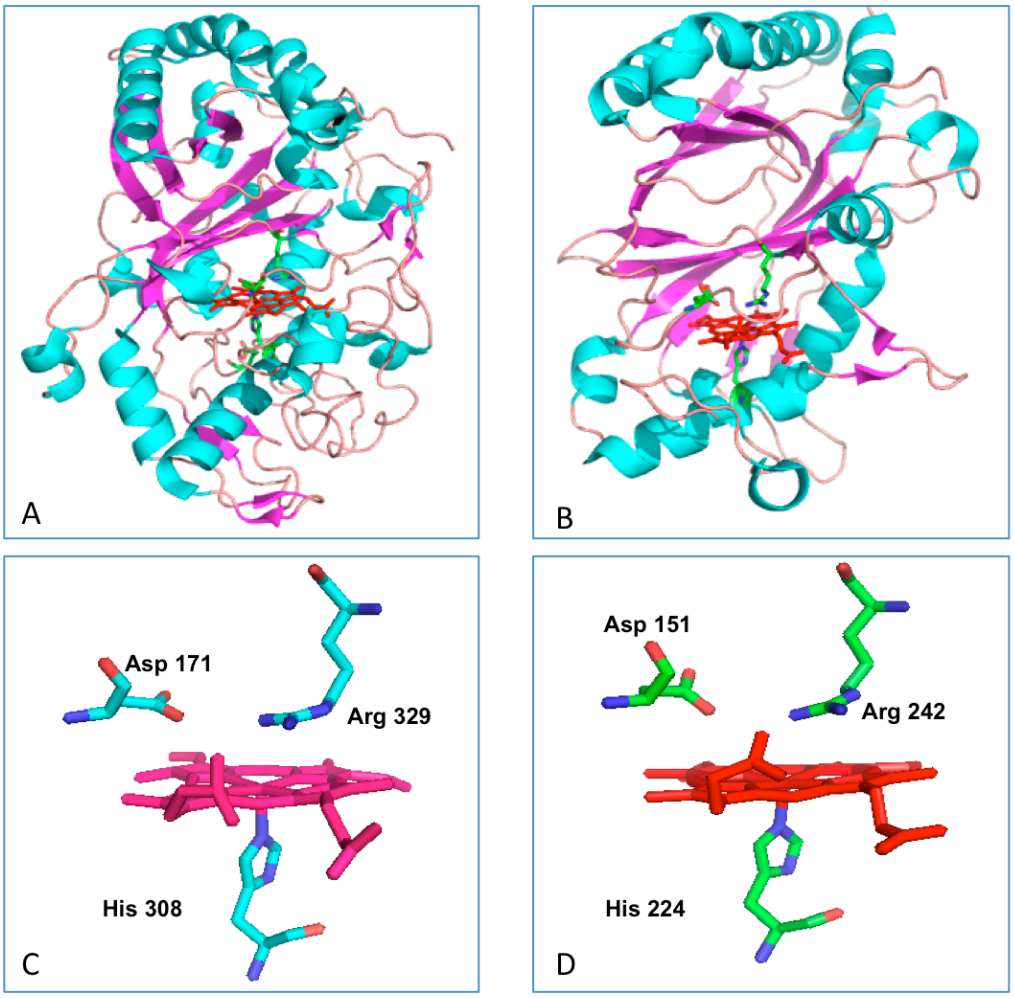

Figure 1.6: Structures of DyP and DyP-type Peroxidase.

A: Overall structure of DyP from *Thanatephorus cucumeris* Dec 1 (PDB: 2D3Q) [39]; B: Overall structure of TyrA from *Shewanella oneidensis* (PDB: 2IIZ) [40]; C: The heme and its surrounding residues important for the peroxidase activity of DyP; D: The active site surrounding of TyrA.

A striking distinction in active site structure is the absence of the typical distal His, instead, its replacement by an aspartate (Asp 171) [35]. Additionally, DyP contains a unique pair of anti-parallel β-sheets located above the distal side of the heme (Fig. 1.6 A) [35]. Although sequence homology between DyP and other DyP-type peroxidase is very low, their overall tertiary structures are quite similar. TyrA, a member of type B DyP-type peroxidases, is a two-domain α + β protein. Each domain contains a four-stranded, antiparallel β-sheet sandwiched by α-helices in a ferredoxin-like fold (Fig. 1.6 B) [40]. At the active site level, three residues: an Asp, an Arg and the proximal His ligand are strictly conserved in this family (Fig 1.6 C and D). The Arg is proposed to assist with the formation of compound I by stabilizing higher oxidation states of heme's iron center [35]. Asp instead of His as a general acid/base catalyst provides an explanation for the extraordinarily low pH optimum of DyP and DyP-type peroxidases [36, 37].

1.3.3.2 Catalytic cycle of DyP and Dyp-type peroxidases:

A mechanism for the formation of compound I based on the participation of Asp and Arg in the active site has been proposed (Fig. 1.7) [35]. According to this model, a conserved Glu 391 forms an H- bond with proximal ligand His 308, increasing the anionic character of the ligand, serving to stabilize higher heme iron oxidation states. In the resting state of DyP, a sixth ligand to the heme iron is absent, allowing for direct formation of a complex with H_2O_2 upon its entrance to the active site. Asp 171 acts as a general base to abstract a proton from the peroxide and deliver it to the distal peroxide oxygen atom concomitant with heterolytic cleavage of the O–O bond. Subsequently, one electron is removed from iron, and another electron is transferred from porphyrin to the remaining oxygen, generating an intermediate analogous to compound I observed in other peroxidases. Recently, a modified mechanism for formation of compound I has

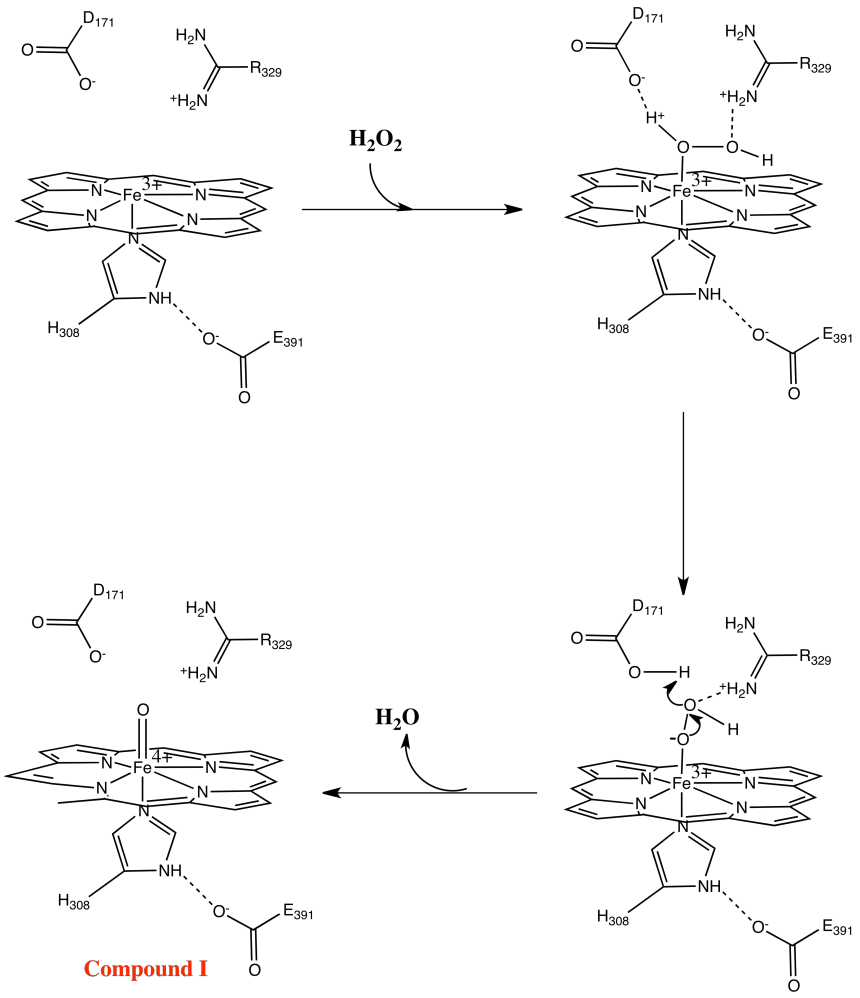

Figure 1.7: Schematic diagram of the proposed formation of compound I by DyP.

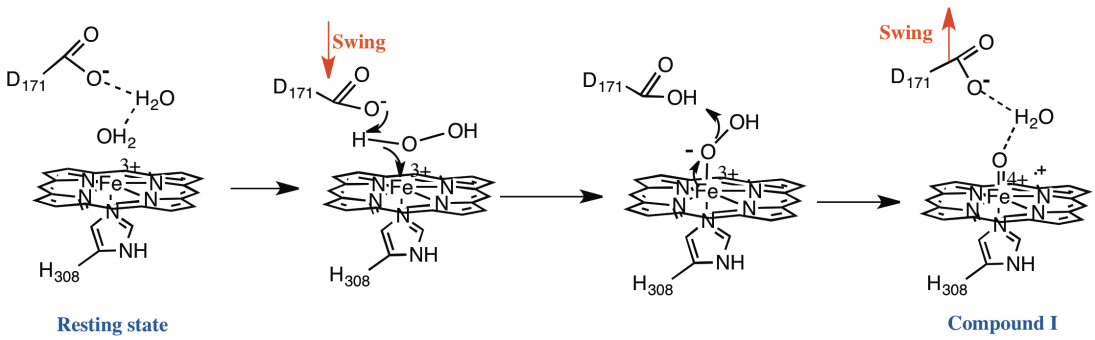

Figure 1.8: A modified mechanism of compound I formation by DyP.

been proposed [39] (Fig. 1.8). In this model, the carboxylate group of Asp 171 associates with the ligand for heme iron by swinging into the appropriate position [39]. Once the compound I is formed, the carboxylate group can revert to its original position in order to stabilize compound I through an H-bonded network involving an active site water molecule. Interestingly, a compound II (ferryl) has never been detected in these enzymes [35]. To date, the picture of the catalytic mechanism of Dyp (or DyP-type) peroxidases remains incomplete.

1.3.4 Haloperoxidases Family:

Haloperoxidase activity has been observed with a variety of heme- or vanadium-dependent enzymes. However, the non-heme (vanadium) haloperoxidases are phylogenetically unrelated to this family. The heme-dependent haloperoxidases are abundant among fungi. They contain protoporphyrin IX as a prosthetic group and catalyze the oxidative transformation of halides and halophenols [41]. A recently constructed phylogenetic tree for this family indicates that heme haloperoxidases form a monophyletic group with frequent gene duplication events [21].

1.3.4.1 Structure and catalytic mechanisms of haloperoxidases family:

In this family, the most intensively investigated member is the chloroperoxidases (CPO) from the ascomycete *Caldariomyces fumago*. This CPO is a 42 kDa glycoprotein. It catalyzes the H_2O_2-dependent chlorination of cyclopentanedione as well as the iodination and bromination of a wide range of substrates [42-46].

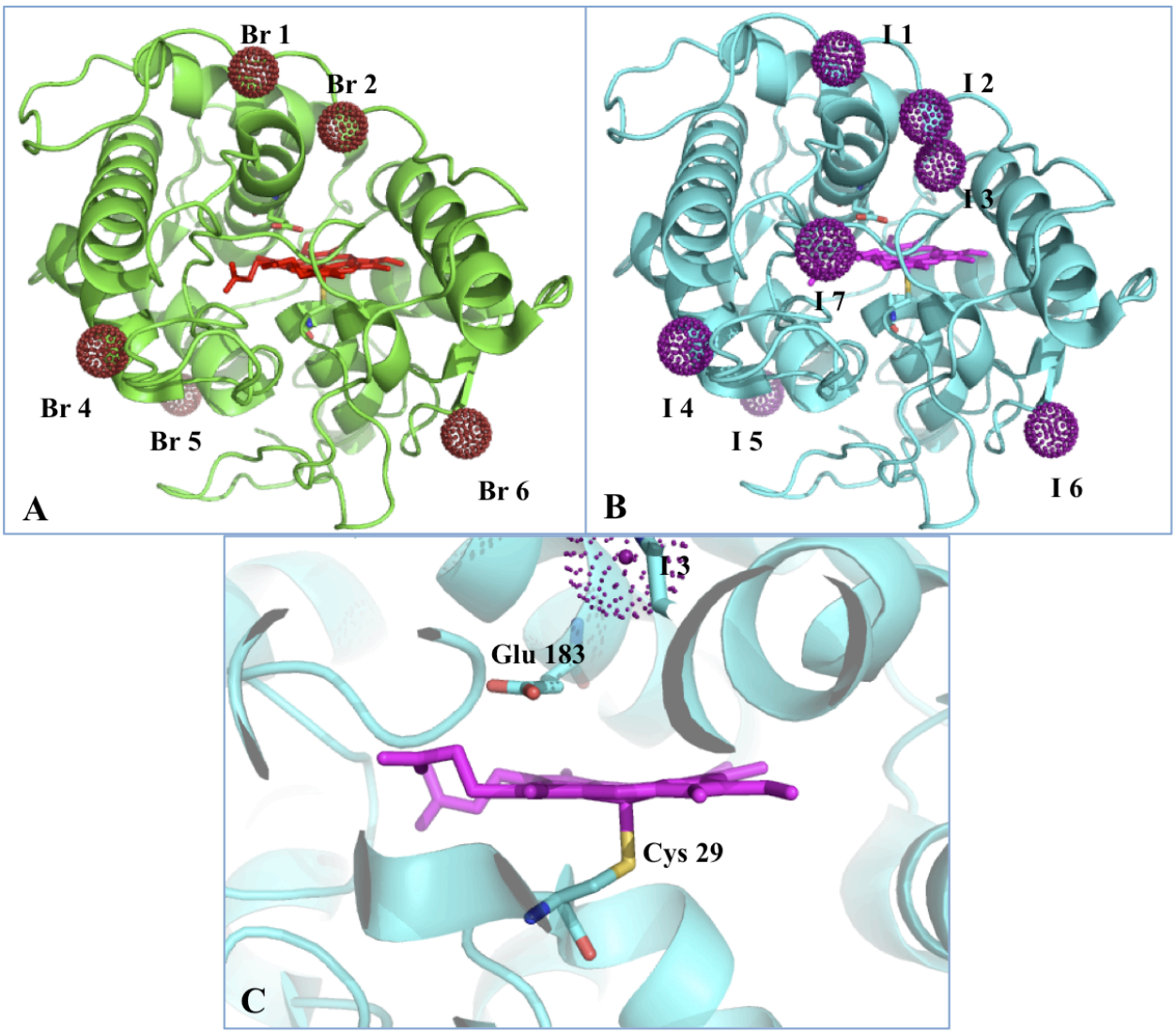

Figure 1.9: Structure of CPO.

Overall structure of CPO with binding of bromide (A) (PDB: 2CIV) and iodide (B) (PDB: 2CIW) [47], and the active site of CPO (C). Dots represent the halides.

Available structures from the protein data bank indicate that CPO has a novel tertiary structure dominated by eight helical segments [48]. In the active site, a cysteine serves as the proximal ligand to the heme iron. Unlike other peroxidases, there is no Arg in the distal cavity, and the catalytic acid/base required to cleave the peroxide O-O bond is Glu rather than His (Fig.1.9). Consequently, CPO is active at low pH with an optimum at 2.8 [42, 47]. This unique active site configuration points to a future strategy by which our stand-alone KatG C-terminal domain ($KatG^C$) may be engineered. Crystal structures solved in the presence of bromide and iodide have been reported. The bromide/iodide binding sites have been identified. The location of these ions points toward a route by which halides may access the heme center [47].

1.3.4.2 Catalytic cycle of CPO:

The fundamental mechanism of CPO-catalyzed halogenations is presented in Fig 1.10 [41]. It begins with the heterolytic cleavage of a loosely bound H_2O_2, resulting in the formation of compound I and H_2O. Compound I is not stable and is proposed to react with the halide to form a hypothetical ferric hypohalite adduct, termed compound X. Decomposition of compound X is proposed to produce a halonium ion (X^+) along with ferric enzyme. In aqueous solution, the hypohalous acid would be expected to form from X^+. Recently, based on substrate-bound structures, a modified mechanism for compound I formation has been proposed [47]. Instead of direct formation of compound I, a ferric-hydroperoxyl species (compound 0) is proposed to be formed first; the Glu 183 then protonates the distal oxygen of compound 0, followed by the formation of compound I along with cleavage of the O-O bond and release of one water molecule (Fig. 1.11).

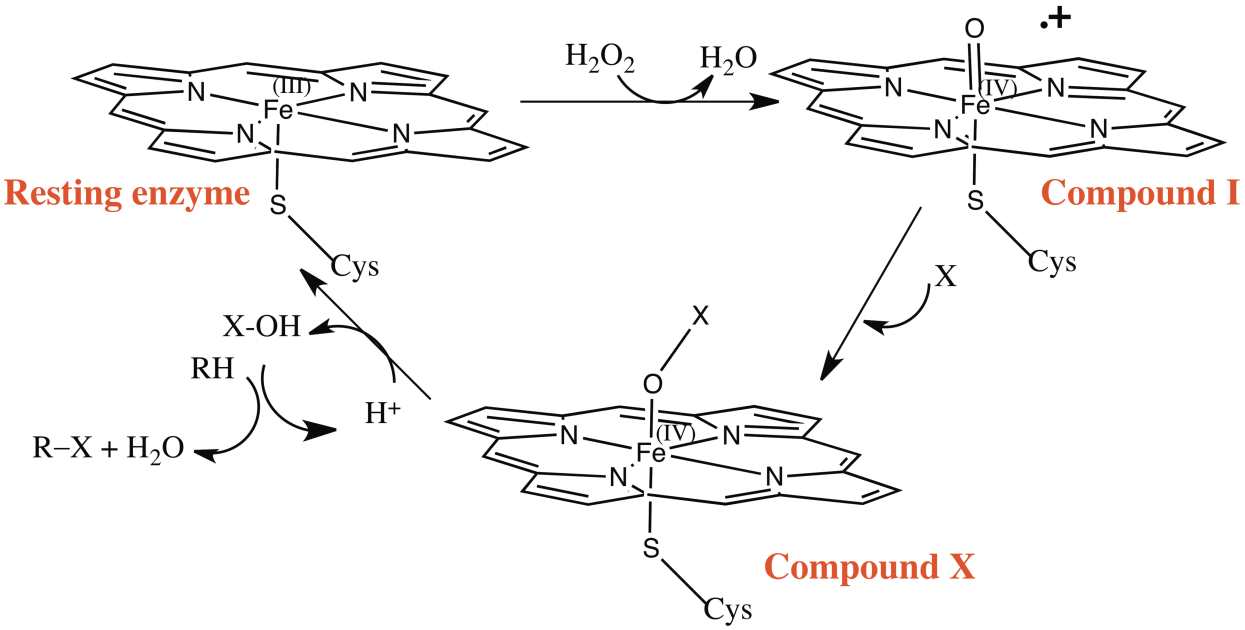

Figure 1.10: Catalytic cycle of haloperoxidases.

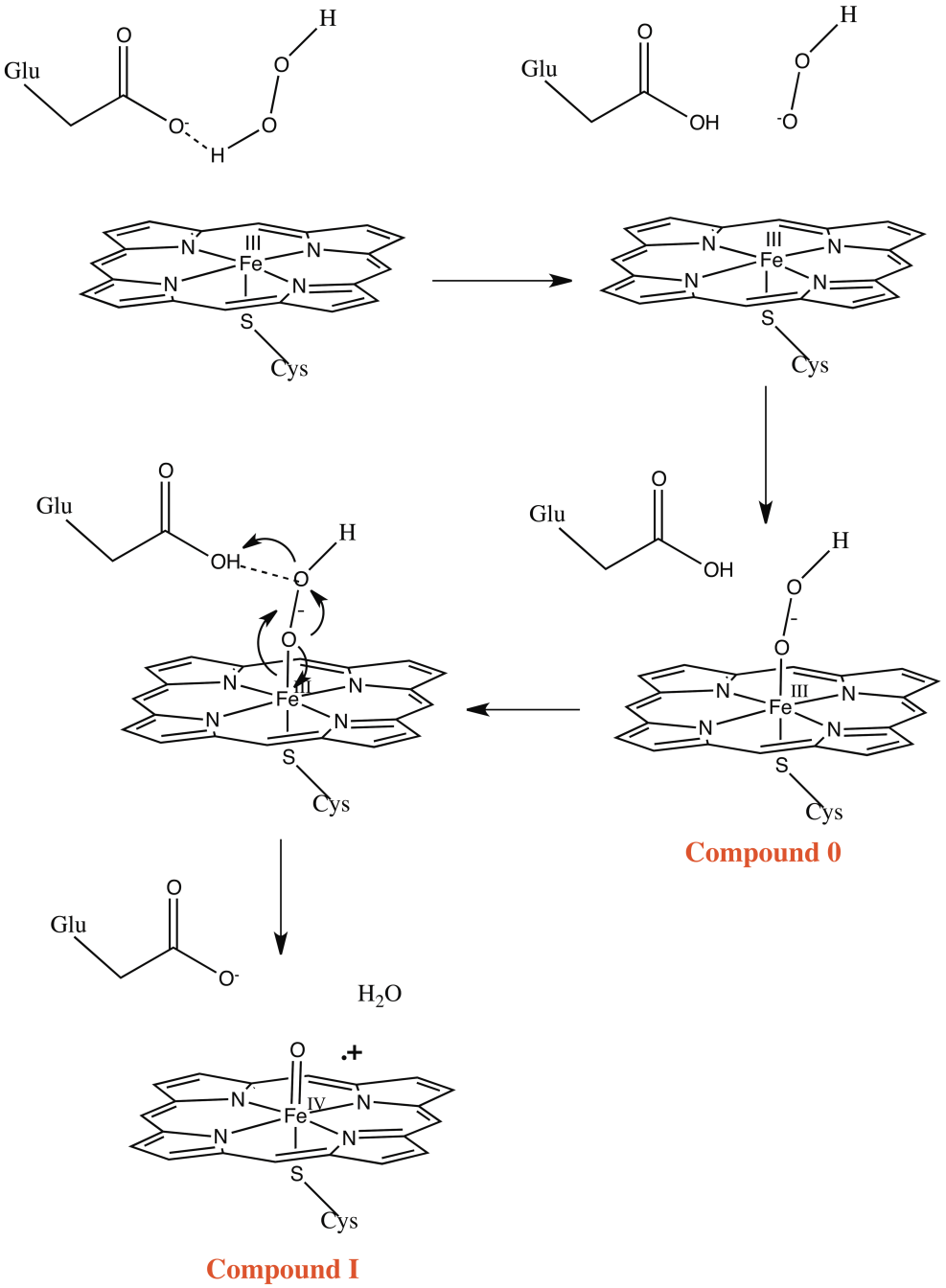

Figure 1.11: Proposed mechanism of compound I formation by chloroperoxidase.

1.3.5 The peroxidase-cyclooxygenase superfamily:

The peroxidase-cyclooxygenase superfamily represents one of the two main groups of heme-dependent peroxidases in biology. Peroxidase-cyclooxygenase and peroxidase-catalase superfamilies arose independently; therefore, the structures of both the protein and prosthetic group are distinct between these two groups [18]. The peroxidase-cyclooxygenase superfamily was originally called the mammalian peroxidases, and was later changed to the animal peroxidase family. However, in recent years, even plant, fungal and bacterial representatives were found and assigned to this superfamily necessitating yet another change in nomenclature. Though this superfamily has been subdivided into seven clades, it is still identified by its most famous members (myeloperoxidase [MPO], eosinophil peroxidase [EPO], lactoperoxidase [LPO] and thyroid peroxidase [TPO]) all of which are found in animals. Because this superfamily is not phylogenetically related to the superfamily containing KatG, this section will only consider the intensively investigated representative, myeloperoxidase (MPO). An interesting feature of many representatives from the peroxidase-cyclooxygenase superfamily is novel covalent linkage between the porphyrin cofactor and protein. In this, MPO is an excellent example.

1.3.5.1 Structure of MPO:

Myeloperoxidase is abundant in neutrophils but also is expressed in monocytes and certain types of macrophages, where it participates in innate immune defense mechanisms by generating reactive oxidants and diffusible radical species [49]. The mature enzyme exists as a homodimer, where each subunit is dominated by α-helices with few β-strands. The subunit is composed of two polypeptide chains resulting from the post-translational excision of a peptide fragment from a single polypeptide precursor [50, 51]. The catalytically essential residues Gln 91, His 95 and

Arg 239 occupy the distal heme pocket; in the proximal site, the heme iron is coordinated through the His 336 imidazole resiude. This ligand forms an H-bond with the amide carbonyl oxygen of Asn 421. One Ca^{2+} ion has been identified and its coordination is essential for maintaining the distal architecture.

A common, but not universal, feature for members of this superfamily is the covalent association of the heme with the protein itself: pyrrole rings A and C of the heme group are methylated, allowing formation of ester linkages with the carboxyl groups of Glu 242 and Asp 94. Additionally, the β-carbon of the vinyl group on pyrrole ring A forms a covalent bond with the sulfur atom of Met 243 (Fig. 1.12). As one might anticipate, this produces unique spectral properties for the heme. In the ferric state, the Soret band shows an absorption maximum around 428 nm and relatively strong absorption bands in the visible region are also detected, which are responsible for the characteristic green color of the enzyme [52]. This unique post-translational modification gives MPO peculiar redox properties, allowing oxidize Cl^- [53].

1.3.5.2 Enzymatic properties and catalytic mechanism:

Under physiological conditions, MPO catalyzes the oxidation of halides (X^-) to the corresponding hypohalite anions (OX^-). To do this the ferric enzyme is oxidized by H_2O_2 to form compound I. Distal His 95 and Arg 239 are proposed to orient and bind the H_2O_2, allowing the heterolytic fission of the O-O bond much as has been observed for other peroxidatic enzymes. In addition to its halogenation activity, MPO is also able to catalyze more typical oxidations of other peroxidatic electron donors. Therefore, once compound I is formed, MPO can catalyze

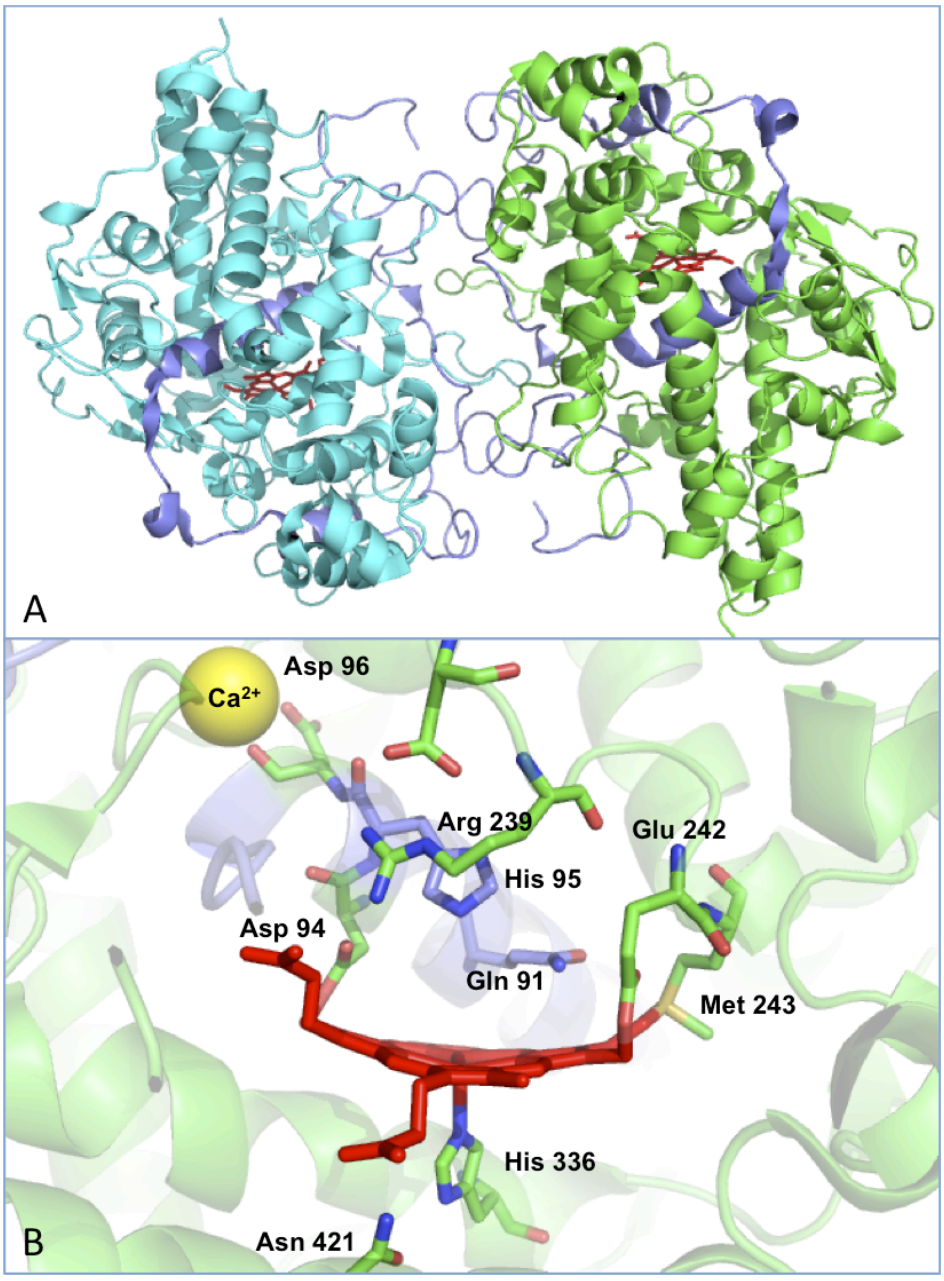

Figure 1.12: Structure of human MPO.

Overall structure (A), and active site (B) of human MPO. Different colors highlight the structures from two different polypeptides (PDB:1CXP) [54].

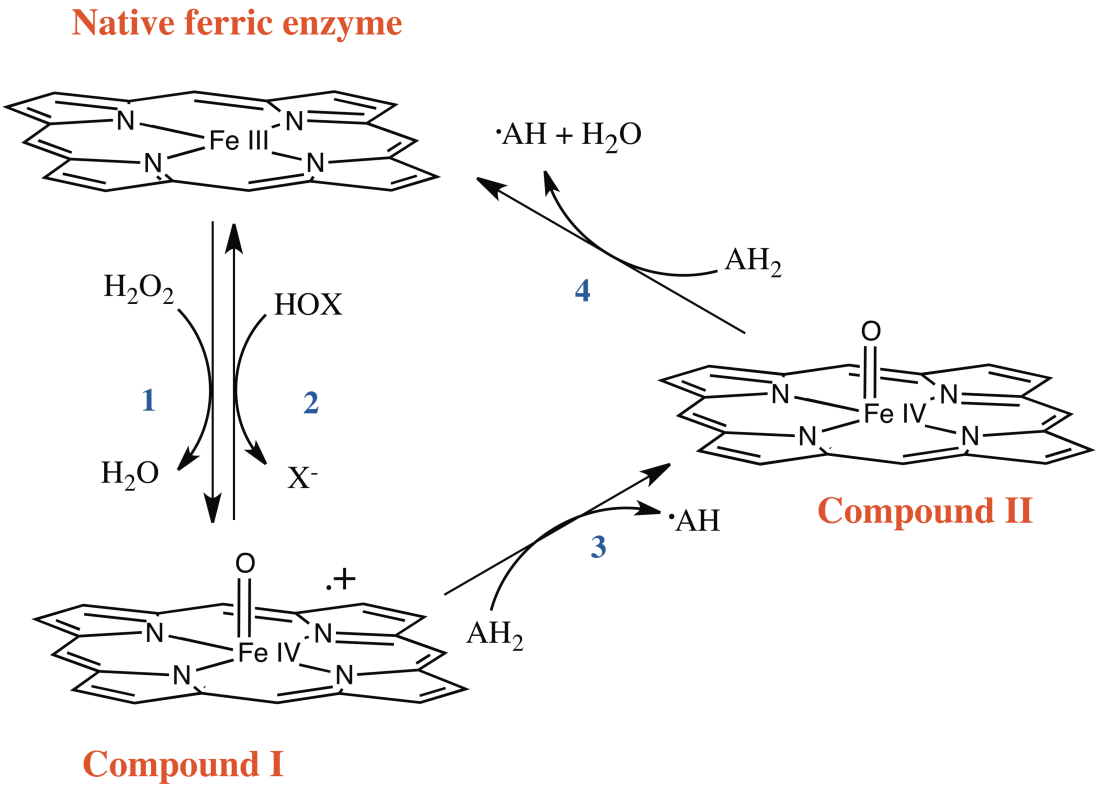

Figure 1.13: Catalytic cycles of MPO.

Halogenation cycles: reaction 1 and 2; Peroxidase cycles: reaction 1, 3 and 4 [49].

either halogenation or canonical peroxidation (Fig. 1.13). In the halogenation cycle, compound I is reduced back to the ferric state by the oxidation of halide (X^-) substrates. In the peroxidase cycle, compound I is reduced back to the native state in two sequential one-electron steps using another exogenous reducing substrate (AH_2). Presumably, the operating cycle is determined by the availability of substrate.

1.3.6 The peroxidase-catalase superfamily:

The first systematic classification of the enzymes of this superfamily was published in 1992 [38] and divided its members into three classes. In contrast to other peroxidase superfamilies, this subdivision has remained unchanged since that time. Class I includes cytochrome *c* peroxidases, ascorbate peroxidases and catalase-peroxidases (KatG). Class II contains fungal peroxidases, predominantly lignin and manganese peroxidases. Class III includes the secretory plant peroxidases. Though the subdivisions have not changed, the name of the overall superfamily was recently changed from the superfamily of plant, fungal, and bacterial heme peroxidases to peroxidase-catalase superfamily in order to reflect the main enzymatic activities of its members [21].

The Class I members are widely distributed in nature with the exception of animals. Though the physiological roles of the peroxidase-catalases vary considerably, the class I enzymes serve exclusively as H_2O_2 scavengers [55-57]. The class II peroxidases are found exclusively in fungi and have a major role in degradation of lignin [58, 59]. Class III are mostly plant-secreted glycoproteins with roles in a variety of physiological processes of the plant life

cycle such as cell wall metabolism [60], wound healing [61, 62], auxin catabolism [63], H_2O_2 scavenging, and defense against pathogens [64].

1.3.6.1 Class III: Plant secretory peroxidases:

The most intensively investigated representative of this family is horseradish peroxidase (HRP) from *Armoracia rusticana*. In this section, the discussion of structure and catalytic mechanism of class III peroxidases will focus on HRP.

1.3.6.1.1 Structure of HRP:

Crystal structures reveal that HRP has ten helices assigned A-J which produce a fold that is highly conserved in the Class III family, and several unique features: a long insertion between helices F and G; a short antiparallel β–sheet preceding the C177-C209 disulfide bridge; and a three-residue insertion between the H and I helix [65]. In HRP, all the N-glycosylation sites positioned in loop regions are pointing away from the molecule except Asn 268 which is located right at the end of the I helix, indicating the purpose of glycosylation is to increase solubility of the enzyme [65]. Recent reports indicate that glycan may stabilize the protein and adjust the substrate access [66-68]. In addition, there are four disulfide bonds between cysteine residues 11-19, 44-49, 97-301 and 177-209. Of those, the disulfide bond in the distal heme-binding domain is proposed to dedicate to stabilizing active site structure [64].

In the active site, the ferric heme *b* prosthetic group is ligated to the protein though His 170, which also hydrogen bonds to the Asp 247 carboxylate group. Three strictly conserved residues are located at the distal site: His 42 serves as a general base/acid; Arg 38 is essential for

the formation and stabilization of compound I; Phe 41 prevents substrate access to the ferryl oxygen of compound I [69]. In addition, Asn 70 is strongly conserved in the peroxidase-catalase superfamily and has been proposed to maintain the basicity of the distal His (His 42) [70]. In both the distal and proximal sites, two hepta-coordinate Ca^{2+} ions are required for both structural stability and catalytic functions [69, 71, 72] (Fig. 1.14). Loss of Ca^{2+} or disruption of its interactions results in the B-helix bearing distal His shift, allowing the distal His to directly coordinate with the heme iron. Therefore, the Ca^{2+}-deficient HRP is inactive, but this is reversible and can be remedied by addition of Ca^{2+} [69, 71, 72].

1.3.6.1.2 Catalytic mechanism of HRP:

The mechanism of catalysis of HRP has been extensively investigated [73, 74]. Similar to those of other peroxidases we described previously, the first step in the catalytic cycle is generation of compound I. Once compound I is formed, typically aromatic electron donors reduce compound I to compound II, then compound II is reduced back to the resting state of the enzyme by another equivalence of reducing substrate. Although the formation of these intermediates has been proposed for a number of catalytic heme enzymes, these species are formed only transiently and have been somewhat elusive to identify until recent years. The structures of the HRP catalytic cycle intermediates have been obtained at high resolution by X-ray crystallography, allowing direct and accurate comparison of the bonding interactions in the different intermediates [75]. The catalytic cycle of HRP with the structures of the intermediates is summarized in Fig. 1.15.

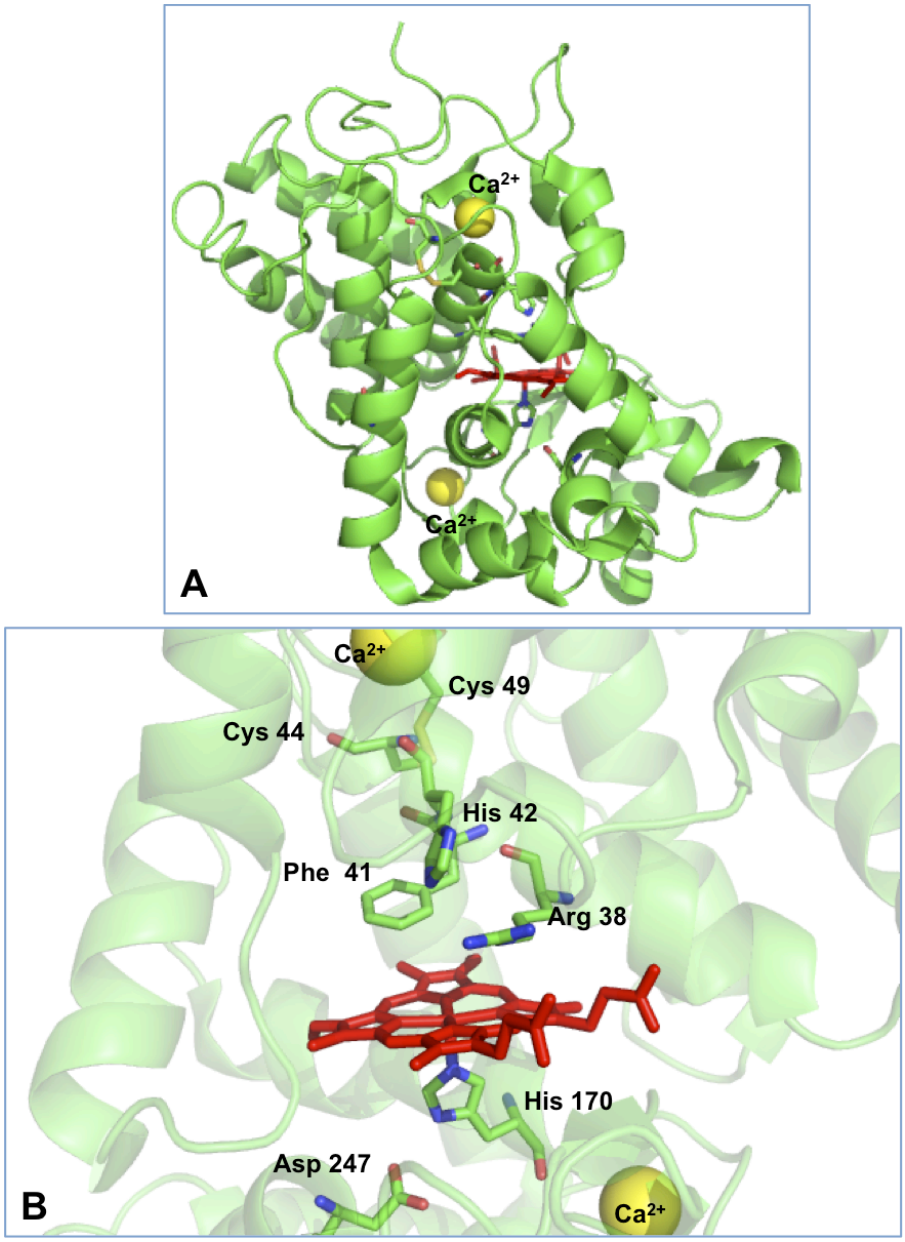

Figure 1.14: Structure of HRP.

Overall structure of horseradish peroxidase (HRP) (PDB: 1h5a) (A) and the active site of HRP (B) [75].

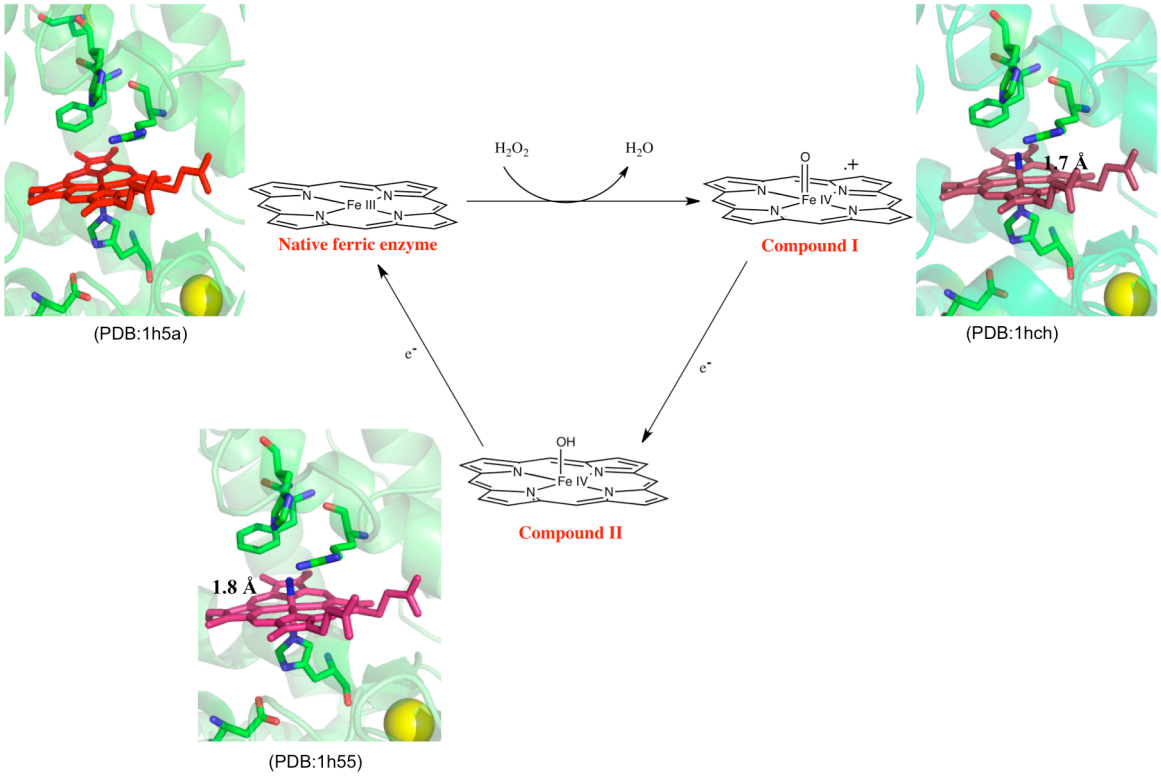

Figure 1.15: Peroxidase cycle of HRP.

1.3.6.2 Class II: Manganese, lignin and versatile peroxidases:

Extracellular Class II heme peroxidases are currently known only in fungi and have their principle function in lignin degradation [76]. There are three main groups secreted by *Basidiomycetes* or so-called white rot fungi: manganese peroxidases (MnP), lignin peroxidases (LiP), and versatile peroxidases (VP).

1.3.6.2.1 Structure and function of Class II peroxidases:

The degradation of lignin to CO_2 by this small and specialized group of fungi is a major route for the recycling of photosynthetically fixed carbon [77]. Lignin is chemically recalcitrant to catabolism by most organisms because of its complex, heterogeneous and irregular structure. In nature, only the *Basidiomycota* are able to degrade lignin efficiently. They produce four major groups of enzymes for lignin degradation: LiP, MnP, VP that belong to Class II peroxidase family and a laccase, which is a multi-copper-containing protein.

Along with the two other peroxidases, LiP catalyzes the H_2O_2-dependent oxidative degradation of lignin, but the mechanism by which this occurs is poorly defined [78, 79]. In addition, LiP displays classical peroxidatic catalytic promiscuity with respect to the electron donor substrate. The enzyme has been shown to oxidize phenolic compounds (especially veratryl alcohol) as well as a broad range of nonphenolic aromatic compounds. Interestingly the reach of LiP in terms of the redox potential of compounds it will oxidize extends as high as 1.4 V [80]. The pH optimum (~3) for the enzyme is strikingly low considering the structure of its active site. Crystal structures for LiP reveal eight major and eight minor α-helices with a few β structures in the proximal domain [81]. The overall folding and active site environment of LiP

are highly similar to those of HRP (Fig. 1.16A). In addition, LiP contains three glycosylation sites, which have been indicated to protect the C-terminal peptide from proteolysis [77]. Similar to HRP, LiP has four disulfide bridges and two structural calcium ions which are essential for maintaining the structure of the active site [81]. The location of the two Ca^{2+} coordination sites are similar to those observed in HRP; however, the disulfide bond that enhances the stability of the distal Ca^{2+} binding site in HRP is absent in LiP, making the coordination state and enzyme activity much more sensitive to the loss of the Ca^{2+} ion in LiP.

Interestingly, a novel post-translational hydroxylation of Trp 171 (Cβ) has been identified [81]. This is proposed to have an important role in the binding and oxidation of aromatic substrates through long-range electron transfer [82-84]. This Trp residue and the electron-deficient heme are purported to account for the high reduction potentials of the enzyme's ferryl intermediates [85]. These endow LiP with the unique ability to catalyze oxidative cleavage of C-C bond and ether bonds in non-phenolic aromatic substrates.

Manganese peroxidase is an acidic glycoprotein. The overall structure of MnP is similar to that of LiP [86]. Two heptacoordinated structural calciums with similar positions and functions as those observed in LiP [87] (Fig. 1.16B). The active sites of MnP and LiP are virtually identical to one another. MnP does possess an additional disulfide bond in addition to those four that are also seen in LiP. This unique fifth disulfide is proposed to assist in Mn^{2+} binding by pushing a C-terminal peptide segment away from the main body of the protein [77]. A bound Mn(II) ion has been identified at the surface of the protein coordinated to the carboxylates of Glu 35, Glu 39 and Asp 179, one of the heme propionates and two water molecules. As described in

greater detail below, MnP utilizes Mn^{2+} as a direct substrate, the oxidation product of which mediates the oxidation of secondary substutrates.

Structurally, versatile peroxidases (VP) resemble LiP more closely than MnP. The available structure shows a 12 helices, 4 disulfide bonds, a heme pocket containing the characteristic proximal and distal triads, 2 structural Ca^{2+} sites, and a Mn (II) binding site (Fig. 1.16C) [88]. The solvent accessible Trp 64 is essential in the oxidation of high redox potential aromatic substrates via a long-range electron transfer pathway similar to that observed for LiP [89].

1.3.6.2.2 Catalytic cycles of Class II peroxidases:

LiP has a typical peroxidase catalytic cycle similar to that of horseradish peroxidase (Fig. 1.15). The primary different is in the involvement of long-range electron transfers for LiP. In a sense, MnP utilizes a similar long-range electron transfer strategy as that observed for LiP; however, instead of oxidizing a surface tryptophanyl residue, MnP catalyzes the oxidation of Mn(II) to Mn(III) which in turn may be used to oxidize numerous monomeric phenols including dyes as well as phenolic lignin model compounds [90]. The overall characteristics of the cycles of LiP, VP, and MnP are highly similar to those of HRP (Fig. 1.17). Another difference between LiP and MnP is oxidation of non-phenolic substrates by MnP involves the formation of reactive radicals in the presence of second mediators (e.g., thiols) [91]. The mechanism employed by VP is essentially the same as that of LiP except that VP can also utilize Mn(II) as a mediatory substrate much as MnP does.

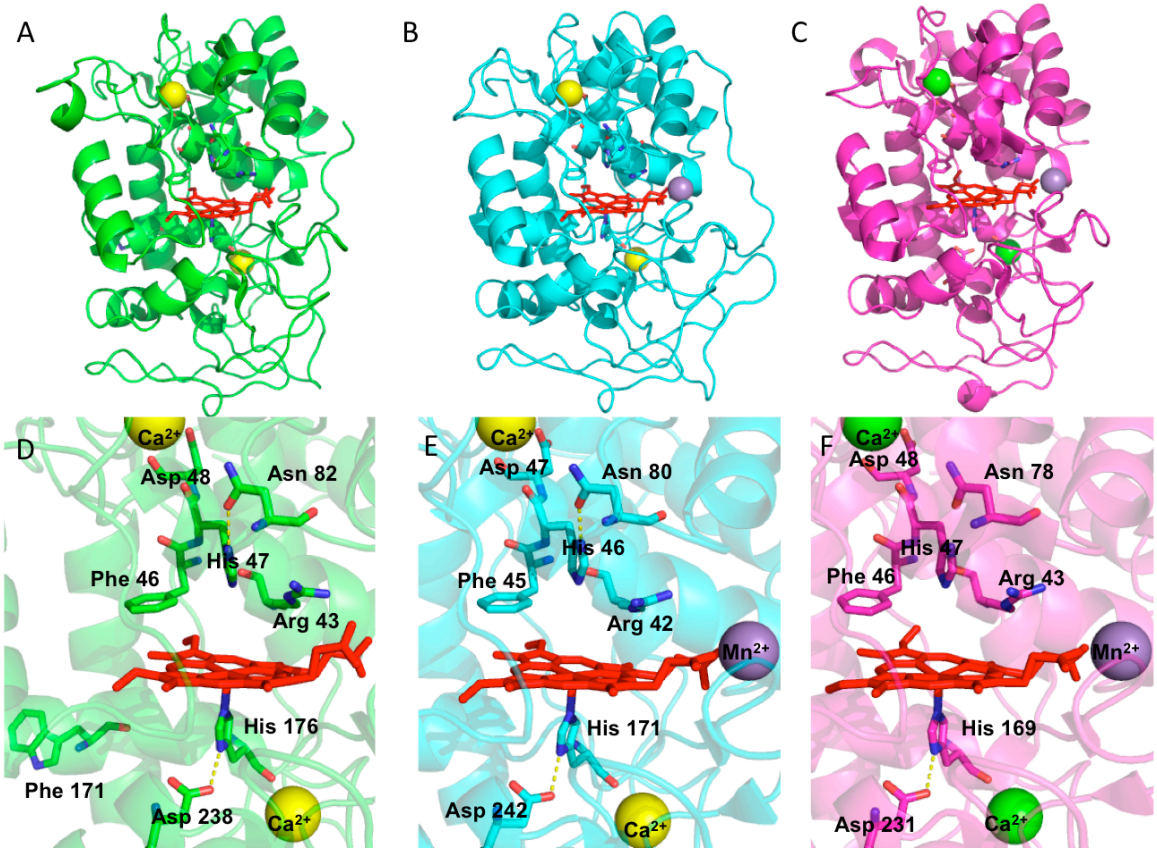

Figure 1.16: Structure of Class II peroxidases.

Overall structures of LiP (PDB: 1LGA)(A) [81], MnP (PDB: 1MNP) (B) [86] and VP (PDB: 2BOQ) (C) [88], and the active sites of LiP (D), MnP (E) and VP (F).

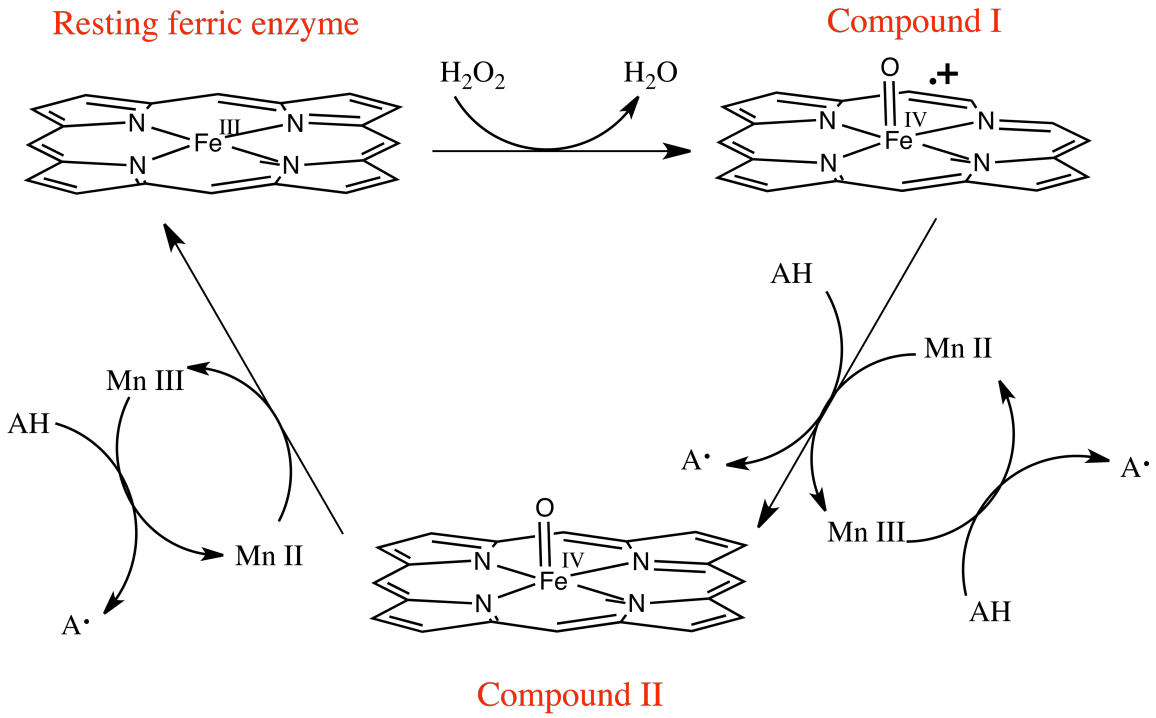

Figure 1.17: Catalytic cycle of manganese peroxidase (MnP).

1.3.6.3 Class I peroxidases:

1.3.6.3.1 Introduction of Class I peroxidases:

Class I peroxidases include intracellular prokaryotic and eukaryotic non-glycosylated heme peroxidases without Ca^{2+} [38, 92]. Extensive gene sequence analysis of all three classes indicate that the whole peroxidase-catalase superfamily originated from ancestral Negibacteria, and during evolution the already diversified peroxidase genes were transferred via two ancestral endosymbiotic events to newly formed eukaryotic cells [19, 93]. Class I segregated at an early stage from a common ancestor of the class II and class III peroxidases [94]. However, the evolutionary lineage of CCP and APX from the two-domain KatG remains contested [38, 92].

Ascorbate peroxidases are predominantly observed among green algae and higher plants. Their primary physiological role is to scavenge H_2O_2 as part of the ascorbate-glutathione cycle [55, 95]. Ascorbate peroxidase plays an important role in root nodules of leguminous plants and chloroplasts in general. Given that O_2 is a known inhibitor of photosynthesis and can deactivate nitrogenase, a peroxide degradation mechanism that avoids generating O_2 is particularly advantageous.

The subfamily of CCPs can be divided into two groups: mitochondrial and non-mitochondrial. The enzyme from *Saccharomyces cerevisiae* is located in the intermembrane space of mitochondria where it decomposes H_2O_2 generated by the mitochondrial respiratory chain [96]. In addition to acting as a H_2O_2 scavenger, CCP appears to be integral to the oxidative stress response to methanol utilization in the methylothropic yeast [97]. The enzyme from

pathogenic basidiomycetes has been implicated in the bacterium's resistance against exogenous oxidative stress [98].

1.3.6.3.2 Structure and Catalytic function of APX and CCP:

As with all members of the peroxidase-catalase superfamily, the structures of all class I enzymes are dominated by the α–helix. As a percentage, KatGs exhibit the lowest contribution from α–helix, whereas the APXs have the highest with CCPs falling in between. All class I enzymes carry heme *b* as a cofactor, and in each case, it is non-covalently held by the protein that carries it. The distal Arg-Trp-His and proximal His-Asp-Trp triads of the active sites are strictly conserved among class I enzymes not only in sequence, but also in their position/orientations within the active site (Fig. 1.18) [2]. There is some evidence that the distal Arg may occupy two positions: one "out" and one "in" [99], where only Arg occupying the "in" position can form H-bond with the iron-linked ferryl oxygen atom. As elsewhere this interaction is proposed to stabilize the ferryl center of compound I [99]. Crystal structures as well as spectroscopic properties of the enzymes indicate several differences between CCP and other peroxidases. The typical compound I (ferryl porphyrin radical) does not accumulate in CCP due to facile electron transfer from an active site, forming instead a ferryl tryptophanyl radical intermediate referred to by some as "compound ES" [100]. In addition, two fully conserved methionines (230 and 231) serve to stabilize the Trp radical [101]. In contrast, a typical compound I (ferryl porphyrin radical) intermediate is observed upon reaction of APX with H_2O_2. In this protein, a potassium ion bound adjacent to the proximal Trp not only stabilizes the conformation of the APX active site [102], but also disfavors Trp oxidation to its corresponding radical intermediate. Beyond this, the catalytic cycles APX and CCP are highly similar to those

observed for class II and III peroxidases (Fig. 1.15 and 1.17). One notable feature in both cases is the identity of the preferred electron donor substrate. Reduced cytochrome *c* and ascorbate are both strikingly poor electron donors for all other peroxidases. In these instances, CCP and APX have clearly adapted to employ the electron donor that is available in the cellular environment of each one.

1.4 Catalase-peroxidases (KatGs):

Phylogenetic analyses suggest the duplication event evident in the KatG gene may have occurred in the later phases of evolution, where the individual and distinguishing features of the peroxidase families were already formed [102]. The KatGs are broadly distributed among archaea, bacteria and lower eukaryotes. It appears that their primary purpose across these organisms is to degrade H_2O_2. Despite all their similarities to other peroxidase-catalase superfamily members (especially class I enzymes), KatGs are unique in that they use single active site to catalyze two fundamentally different reactions.

1.4.1 The biomedical benefits of understanding KatG structure and function:

The vast majority of superfamily members are monomeric, and with the lone exception of KatG, the subunits of these enzymes are composed of a single domain. As a consequence, the novel two-domain composition of KatGs provide a rare opportunity to evaluate mechanisms in which structures peripheral to and distant from an active site influence its architecture and catalytic ability. This aspect of the structure/function relationship is rarely studied and poorly understood.

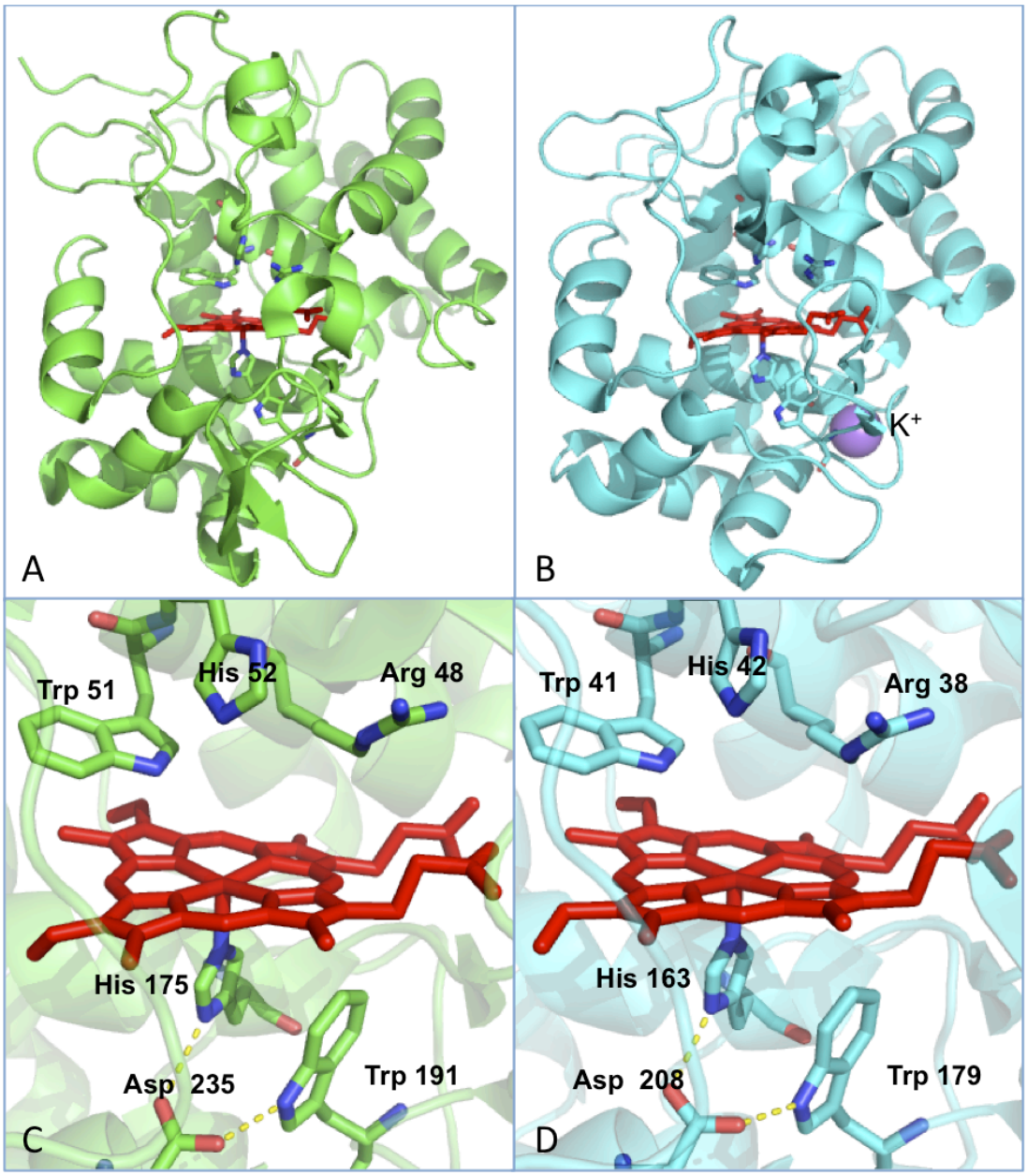

Figure 1.18: Structure of Class I peroxidase.

Overall structure of CCP (PDB: 2CYP)(A), APX (PDB: 1OAF) (B) and the active site of CCP (C), APX (D) [103, 104].

There are substantial biomedical benefits to be derived from an understanding of KatG structure and function. First, KatG from *Mycobacterium tuberculosis* has a central role in the activation of isoniazid (INH), a front-line antitubercular agent. In *M. tuberculosis,* INH is activated by KatG, leading to the formation of an INH-NAD adduct [105-108]. This adduct inhibits InhA, the enoyl-ACP reductase of the fatty acid synthase type II system, which is the central enzyme complex in mycolic acid biosynthesis [109, 110]. Consequently, inhibition of mycolic acid production interferes with mycobacterial cell wall construction and ultimately results in cell death [109, 110]. It has been estimated that 70% of isoniazid resistant strains carry mutations to the gene for KatG. The mechanisms by which many of the commonly observed mutations compromise isoniazid activation are not known. Clearly, a better understanding of KatG structure and function will be beneficial for resolving these questions.

In addition, KatGs have been implicated as virulence factors in organisms like *Yersinia pestis* [111-113]*, Legionella pneumophila* [114], and enterohemorrhagic *E. coli* [115, 116]. These organisms produce a periplasmic or extracellular form of KatG. Because a central strategy of antibacterial responses of plants, mammals and other higher eukaryotes relies on the production of copious quantities of reactive oxygen species, particularly H_2O_2, the advantage to be gained from a robust extracellular catalase is considerable. The oxidative burst of neutrophils and macrophages rapidly produces high levels of O_2•− which disproportionate to H_2O_2. In neutrophils, H_2O_2 is used by myeloperoxidase to oxidize chloride to hypochlorous acid. In macrophages, the rapid generation of •NO along with O_2•− produces peroxynitrite anion. The ability to rapidly degrade H_2O_2 and other peroxides like peroxynitrite is essential for pathogenic bacteria employ as a defense against the host's immune response. Therefore, the periplasmic

location of these enzymes is an essential strategy that allows access to the target substrate before it has had an opportunity to damage essential cellular systems. The connection between KatG structure and its utility in this role remains to be explored, and a greater knowledge of KatG structure will be necessary in order to exploit this enzyme as a target to hobble bacterial antioxidant defenses, making pathogens like *E. coli* O157:H7 or *Yersinia pestis* more vulnerable to the hosts' own natural antibacterial defenses.

1.4.2 Structure of KatGs:

The catalase-peroxidases exist as either homodimers or homotetramers [117]. Each subunit is composed of two structurally homologous domains [118]. Neither domain bears any resemblance to monofunctional catalases; rather, both domains strongly resemble monofunctional peroxidases, bearing the same topological structure and similar helical structure around the active sites [119-122]. Structural data and amino acid sequence alignments indicate that there are 10 major helices in each domain, similar to other class I members. Interestingly, the heme-binding consensus sequence is only observed in the N-terminal domain, and hence, this domain contains the only functional active site. In contrast, the C-terminal domain lacks the heme-binding motif, and as a result, does not bind heme or catalyze a reaction.

At the active site level, the available crystal structures reveal that the KatGs have the proximal and distal conserved amino acids at almost identical positions as in other class I peroxidases. In particular, both the triads His/Trp/Asp and His/Arg/Trp are strongly conserved and almost in superimposable positions found in other class I peroxidases (Fig. 1.19) [119-122]. In addition, a conserved Asp 135 participates in the extensive KatG-typical hydrogen-bond

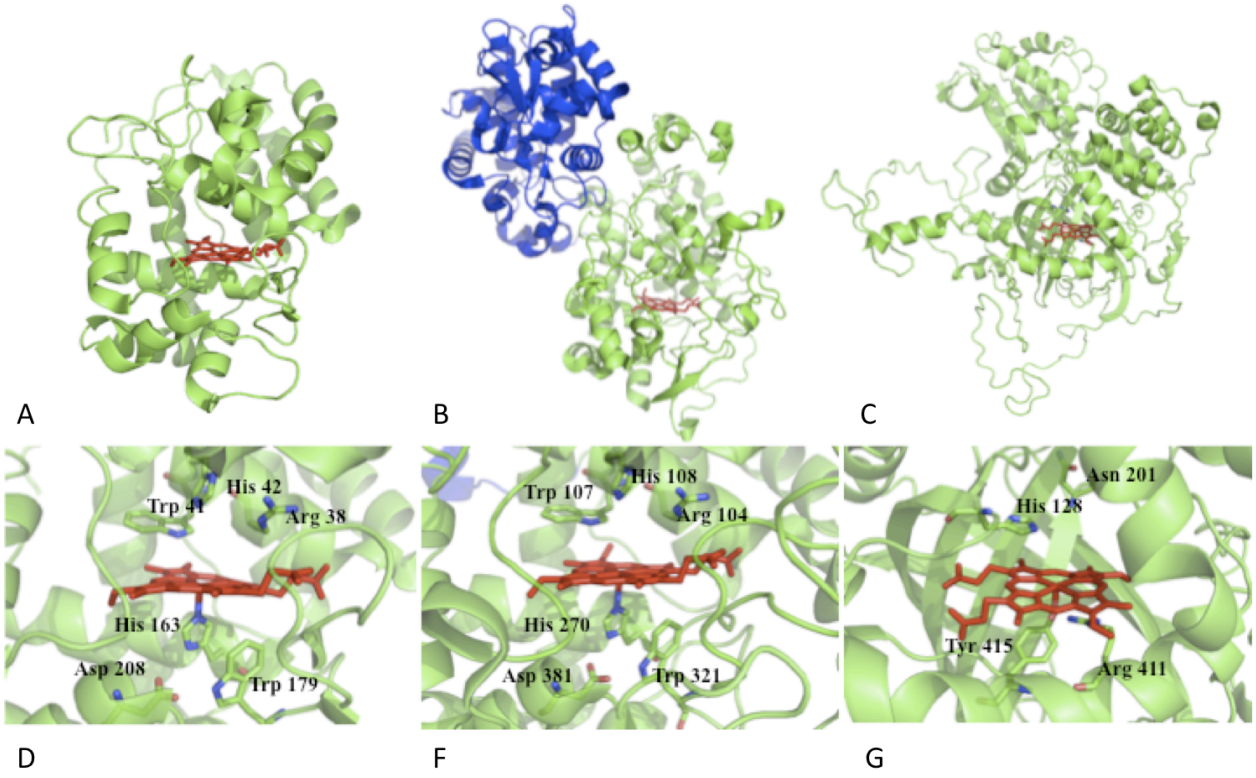

Figure 1.19: Comparisons of the overall structures and the active sites of monofunctional peroxidases, KatG and monofunctional catalases.

APX, (PDB: 1OAF) (A and D, respectively), catalase-peroxidase (PDB: 1SJ2) (B and F, respectively) and HPII from *E.coli*, (PDB: 1IPH) (C and G, respectively).

network at the distal heme pocket. Asn 136 is conserved in all members of the peroxidase-catalase superfamily and supports this network through a hydrogen bond to the distal His. On the basis of site-directed mutagenesis and spectroscopic studies, it has been suggested that the catalase-unique reaction requires this precisely aligned H-bond network [123-125]. Another obvious difference between KatG and monofunctional peroxidase is that there is a pronounced funnel channel to the active site in KatG that is reminiscent of monofunctional catalases. In KatG, the acidic residues are critical for stabilizing the solute matrix and orienting the water dipoles in the channel. Accordingly, exchange of the acidic residues affects catalase but not peroxidase activity [126].

Most KatGs do not contain any disulfide bonds. Extracellular KatGs secreted by certain fungi stand as an exception. Indeed, the recently solved structure for a eukaryotic KatG from *Magnaporthe grisea* shows two disulfide bridges between the N-terminal domains of two subunits [127]. These cysteines, and presumably the disulfide bonds which result, appear to be fully conserved but only in the group of the secreted fungal KatGs (Fig. 1.20). They are also absent in the other members of class I peroxidases such as CCP and APX. These disulfide bonds significantly increase the structural integrity of the enzyme, making the N-terminal domain more stable than the C-terminal domain [127].

Although KatG belongs to the class I peroxidase family, none of the other class I members (e.g., CCP and APX) has appreciable catalase activity. Given the high similarity of the monofunctional peroxidase and KatG active sites, it is reasonable to suggest that KatG-unique protein structures external to the active site have an important role in fine-tuning the active site

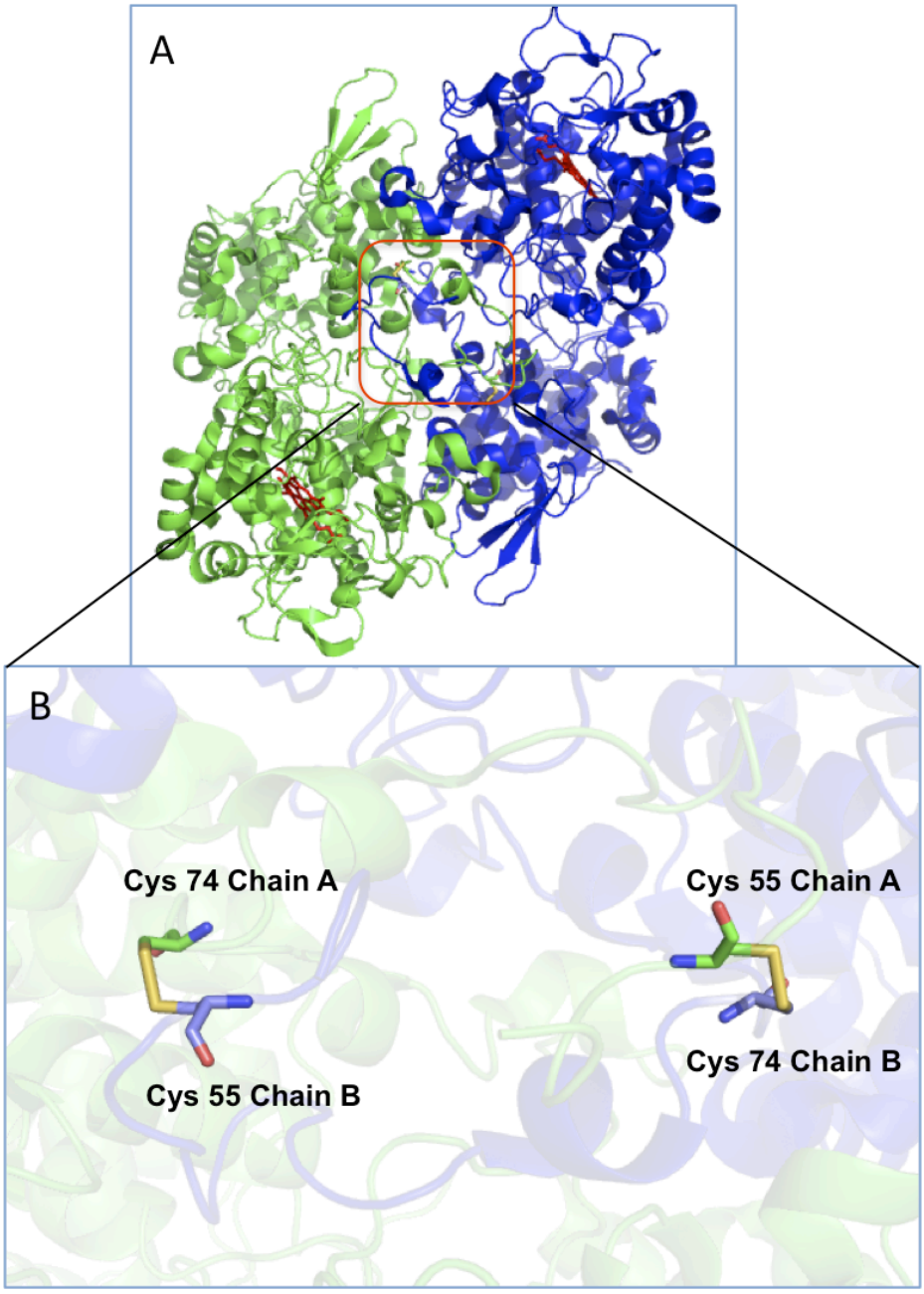

Figure 1.20: Two novel disulfide bridges between the N-terminal domains of two subunits in KatG.

KatG from *M. Grisea* KatG 2 (PDB: 3UT2) shown in the overall structure (A) and zoom-in view (B) [127].

for its bifunctional abilities. In support of this hypothesis, sequence alignments [118, 128] and the four available crystal structures of the KatGs [119-122] reveal several structural features that are unique to these enzymes. Two of them are Large Loops 1 and 2, LL1 and LL2, respectively (Fig. 1.21). Relative to the other class I enzymes, each one adds about 35 amino acids to the interhelical loops connecting the D and E helices and F and G helices, respectively. Evaluation of a wide array of substitution and deletion variants targeting the LL2 structure suggests that this loop structure may support hydrogen-bonded networks critical for reactions involving H_2O_2 and may regulate access of electron donors to the active site [129, 130].

A striking feature of LL1 is that it contains the invariant Tyr (Y226 by *E. coli* KatG numbering), which participates in a novel Met-Tyr-Trp covalent adduct located on the distal side of the heme active site. This adduct has been observed in the crystal structures [119-121, 131] (Fig. 1.22) as well as by mass spectrometric peptide mapping [132-135]. Elimination of LL1 or substitution of Y226 eliminates catalase activity, but deletion variants are substantially more active as peroxidases, up to an order of magnitude increase to the rate in same cases [128, 136]. In addition to orienting this invariant tyrosine for participation in the essential covalent adduct, LL1 also appears to regulate the access of reducing substrates to the heme edge [128, 136].

1.4.3 Catalytic cycles of KatGs:

KatGs are capable of H_2O_2 decomposition by catalatic and peroxidatic mechanisms, and they do so using a single active site. In the classical model, both catalase and peroxidase cycle start with heterolytic reduction of H_2O_2 along with oxidation of ferric enzyme to compound I (Fig. 1.23A). Once compound I is formed, it can be reduced to the resting state either

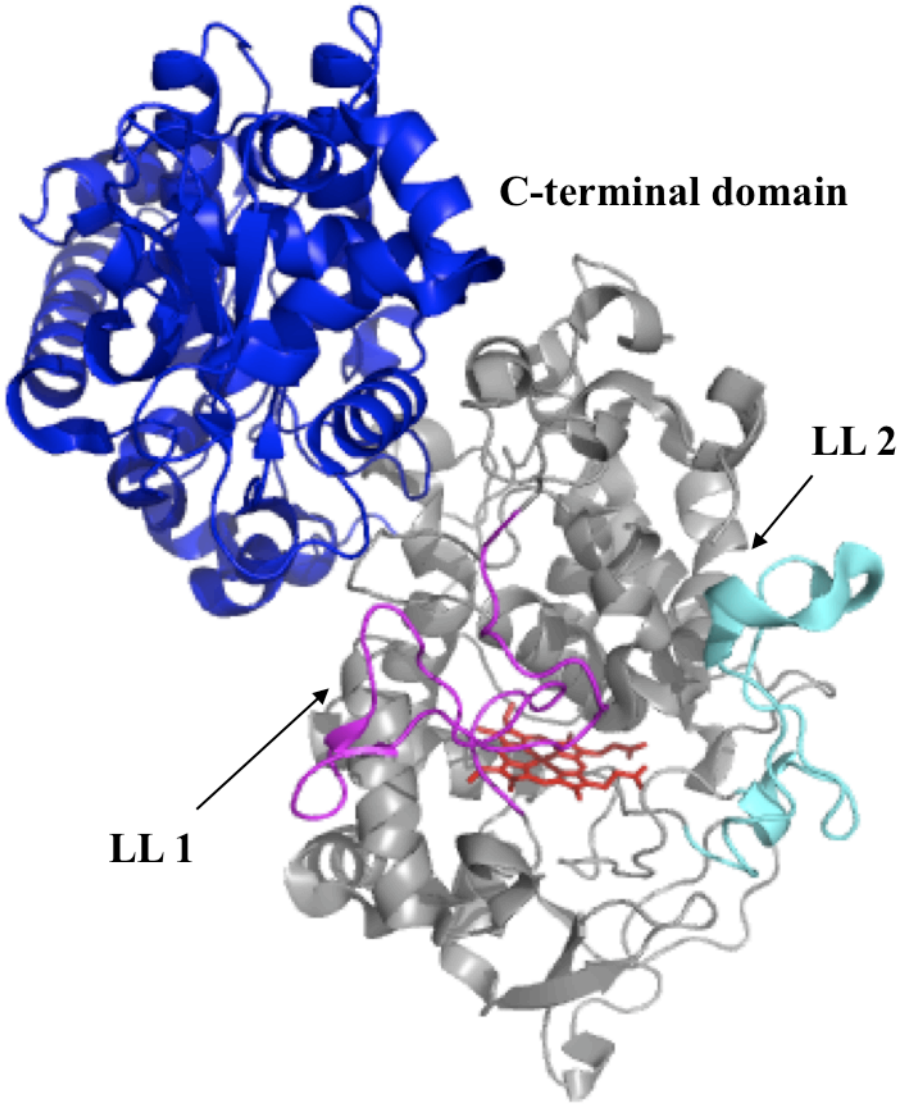

Figure 1.21: Structure of catalase-peroxidase.

KatG from *M. tuberculosis* (PDB: 1SJ2) [131].

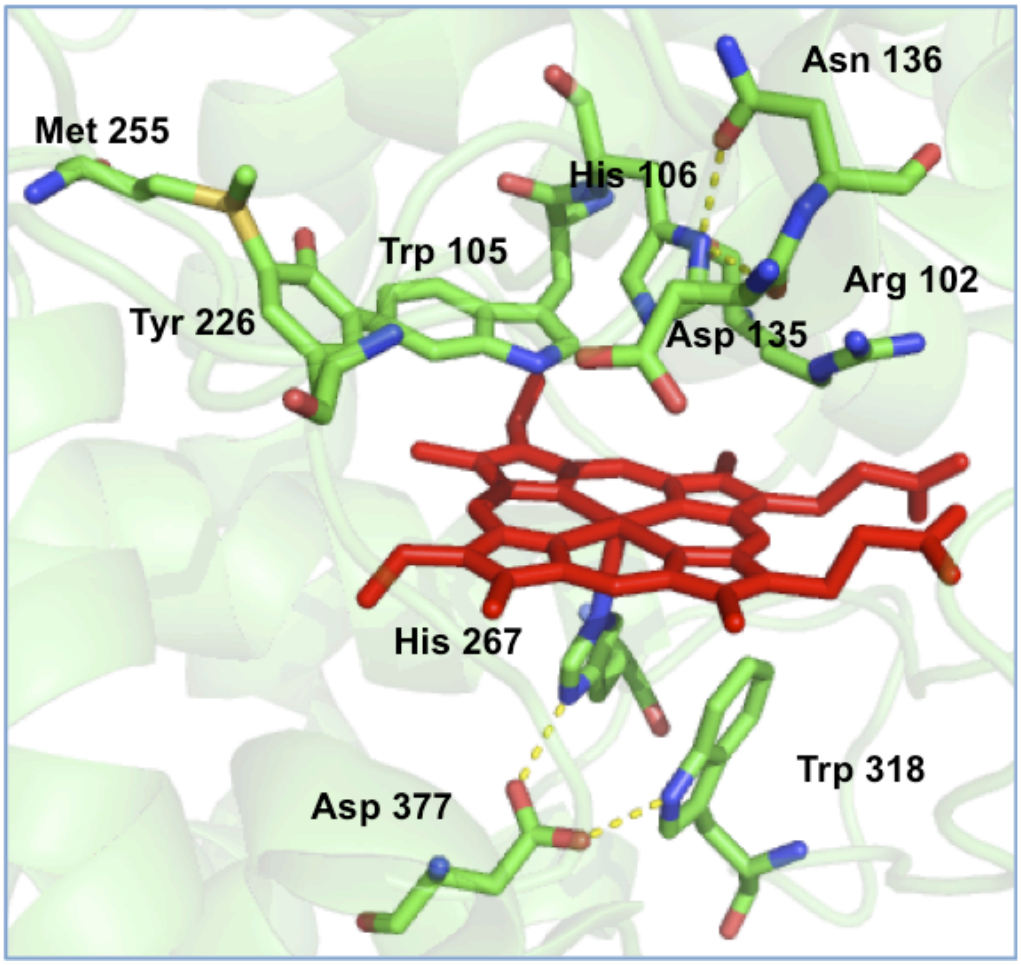

Figure 1.22: The covalent adduct in KatG.

KatG from *M. tuberculosis* (PDB: 1SJ2) (Numbering reflects *E.coli* structure of KatG) [131].

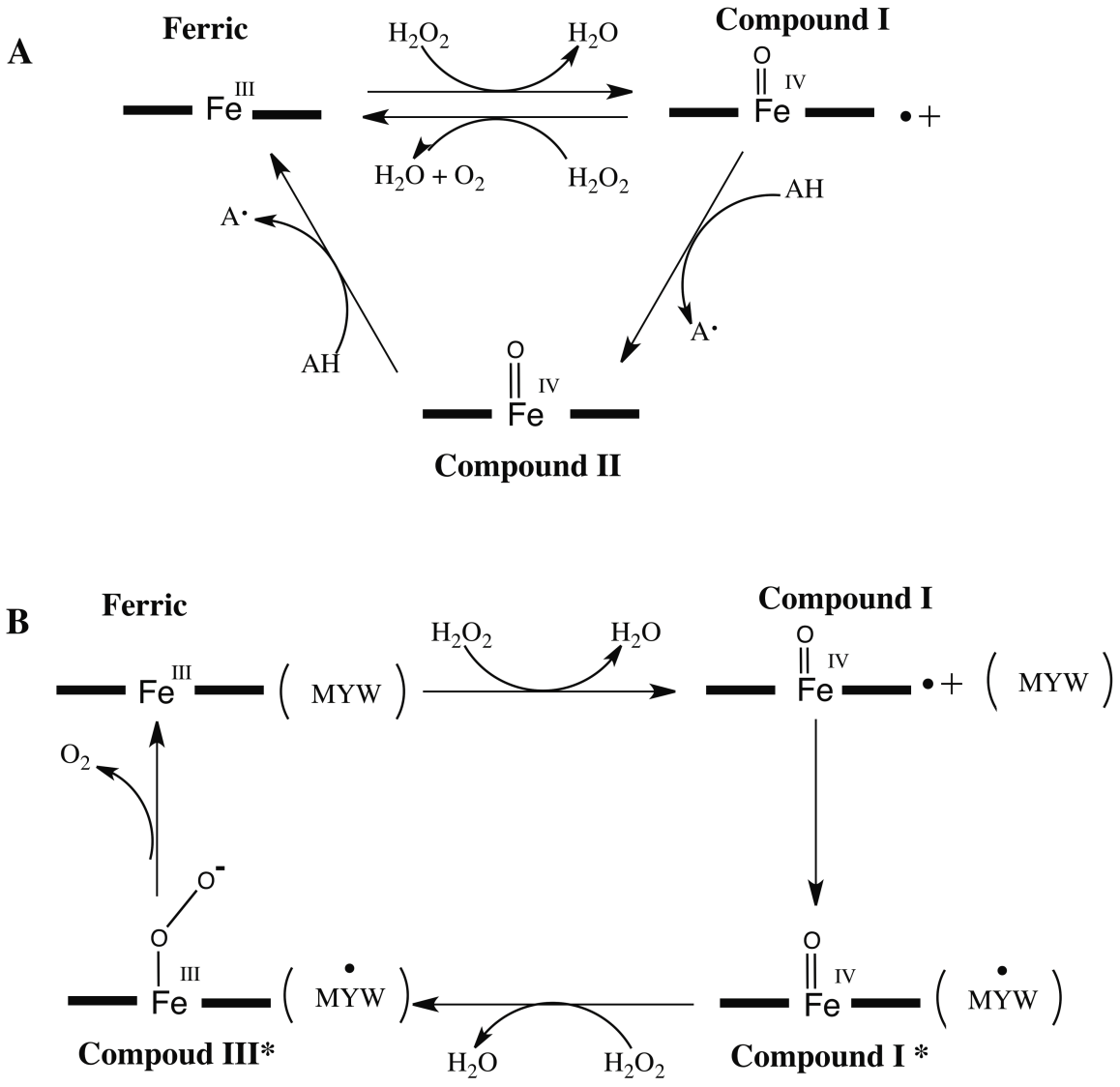

Figure 1.23: Classical model of catalytic cycle of KatG (A), modified model of catalase mechanism of KatG (B).

through a catalase or peroxidase cycle. However, this model cannot explain the role of M-Y-W adduct in the catalytic mechanism. In addition, recently, the Goodwin laboratory has reported the stimulation of catalase activity by classical peroxidatic electron donors rather than inhibition, particularly under conditions favorable to peroxidase activity. This is wholly inconsistent with the classical paradigm. One mechanism proposed for the catalatic turnover of KatG that accounts at least for the former observation has been proposed. By this mechanism compound I is converted to compound I* wherein the unique covalent adduct serves as an endogenous electron donor. An additional equivalent of H_2O_2 then converts compound I* to compound III*. Finally, the adduct radical serves as an electron acceptor returning the enzyme to its ferric state with the concomitant release of O_2 [137-140] (Fig. 1.23B).

1.4.4: The roles of C-terminal domain:

As mentioned above, all other members of the peroxidase-catalase superfamily are single domain proteins. Thus, the C-terminal domain, a structure ≥ 30Å from the active site, is unique to KatG. The structure is conserved across all KatGs. Based on its sequential and structural similarity to the N-terminal domain, the C-terminal domain is proposed to have originated from a gene-duplication and fusion event [118, 128, 141]. However, its roles in catalysis are not immediately obvious. Nevertheless, the Goodwin laboratory has observed that KatG without its C-terminal domain ($KatG^N$) is no longer expressed in a soluble form but is instead found in inclusion bodies. In addition, following denatured purification, refolding and reconstitution, $KatG^N$ shows a shifted active site structure, allowing what appears to be the direct coordination of the heme iron by the distal histidine (H106 by *Escherichia coli* numbering) [142]. Consequently, $KatG^N$ has neither catalase nor peroxidase activity. It has been suggested that the

C-terminal domain might serve as a platform to direct the proper folding of the N-terminal domain and facilitate dimerization [143]. This is supported by previous observations from the Goodwin laboratory [142, 144]. Introducing the separately expressed and isolated C-terminal domain ($KatG^C$) results in restructuring $KatG^N$ that is evident from a return of high-spin coordination states typical of the wild-type enzyme as well as the restoration of catalase and peroxidase activities [144]. Therefore, the C-terminal domain is an integral component of KatG intimately tied to its structure and function; this is also evident from a recent thermodynamic study of KatGs showing that the N- and C-terminal domains unfold as a single unit rather than independently [145].

However, the mechanism by which the C-terminal domain modulates the active site conformation is still not clear. Inspection of the crystal structures for various KatGs reveals that there are clear interactions between the two domains, which are proposed to contribute to the stability of the overall quaternary structure of the enzyme [119, 120, 122, 146]. As an extension of this hypothesis, it is reasonable to propose that the C-terminal domain, through these interactions, directs conformational adjustments in the adjacent domain including the active site itself. In order to evaluate the individual structures and mechanisms employed by the C-terminal domain, we focused our attention on a conspicuous structural element of this domain, the I'-helix (Chapter 2). Our results show that this helix is a central component of a platform to facilitate folding events and/or conformational adjustment in the N-terminal domain. Upon establishing the critical contributions of this structure, we turned our attention to understanding the mechanism(s) by which this remote structure communicates with and controls the active site (Chapter 3). The C-terminal domain has a unique evolutionary history. It was born in a gene-

duplication and fusion event. Either because the maintenance of its own catalytic function was unnecessary, or because a catalytically active C-terminal domain was a hindrance to the overall function of KatG, the specific structures necessary for heme binding and catalytic transformation of H_2O_2 were eliminated. Nevertheless, the general scaffold for a heme-based catalyst was retained to near perfection. We surmised that this provided an ideal avenue toward the creation of new heme protein-based catalysts. Our efforts and accomplishments in this direction are given in Chapter 4. Finally, our previous observations have shown that the C-terminal domain is essential for both catalase and peroxidase activities of KatG. It is also known that a novel covalent adduct in the N-terminal domain is critical, but only to the catalase activity of the enzyme. More importantly, the establishment of this adduct is both heme and peroxide dependent. This would suggest that the C-terminal domain is also essential for formation of the covalent adduct, but this has never been investigated. By way of a novel procedure to evaluate covalent adduct formation, we have determined that establishment of the covalent adduct cannot occur without the C-terminal domain (Chapter 5). It is noteworthy that although the C-terminal domain accounts for nearly half the structure of this important enzyme, prior to these investigations it remained the least understood of all of KatG's novel structural features. Together, these studies represent a substantial advance in understanding the function and potential applications of this important structure, and we anticipate that they will contribute not only to answering fundamental questions surrounding protein structure and function, but also to providing insight into the specific biomedical importance of KatG, in particular, its central involvement in *Mycobacterial* resistance to antibiotics and the virulence of pathogenic bacteria.

CHAPTER TWO

INTEGRAL ROLE OF THE I'-HELIX IN THE FUNCTION OF THE "INACTIVE" C-TERMINAL DOMAIN OF KATG

2.1 Introduction:

Catalase-peroxidases (KatGs) have been the subject of considerable attention since the discovery of their role in the activation of the frontline anti-tubercular agent isoniazid in *Mycobacterium tuberculosis* [105-107]. Catalase-peroxidases have also been implicated as virulence factors for some highly virulent pathogens such as *Yersinia pestis* [111-113], *Legionella pneumophila* [114]. Nevertheless, the mechanism by which these enzymes may serve as virulence factors have not been illuminated. Clearly, there are important benefits to be derived from understanding the structure and function of KatG.

Catalase-peroxidases are distributed among archaea, eubacteria, fungi and protists [93] primarily as hydrogen peroxide scavengers [147]. These enzymes use a single active site to degrade H_2O_2 by either a catalase or peroxidase mechanism. KatGs are either homodimers or homotetramers [148], and each subunit has two structurally homologous domains [118]. Neither domain bears any resemblance to monofunctional catalases; rather, both domains strongly resemble monofunctional peroxidases, bearing the same topological structure and similar helical structure around active sites [119-122]. Indeed, catalase-peroxidases belong to class I of the

peroxidase-catalase superfamily [118]. However, none of the other class I members (e.g., cytochrome *c* peroxidase [CCP] and ascorbate peroxidase [APX]) has appreciable catalase activity. Sequence alignments [118, 128] and the four available crystal structures of the KatGs [119-122] reveal several structural features that are unique to catalases-peroxidases. Two of them are Large Loop 1 (LL1) and Large Loop 2 (LL2). Relative to the class I enzymes, each one adds about 35 amino acids to the interhelical loops connecting the D and E helices and F and G helices, respectively. Likewise, other peroxidases are single-domain proteins, making the 300-amino acid C-terminal domain another unique feature of KatGs. It may be the persistence of the longer interhelical loops, both of which are essential for catalase but not peroxidase activity [132, 134, 149-151], along with the necessity for a precisely ordered active site to support catalase activity [145] that has compelled the continued presence of the C-terminal domain in KatG but not its most closely related neighbors CcP and APx.

The C-terminal domain is ≥ 30Å from the active site. It is conserved across all catalase-peroxidases, and based on its sequential and structural similarity to the N-terminal domain, is proposed to have originated from a gene-duplication and fusion event [118, 128]. However, its roles in catalysis are not immediately obvious. It bears a striking resemblance to monofunctional peroxidases [119-122, 143], but it neither binds heme nor catalyzes any discernable reaction. It is proposed that the class I enzymes were all derived from a two-domain predecessor, suggesting that deletion of one of the domains was a necessary step in the development of CcP and APx [92]. In this, the C-terminal domain has the appearance of a vestigial structure.

Contrary to this notion, KatG without its C-terminal domain ($KatG^N$) is no longer expressed in a soluble form but is instead found in inclusion bodies. In addition, following denatured purification, refolding and reconstitution, $KatG^N$ shows a shifted active site structure, allowing what appears to be the direct coordination of the heme iron by the distal histidine (H106 by *Escherichia coli* numbering) [142]. Consequently, $KatG^N$ has neither catalase nor peroxidase activity. It has been suggested that the C-terminal domain might serve as a platform to direct proper folding of the N-terminal domain and facilitate dimerization [143], which is supported by our previous observation. Introducing the separately expressed and isolated C-terminal domain ($KatG^C$) results in restructuring of $KatG^N$ that is evident from a return of high-spin coordination states typical of wild-type enzyme as well as the restoration of catalase and peroxidase activities [144]. That the C-terminal domain is an integral component of KatG intimately tied to its structure and function is also evident from a recent thermodynamic study of KatGs showing that the N- and C-terminal domains unfold as a single unit rather than independently [145].

The I′-helix in the C-terminal domain is highly conserved and appears at the interface between the two domains. It makes contacts with several elements from the N-terminal domain of the adjacent subunit using strongly conserved Leu 690, Arg 691, Glu 695, and Tyr 697. As such, it has all the appearances of a platform by which the C-terminal domain may direct structural adjustments to the N-terminal domain thereby modulating active site conformation. To evaluate this hypothesis, we produced variants substituting alanine for these conserved residues. Single, double, and quadruple alanine substitution variants of intact KatG were expressed, isolated and characterized, and the effects of these substitutions on active site structure, stability and catalytic bifunctionality were evaluated. In addition, the analogous variants were also

expressed and isolated for the stand-alone C-terminal domain ($KatG^C$). The ability of these $KatG^C$ variants to restore $KatG^N$ to an active conformation was evaluated. Results from both sets of variants demonstrate that the I′-helix is central to the ability of the C-terminal domain to direct structural adjustments in the adjacent N-terminal domain. This supports the hypothesis that the C-terminal domain serves as a platform to direct N-terminal domain active site conformation and bifunctionality.

2.2 Materials and methods:

2.2.1 Materials:

Hydrogen peroxide (30%), imidazole, hemin, ampicillin, chloramphenicol, sodium dithionite, phenylmethylsulfonyl fluoride (PMSF), 2,2′-azino-bis(3-ethylbenzthiazoline-6-sulfonate) (ABTS), and guanidine hydrochloride (GuHCl) were purchased from Sigma (St. Louis, MO). Isopropyl-β-d-thiogalactopyranoside (IPTG), urea, mono- and dibasic sodium phosphate, acetic acid, and sodium acetate were obtained from Fisher (Pittsburgh, PA). Bugbuster and benzonase were purchased from Novagen (Madison, WI). All restriction enzymes were purchased from New England Biolabs (Beverly, MA). All oligonucleotide primers were purchased from Invitrogen (Carlsbad, CA). All *E. coli* strains (BL-21-Gold [DE3] pLysS and XL-1 Blue), *Pfu* polymerase, and T4 DNA ligase were obtained from Agilent (La Jolla, CA). Nickel-nitrilotriacetic acid (Ni-NTA) resin was purchased from Qiagen (Valencia, CA). Desalting 10DG chromatography columns were purchased from Bio-Rad. All buffers and media were prepared using water purified through a Barnstead EasyPure II system (18.2 MΩ/cm resistivity).

2.2.2 Cloning:

All plasmids were prepared using mutagenic coding and non-coding primers (Table 2.1) according to the Round-the-Horn procedure [152]. Amplification products were subjected to blunt-end ligation with T4 DNA ligase and used to transform *E. coli* (XL-1 Blue) by heat shock according to manufacturer instructions, and transformants were selected on the basis of ampicillin resistance. Plasmids from candidate colonies were isolated and evaluated by diagnostic restriction digest (Table 2.1) and DNA sequence analysis (Davis Sequencing, Davis, CA). Plasmids verified to carry the correct mutations were used to transform *E. coli* (BL-21-Gold [DE3] pLysS).

2.2.3 Expression and purification:

All expression was carried out in *E. coli* (BL-21-Gold [DE3] pLysS) cells using liquid Luria–Bertani broth supplemented with ampicillin and chloramphenicol with constant agitation. Wild-type KatG was over-expressed in a soluble form as previously described [151]. However, substituting any one of the four strictly conserved residues resulted in accumulation of target protein in inclusion bodies so long as expression was carried out at 37 °C. Upon adjusting the temperature to 18 °C, a substantial proportion (~ 60%) of expressed protein was produced in a soluble state for all $KatG^C$ variants. Likewise, R691A, E695A, Y697A, and L690A/R691A variants of intact KatG were expressed in a soluble form at appreciable levels (40–60%) at 18 °C. Interestingly, the L690A variant of intact KatG was only observed in inclusion bodies even at alternative expression temperatures. In all cases, expression was induced with IPTG once cells had reached mid-log phase (OD_{600} = 0.4). At 10 h post-induction, cells were harvested by centrifugation, and cell pellets were stored at − 80 °C until purification. Expression analysis was

Table 2.1: Primer sets for site-directed mutagenesis of I'-helix.

Protein:	Primer Sequences:	Restriction enzymes
L690A	5'-Phos-CTTGCGGTGGCGGAAGTTACGCC-3' 5'-Phos-TGCGACGGAGTTAGAACCAAACACCAGATCCG-3'	*PmI I*
R691A	5'-Phos-GCGGTGGCGGAAGTTTACGCCAGT-3' 5'-Phos-GGCCAGGACGGAGTTAGAACCAAACACCAGA-3'	*Sac II*
E695A	5'-Phos-GCAGTTTACGCCAGTAGCGATGCCCACG-3' 5'-Phos-AGCCACCGCACGCAGGACGGAGTTA-3'	*Pst I*
Y697A	5'-Phos-GAAGTTGCAGCCAGTAGCGATGCCCACG-3' 5'-Phos-AGCCACCGCACGCAGGACGGAGTTA-3'	*N/A*
L690A/R691A	5'-Phos-CGCGGTGGCGGAAGTTTACGCCAGT-3' 5'-Phos-GCCGCGACGGAGTTAGAACCAAACACCAG-3'	*Sac II*
E695A/Y697A	5'-Phos-GCAGTTGCAGCCAGTAGCGATGCCCACG-3' 5'-Phos-AGCCACCGCACGCAGGACGGAGTTA-3'	*Pst I*
L690/R691A/ E695A/Y697A	5'-Phos-CGGTGGCTGCAGTTGCCGCCAGTAG-3' 5'-Phos-CGGCCGCGACGCAGTTAGAACCAAACAC-3'	*Sac II*

performed using a trichloroacetic acid precipitation technique that we have described elsewhere [153].

Purification of variants expressed at 18 °C began by resuspending the cell pellets in Bugbuster reagent (Novagen, Madison, WI) in the presence of PMSF (0.1 mM) and benzonase nuclease (250 U). The cell lysate was centrifuged, and the supernatant loaded onto a Ni-NTA column by recirculating the solution with a flow rate of 1 mL/min through the column overnight. Following loading, the column was washed in succession with buffer A (50 mM Tris, pH 8.0), buffer B (50 mM phosphate buffer, pH 7.0, 200 mM NaCl), buffer B supplemented with 2 mM imidazole, and buffer B supplemented with 20 mM imidazole. The target protein was then eluted from the column using buffer B with 50 mM imidazole, and finally, buffer B with 200 mM imidazole. Excess imidazole was then removed by gel filtration using a 10DG column from BioRad. The eluted fractions were collected and analyzed by SDS-PAGE. Protein-containing fractions were combined, concentrated, aliquotted, and stored at − 80 °C. Concentrations of purified proteins were estimated according to the method of Gill and von Hippel [154]. Even though no heme precursors had been added to the expression media, a small portion of the purified enzyme already had heme incorporated while inside the cells.

The variants $KatG^N$, E695A/Y697A KatG and L690A/R691A/E695A/Y697A KatG were expressed in insoluble inclusion bodies. Purification was carried out as previously described for $KatG^N$ [142] with the following modifications. After the centrifugation of the cell lysate, the insoluble pellet was resuspended using 8 M urea in buffer B. Likewise, the initial washing of the loaded Ni-NTA column was carried out using 8 M urea in buffer B supplemented with 10 mM imidazole. Elution of the protein from the Ni-NTA column was accomplished with 8 M urea in

buffer B supplemented with 400 mM imidazole. The eluent was then pooled and dialyzed against buffer B (24–30 h; five changes). With these modifications to the purification procedure, we obtained $KatG^N$ with a greater capacity for reactivation by $KatG^C$ than previously observed [144] as determined by visible absorption, MCD, and EPR spectroscopies as well as catalase and peroxidase activities.

2.2.4 Enzyme reconstitution and absorption spectra:

Due to its poor solubility in neutral and acidic solutions, hemin was dissolved in 0.1 M KOH. The concentration of hemin stock solutions was determined by the method of Falk [155]. Hemin (0.75 equivalents) was added to wild-type KatG, intact I′-helix variants, and $KatG^N$. These solutions were allowed to incubate for at least 24 h at 4 °C. These solutions were then centrifuged to remove insoluble unincorporated heme and other debris. The final concentration of incorporated hemin was determined by the pyridine hemichrome method of Falk [30]. and used to calculate molar absorptivities of the heme absorption spectra of each protein. Spectra for the ferrous states of these proteins were obtained by adding a small amount (< 10 mg) solid dithionite to the ferric form of each. All spectra were obtained at room temperature on a Shimadzu UV-1601 spectrophotometer (Columbia, MD) with a cell path length of 1.0 cm.

2.2.5 Domain mixing and incubation procedures:

The concentrations of $KatG^N$, $KatG^C$, and $KatG^C$ variants were estimated based on their molar absorptivities as follows: $KatG^N$ ($\varepsilon 416 = 98\ mM^{-1}\ cm^{-1}$); $KatG^C$, L690A $KatG^C$, R691A $KatG^C$, E695A $KatG^C$, and L690A/R691A $KatG^C$ ($\varepsilon 280 = 34\ mM^{-1}\ cm^{-1}$); and Y697A $KatG^C$, E695A/Y697A $KatG^C$, and L690A/R691A/E695A/Y697A $KatG^C$ ($\varepsilon 280 = 33\ mM^{-1}\ cm^{-1}$).

Solutions containing 1:1 ratios of $KatG^N$ and $KatG^C$ or one of its variants were incubated for times ranging from 0 to 96 h in the presence of 50 mM phosphate buffer, pH 7.0, 50 mM NaCl at 4 °C. Optimal results were obtained with freshly purified and reconstituted $KatG^N$ and freshly purified $KatG^C$.

2.2.6 Catalase and peroxidase activity assays:

Peroxidase activity was evaluated by monitoring the production of the ABTS radical over time at 417 nm ($34.7\ mM^{-1}\ cm^{-1}$) [156]. All assays were carried out at room temperature in 50 mM acetate buffer, pH 5.0. Catalase activity was evaluated by monitoring the decrease in H_2O_2 concentration with time at 240 nm ($39.4\ M^{-1}\ cm^{-1}$) [157]. All assays were carried out at room temperature in 100 mM phosphate buffer, pH 7.0. Initial velocities ($v_o/[E]_T$) were fit to a Michaelis–Menten equation (Eq. (1)) by non-linear regression analysis to determine apparent kinetic parameters k_{cat}, K_M, and k_{cat}/K_M.

$$v_o/[E]_T = \frac{k_{cat}[S]}{K_M + [S]} \quad (1)$$

Here, $[E]_T$ is determined on the basis of the heme content of the protein(s) present. In all instances reported here, k_{cat} is the asymptotic maximum catalytic output, the apparent K_M simply corresponds to the concentration of substrate necessary to produce $v_o/[E]_T$ equal to ½ k_{cat}, and k_{cat}/K_M, the apparent second-order rate constant, represents the efficiency with which the substrate is processed and corresponds to the slope of the tangent line to rates obtained at low [S] (i.e., $<K_M$). When evaluating peroxidase activity as a function of H_2O_2 concentration, H_2O_2-dependent inhibition was frequently observed. In order to account for the inhibitory effect and make accurate determinations of the apparent parameters k_{cat}, K_M, and k_{cat}/K_M, the data were fit

to Eq. (2) derived from a general model for substrate-dependent inhibition[158], where K_I is an apparent dissociation constant corresponding to inhibition due to the substrate.

$$v_o/[E]_T = \frac{k_{cat}[S]}{K_M + [S] + [S]^2/K_I} \quad (2)$$

2.3.7 Circular dichroism spectropolarimetry:

Far-UV (190–300 nm) circular dichroism (CD) spectra were recorded using a Jasco J-810 spectropolarimeter (Tokyo, Japan). To minimize buffer interference at wavelengths below 200 nm, all spectra were recorded using 5 μM enzyme in the presence of 5 mM phosphate buffer, pH 7.0, and Suprasil quartz cells (0.1 mm path length). All spectra were recorded at 23 °C.

2.2.8 Magnetic circular dichroism (MCD):

All spectra of intact wild-type KatG and its variants were obtained using 15 μM of enzyme. Spectra for $KatG^N$ alone or incubated with $KatG^C$ or one of its variants were obtained using 10 μM $KatG^N$. All concentrations were determined on the basis of heme content. Spectra (700–350 nm) were recorded in the presence of 50 mM phosphate buffer, pH 7.0 and 50 mM NaCl at 23 °C on a Jasco J-810 spectropolarimeter equipped with a magnetic cell holder (1.4 T) (Tokyo, Japan). Baseline subtraction and spectral analysis were carried out using Jasco J-720 software. The ferrous states of all heme-containing variants/domain combinations were prepared by adding a small amount (< 10 mg) of sodium dithionite to the ferric state.

2.2.9 Electron Paramagnetic Resonance (EPR):

Spectra were recorded using a Bruker EMX instrument equipped with an Oxford ESR 900 cryostat and ITC temperature controller. Additional sample concentration was performed using Amicon Ultra-4 centrifugal devices. The settings for the spectrometer were as follows: temperature, 10 K; microwave frequency, 9.38 GHz; microwave power, 0.1 mW; modulation amplitude, 10 G; modulation frequency, 100 kHz; time constant, 655.36 ms; conversion time, 655.36 ms; and receiver gain, 1.0×10^5. Spin quantification was carried out using the Biomolecular EPR Spectroscopy Software package available online [159, 160].

2.2.10 GuHCl-mediated protein unfolding:

The effect of GuHCl on the stability of wtKatG and its I′-helix variants was evaluated by two methods. The first method monitored the loss of heme from the active site using a SX.18MV (PC upgrade) stopped-flow rapid reaction analyzer (Applied Photophysics, Surrey, UK) equipped with diode array detection. One syringe contained 2 μM wtKatG (or one of its variants) and the second syringe contained GuHCl (from 1.5 to 6 M). The *k*obs values for heme loss were determined from the decrease in absorbance at 413.9 nm. All reactions were carried out at 23 °C in 50 mM phosphate pH 7.0. The GuHCl-dependent disruption of the overall secondary structural content of KatG and its I′ helix variants was monitored by far UV (250–190 nm) CD spectroscopy. All reactions were carried out in the presence of 5 mM phosphate buffer, pH 7.0, and contained 5 μM enzyme except for $KatG^N$, E695A/Y697A KatG and L690A/R691A/E695A/Y697A KatG, which contained 10 μM protein. Each spectrum was corrected using a baseline spectrum obtained using phosphate buffer alone.

2.2.11 Temperature-mediated protein unfolding:

Thermal denaturation of KatG at the active-site level was monitored by visible absorption due to the heme prosthetic group. Intact KatG and its I′-helix variants (10 μM) were incubated across a temperature range from 0 to 70 °C in 50 mM phosphate buffer, pH 7.0. For each measurement, enzymes were incubated at the target temperature for 10 min at which point spectra were recorded. Due to protein aggregation at high temperature, all spectra were background corrected based on their absorbance at 450 nm.

2.2.12 Calculation of thermodynamic parameters:

The fraction (α) of unfolded protein at each temperature (T) was calculated from the absorbance of the Soret λmax of the native enzyme according to Eq. (3), where A represents the absorbance at a given temperature, A_N is the absorbance value for the native state, and A_U is the absorbance of the unfolded state. Similarly from CD data, α was calculated according to Eq. (4), where θ_N is the ellipticity at 222 nm for the native folded state, θ is the ellipticity at a given GuHCl concentration, and θ_U is the ellipticity at 222 nm for the unfolded state. Assuming a two-state model, where N is the native protein and U is the unfolded protein, the equilibrium constant between the unfolded and native state is given by Eq. (5) [161, 162]. This is related to the standard free energy of denaturation according to Eq. (6), where R is the universal gas constant (8.3145 J mol^{-1} K^{-1}) and T is the absolute temperature. In unfolding experiments with chaotropic reagents performed at 25 °C (298.13 K), there is generally a linear relationship between ΔG° and denaturant concentration, allowing for extrapolation [145, 163] to obtain $\Delta G°_{H2O}$ (see Eq. (7)). Here $\Delta G°_{H2O}$ is the value of ΔG° in the absence of denaturant and *m* reflects the efficacy of the denaturant for unfolding [145].

$$\alpha = (A_N - A)/ (A_N - A_U) \quad (3)$$

$$\alpha = (\theta_N - \theta)/(\theta_N - \theta_U) \quad (4)$$

$$K = [U] / [N] = \alpha/(1 - \alpha) \quad (5)$$

$$\Delta G° = - RT \ln K \quad (6)$$

$$\Delta G° = \Delta G°_{H2O} - m[\text{denaturant}] \quad (7)$$

2.3 Results:

2.3.1 Mutagenesis, expression and purification of KatG and KatG^C I'-helix variants:

As confirmed by DNA sequence analysis, we successfully produced constructs for expression of seven alanine substitutions involving four intersubunit interface residues: L690, R691, E695 and Y697. All I'-helix variants as well as wtKatG and KatG^N were successfully expressed and isolated. Far-UV CD spectra for I'-helix variants of intact KatG and KatG^C were indistinguishable from those obtained for wtKatG and unmodified KatG^C, repectively, indicating that substitutions did not disrupt protein secondary structural content of proteins (Fig. 2.1).

2.3.2 Spectroscopic properties of I'-helix KatG variants

UV-visible absorption spectra (Fig. 2.2) for single substitution variants E695A and Y697A KatG were very similar to the wild-type enzyme with Soret band maxima between 406 and 407 nm and charge transfer transitions around 505 and 640 nm. The spectrum for R691A KatG was also very similar except for a more prominent shoulder at 380 nm consistent with a greater contribution from pentacoordinate rather than hexacoordinate high-spin heme. By contrast, the double (L690A/R691A and E695A/Y697A) and quadruple (L690A/R691A/E695A/Y697A)

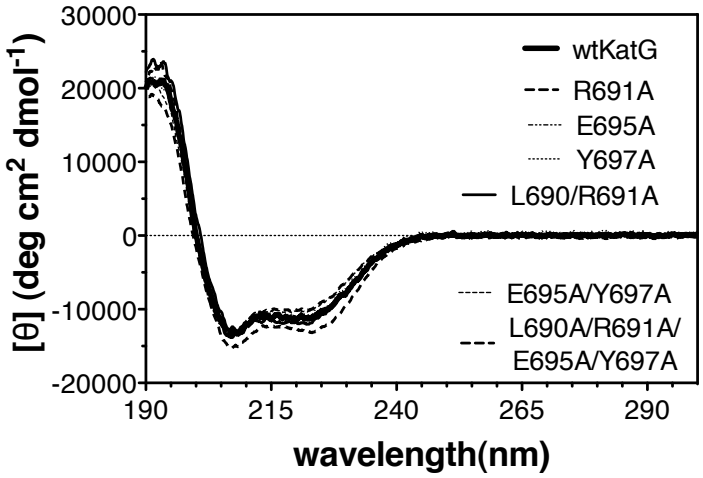

Figure 2.1A

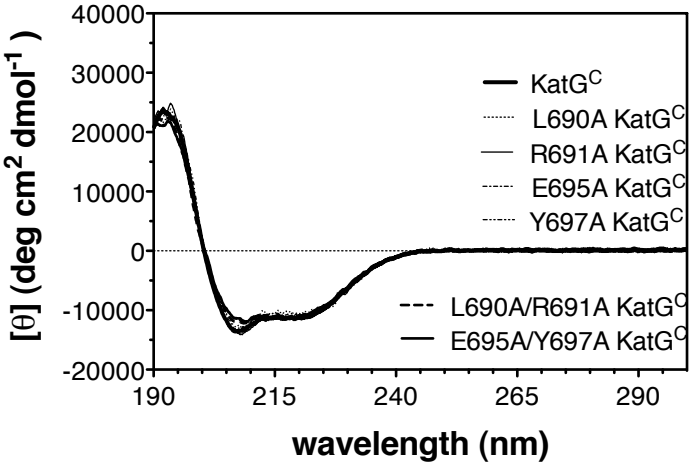

Figure 2.1B

Figure 2.1: (A) Far-UV circular dichroism of *wtKatG*, and I'helix variants. (B) Far-UV circular dichroism of C-terminal domain I'helix variants and KatG^{C}.

Spectra were recorded at 23 °C in 5mM phosphate buffer, pH 7.0 using a 0.5 mm quartz cell.

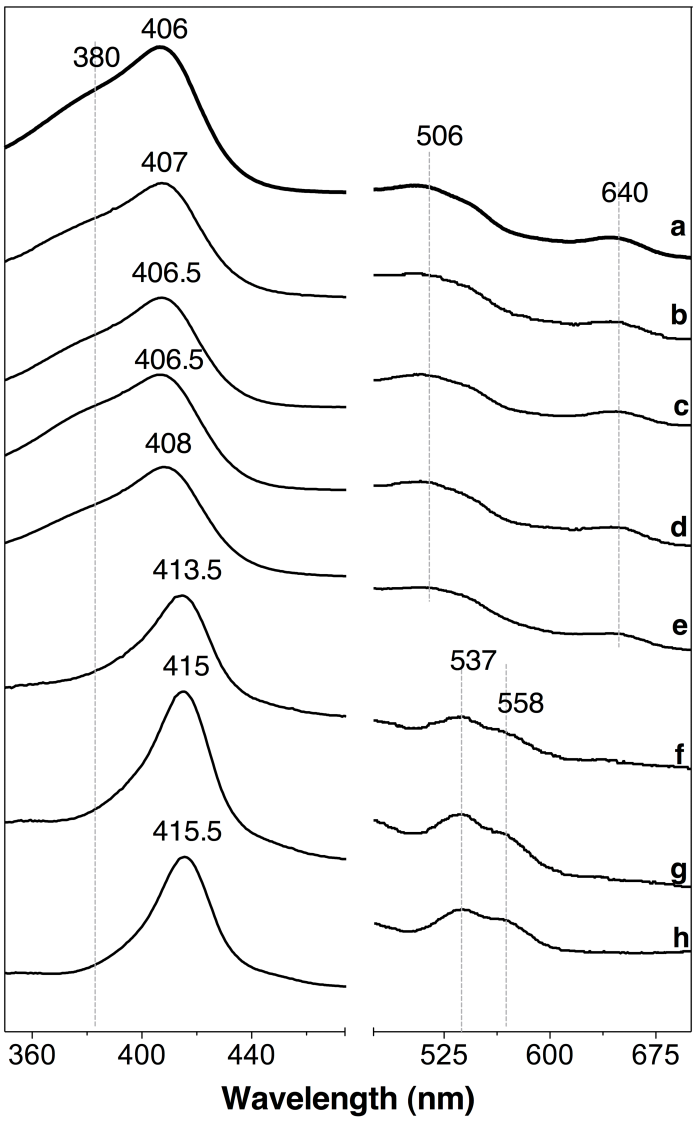

Figure 2.2: Absorption spectra of ferric wtKatG, its I′-helix substitution variants, and KatG^N.

Spectra were recorded for wtKatG (a), Y697A (b), E695A (c), R691A (d), L690A/R691A (e), E695A/Y697A (f), L690A/R691A/E695A/Y697A (g), and KatG^N (h).

variants all showed a red shift in the Soret band, increased contributions from the β and α bands (538 nm and 558 nm respectively) and diminished intensity of the charge transfer transitions. The effect was more modest for the L690A/R691A variant but progressively more dramatic for E695A/Y697A and the quadruple variant. These results were consistent with a progressively greater contribution from hexacoordinate low-spin heme to the spectra.

In order to more effectively differentiate the high-spin and low-spin state contributions of these variants, we obtained magnetic circular dichroism (MCD) spectra (Fig. 2.3). Particularly with the ferrous oxidation state, the differences between high-spin and low-spin are pronounced and easily distinguished. Spectra for the low-spin state shows an intense band with a maximum near 550 nm [164]. The dominant feature in the ferrous MCD spectra for all the single substitution variants was the B-term features near 440 nm with little if any contribution from the A-term feature centered at 557 nm. The A-term became more pronounced and the 440 nm B-term less pronounced for the double and quadruple variants. These shifts were most subtle for the L690A/R691A variant, but spectra for E695A/Y697A KatG and the quadruple variant were dominated by features consistent with hexacoordinate low-spin heme. Nevertheless, even with the quadruple variant there was a detectable (albeit minor) contribution from high-spin species (Fig. 2.3).

More definitive assessments of the distribution of heme states were obtained from EPR spectra (Fig. 2.4). The wild-type and single substitution variants were all dominated by high-spin species with little contribution from hexacoordinate low-spin complexes. Further, as is typically observed, more than one high-spin complex was detected [142, 165-167]. For L690A/R691A,

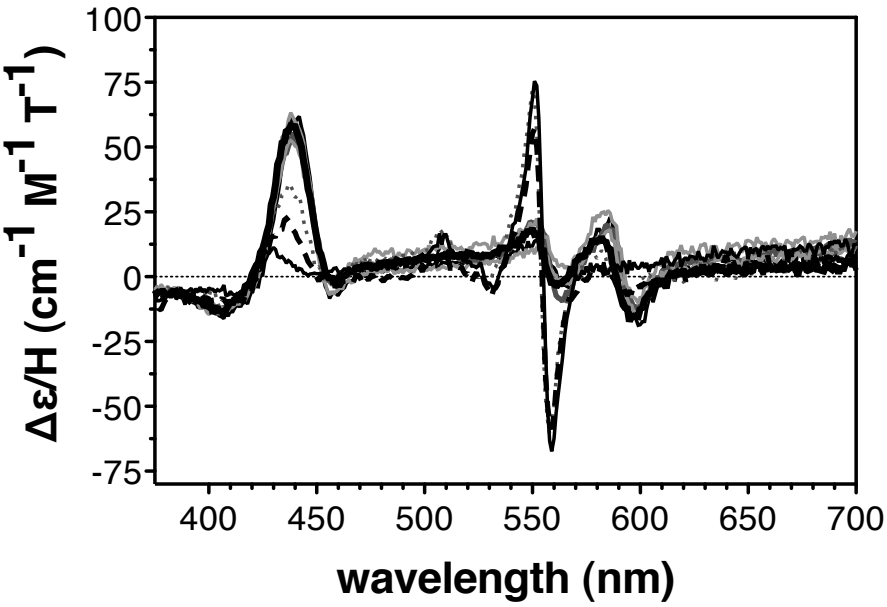

Figure 2.3: MCD spectra of ferrous wtKatG, KatG^N and I'helix substitution variants.

Spectra were recorded for 15 μM wtKatG (bold line), KatG^N (solid line), E695A/Y697A (dotted line), L690A/R691A/E695A/Y697A (dashed line), Y697A, E695A, R691A, L690A/R691A (grey solid lines), in presence of 50 mM phosphate 50 mM NaCl, pH 7.0 using a 5.0 quartz cell in a 1.4 T magnetic cell holder.

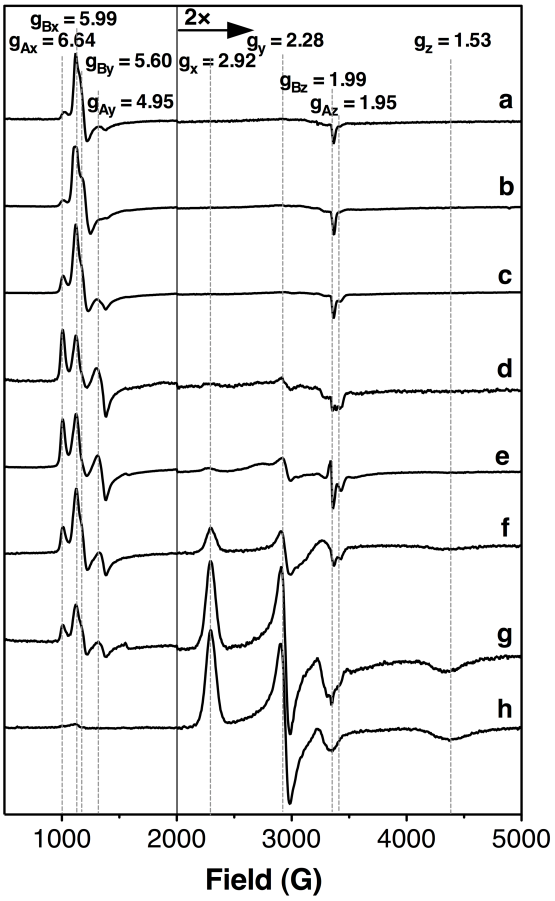

Figure 2.4: EPR spectra recorded for wtKatG, its I′-helix substitution variants, and KatG^N. Spectra for ferric wtKatG (a), Y697A (b), E695A (c), R691A (d), L690A/R691A (e), E695A/Y697A (f), L690A/R691A/E695A/Y697A (g), and KatG^N (h) are shown. Spectrometer settings were as follows: temperature, 10 K; microwave frequency, 9.38 GHz; microwave power, 0.1 mW; modulation amplitude, 10 G; modulation frequency, 100 kHz. The g-values corresponding to RHS 1 (g_{Ax}, g_{Ay}, and g_{Az}) and RHS 2 (g_{Bx}, g_{By}, and g_{Bz}) are shown as those of the hexacoordinate low spin complex (g_x, g_y, and g_z)

E695A/Y697A and the quadruple variant, there was a progressively diminishing contribution from the high spin states as well as an increasing contribution from the hexacoordinate low-spin complex. To quantify the relative proportions of each species, the spectra were simulated and the individual signals were integrated (Table 2.2). The simulations shown used two rhombic high-spin species (RHS) (RHS 1: g_x=6.64, g_y=4.95 and g_z=1.95; RHS 2: g_x=5.99, g_y=5.60 and g_z=1.99) and one low-spin signal (g_x =2.92, g_y =2.28, g_z =1.53). The simulations were also carried out using an additional axial high-spin component similar to that described by Svistunenko et al. [167], but these did not appreciably change our principal observations. Species producing features like RHS 1 have typically been assigned as pentacoordinate high-spin, whereas those corresponding to RHS 2 are attributed to a hexacoordinate high-spin state [165-167]. Wild-type (70%), Y697A (77%) and E695A (56%) were all dominated by RHS 2. The R691A variant was dominated by RHS 1 (62%) with a modest contribution from the low-spin state (14%). Interestingly, the other variant bearing an R691 substitution L690A/R691A was also dominated by RHS 1 (55%), but had a greater contribution from the low-spin state (25%). For E695A/Y697A (47%) and the quadruple variant (88%), the most abundant component was the hexacoordinate low-spin complex. But for small contribution from RHS 1 (6%) and RHS 2 (6%) the latter closely resembled the exclusively hexacoordinate low-spin spectrum of $KatG^N$.

2.3.3 Steady-state kinetics of I'-helix KatG variants

Single substitutions to I'-helix residues caused only modest changes in catalase activity as determined by comparing apparent k_{cat} and k_{cat}/K_M values (Table 2.3). Even the double variant

Table 2.2: Ratios of EPR signals observed for wtKatG, its I′-helix variants, and $KatG^N$.

Protein	**% contribution**		
	HS [a] : LS [b]	RHS 1 [c]: RHS 2 [d]	RHS 1: RHS 2 : LS
wtKatG	92 : 8	24 : 76	22 : 70 : 8
R691A	86 : 14	72 : 28	62 : 24 : 14
E695A	96 : 4	42 : 58	40 : 56 : 4
Y697A	93 : 7	18 : 82	16 : 77 : 7
L690A/R691A	75 : 25	69 : 31	55 : 20 : 25
E695A/Y697A	53 : 47	57 : 43	30 : 23: 47
L690A/R691A/E695A/Y697A	12 : 88	53 : 47	6 : 6 : 88
$KatG^N$	0 : 100	0 : 0	0 : 0 : 100

[a] : High Spin; HS = RHS 1+RHS 2

[b] : Low Spin (g_x =2.92 , g_y =2.28 , g_z =1.53)

[c] : Rhombic high-spin species 1 (g_x=6.64, g_y=4.95 and g_z=1.95)

[d] : Rhombic high-spin species 2 (g_x=5.99, g_y=5.60 and g_z=1.99)

Table 2.3: Apparent catalase kinetic parameters for wtKatG and its I′-helix variants [a]

Protein	**Parameter**		
	k_{cat} (s^{-1})	K_M (mM H_2O_2)	k_{cat}/K_M (M^{-1} s^{-1})
wtKatG	11500 ± 200	4.5 ± 0.2	2.5×10^6
R691A	6800 ± 300	2.7 ± 0.3	2.5×10^6
E695A	8900 ± 500	2.9 ± 0.4	3.1×10^6
Y697A	8300 ± 300	1.9 ± 0.2	4.4×10^6
L690A/R691A	4800 ± 300	2.7 ± 0.4	1.7×10^6
E695A/Y697A	1020 ± 70	1.2 ± 0.3	0.85×10^6
L690A/R691/E695A/Y697A	160 ± 30	2.2 ± 1.2	0.07×10^6

[a] Assay included 20 nM enzyme in 100 mM phosphate buffer, pH 7.0, 23 °C.

Table 2.4: Apparent peroxidase kinetic parameters for wtKatG and its I′-helix variants[a]

Protein	**Peroxide-dependent peroxidase parameters**			
	k_{cat} (s^{-1})	K_M (mM H_2O_2)	k_{cat} K_M (M^{-1} s^{-1})	K_i (mM H_2O_2)
wtKatG	65.0 ± 6.0	0.180 ± 0.040	3.60×10^5	2.90 ± 1.0
R691A	105.5 ± 12	0.170 ± 0.040	6.20×10^5	3.35 ± 0.9
E695A	58.8 ± 5.1	0.133 ± 0.034	4.41×10^5	4.64 ± 1.0
Y697A	94.7 ± 4.9	0.103 ± 0.019	9.19×10^5	8.51 ± 1.4
L690A/R691A	66.9 ± 6.9	0.218 ± 0.053	1.08×10^5	5.26 ± 1.3
E695A/Y697A	7.81 ± 0.7	0.070 ± 0.020	3.06×10^5	7.82 ± 2.1
L690A/R691A/E695A/Y697A	0.74 ± 0.1	4.70 ± 0.080	0.02×10^4	-
Protein	**ABTS-dependent peroxidase parameters**			
	k_{cat} (s^{-1})	K_M(mM ABTS)	k_{cat} /K_M (M^{-1} s^{-1})	Ki (mM ABTS)
wtKatG	55.2 ± 1.3	0.087 ± 0.008	6.34×10^5	-
R691A	75.5 ± 5.8	0.154 ± 0.025	4.92×10^5	5.96 ± 2.1
E695A	57.6 ± 5.2	0.078 ± 0.019	7.38×10^5	4.4 ± 1.8
Y697A	72.0 ± 1.5	0.081 ± 0.007	8.89×10^5	-
L690A/R691A	46.7 ± 2.6	0.087 ± 0.012	5.37×10^5	8.27 ± 3.2
E695A/Y697A	6.21 ± 0.2	0.030 ± 0.007	2.07×10^5	-
L690A/R691A/E695A/Y697A	0.26 ± 0.1	0.007 ± 0.007	0.37×10^5	-

[a] Assay included 20 nM enzyme in 50 mM acetate buffer, pH 5.0 23 °C.

L690A/R691A retained about half the catalase activity of the wild-type enzyme. However, the apparent k_{cat} values for E695A/Y697A and the quadruple variant were about one and two orders of magnitude below the wild-type enzyme, respectively. We observed a similar trend in peroxidase activity (Table 2.4). These data corresponded well to the proportion of hexacoordinate low-spin heme observed in EPR spectra.

2.3.4 Effect of I'-helix substitution on KatG stability:

As mentioned in *Materials and methods*, substituting the strictly conserved residues in the I'-helix resulted in expression of protein in insoluble inclusion bodies. Soluble protein could be obtained if expression was carried out at lower temperatures. This suggested that these residues might be central to the proper folding and stability of the enzyme. To investigate this further, we evaluated the effect of guanidine hydrochloride (GuHCl) on the secondary structural content of KatG and its variants by far-UV circular dichroism. In addition, the sensitivity of the KatG active site to disruption by GuHCl or temperature variation was monitored by stopped-flow and UV-visible absorption, respectively. All three methods revealed that single substitutions to the I'-helix had minimal influence on KatG stability. Disruption of secondary structure by GuHCl was indistinguishable for wild-type KatG and the single variants (Fig. 2.5). Extrapolated free energies of unfolding and mid-point unfolding concentrations of GuHCl (C_m's) were all similar for wild-type KatG, R691A, E695A, Y697A, and even the double variant L690A/R691A (Table 2.5). At the active site level, these same variants showed only modest increases in the rates of GuHCl-mediated heme loss, and thermally induced heme loss was virtually identical for wild-type KatG, the single variants, and L690A/R691A. Interestingly, in this latter experiment the E695A variant did stand out from the group with a T_m about 6 °C lower than the wild-type

Table 2.5: Parameters GuHCl-mediated unfolding of wtKatG and I'-helix variants.

Protein	Parameter			
	$\Delta G°_{H2O}$ (kJ mol $^{-1}$)	m [a] (kJ mol^{-1} M^{-1})	C_m [b] (M)	k_{obs} [c] (s^{-1})
wt KatG	12.3 ± 0.63	6.86 ± 0.32	1.76 ± 0.03	0.020 ± 0.010
R691A	11.0 ± 0.66	6.28 ± 0.37	1.70 ± 0.04	0.105 ± 0.004
E695A	10.2 ± 0.47	5.78 ± 0.28	1.78 ± 0.03	0.134 ± 0.042
Y697A	11.5 ± 0.58	6.27 ± 0.31	1.72 ± 0.04	0.231 ± 0.010
L690A/R691A	8.93 ± 0.41	5.52 ± 0.21	1.66 ± 0.51	0.356 ± 0.088
E695A/Y697A [d f]	12.8 ± 1.73	7.14 ± 0.78	2.33 ± 0.07	8.58 ± 0.036
E695A/Y697A [e f]	4.99 ± 0.27	4.51 ± 0.30	0.45 ± 0.21	8.58 ± 0.036
L690A/R691A/E695A/Y697A [f]	7.47 ± 0.97	25.8 ± 2.8	0.27 ± 0.02	8.47 ± 0.023
KatG^N	9.96 ± 1.12	51.9 ± 4.8	0.19 ± 0.01	8.77 ± 0.019

[a] m, efficacy of GuHCl in unfolding.

[b] C_m, GuHCl concentration with K=[U]/[N]=1

[c] From single exponential fit of plots of absorbance at $A_{413.9\ nm}$ in the presence of 2M GuHCl.

[d] Obtained from the second of two phase of GuHCl-mediated unfolding.

[e] Obtained from the first of two phase of GuHCl-mediated unfolding.

[f] protein aggregation was observed in presence of <1M GuHCl.

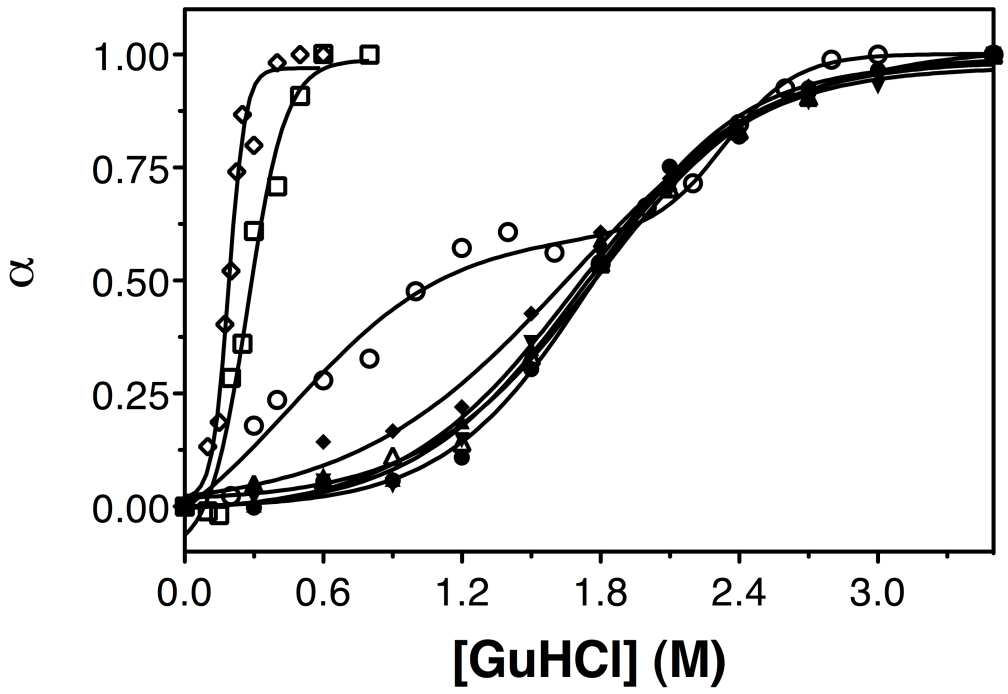

Figure 2.5: GuHCl-mediated unfolding of wtKatG, its I′-helix variants, and KatG^N as monitored by far-UV CD spectroscopy.

Relative changes in ellipticity at 222 nm were monitored for wtKatG (●), R691A (▲), Y697A (▼), L690A/R691A (⬥), E695A (△), E695A/Y697A (○), L690A/R691A/E695A/Y697A (□), and KatG^N (◇). All reactions were carried out using 5 mM phosphate buffer, pH 7.0, at 23 °C. For KatGs indicated by closed symbols, 5 μM protein was used, and for those indicated by open symbols, 10 μM protein was used. The fraction of the unfolded state, α, was calculated according to Eq. (4).

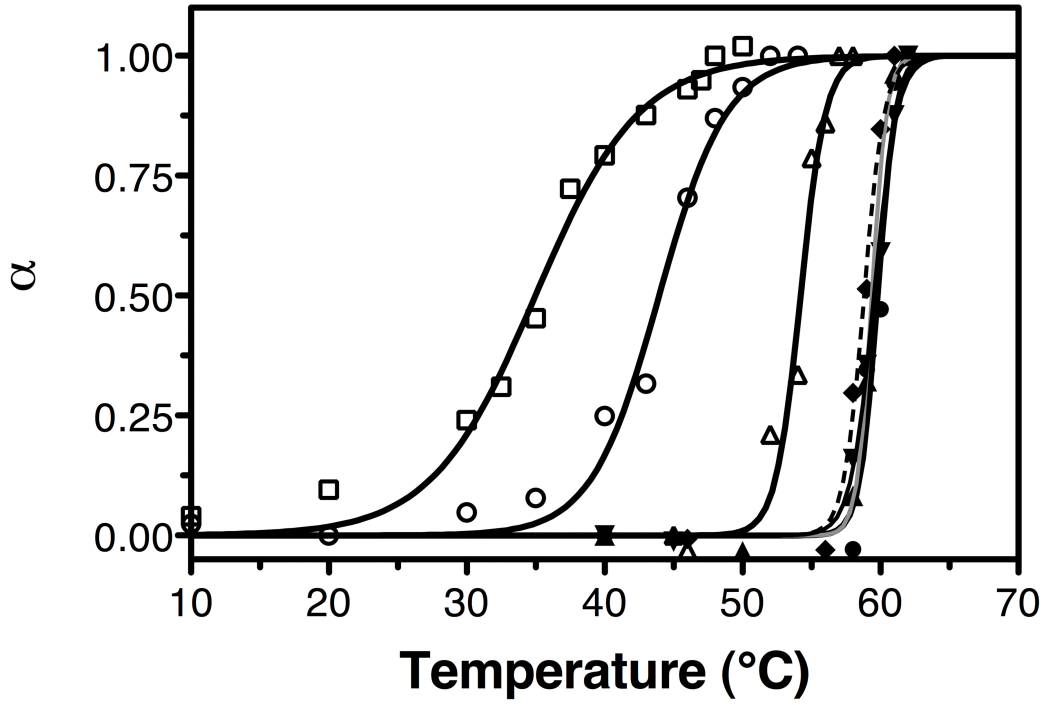

Figure 2.6: Thermal stability of the heme cavity of wtKatG and its I′-helix substitution variants.

The effect of temperature on heme absorption spectra was evaluated for wtKatG (●), R691A (▲), Y697A (▼), L690A/R691A (⬥), E695A (△), E695A/Y697A (○), and L690A/R691A/E695A/Y697A (□). All temperature profiles were carried out using 100 mM phosphate buffer, pH 7.0. Background correction for individual spectra was carried out based on absorbance at 450 nm. The fraction of active site-disrupted KatG, α, was calculated according to Eq. (3).

enzyme (Fig. 2.6).

The E695A/Y697A KatG and quadruple variant were considerably less stable. The secondary structural content of the E695A/Y697A variant showed a two-component response to GuHCl. The T_m corresponding to the temperature dependent loss of heme for this variant was 16 °C lower than the wild-type enzyme, and the rate of heme loss upon reaction with 2M GuHCl was over 400 fold faster than wild-type KatG. The quadruple variants showed an even greater loss of stability. The T_m was 24 °C below wild-type, and the C_m with respect to GuHCl concentration was over seven fold lower. The rate constant for GuHCl mediated unfolding was also over 400-fold faster. Interestingly, these properties bore a striking resemblance to KatG lacking its entire C-terminal domain (i.e., $KatG^N$).

2.3.5 Spectroscopic properties of $KatG^N$ + $KatG^C$ I'-helix substitution variants:

Expressed as a separate protein, the KatG N-terminal domain ($KatG^N$) has neither catalase nor peroxidase activity, and the dominant form of heme is a hexacoordinate low-spin complex [142]. Introducing the separately expressed and isolated C-terminal domain ($KatG^C$) results in restructuring of $KatG^N$ that is evident from a return of high-spin coordination states typical of wild-type enzyme as well as the restoration of catalase and peroxidase activities [144]. Specifically, incubation of $KatG^N$ with equimolar $KatG^C$ at 4 °C results in a blue shift of the Soret band from 415.5 to 410 nm, a decrease in the intensity of the β and α bands at 535 and 560 nm, respectively, and an increase in intensity of charge transfer bands at 505 and 640 nm (Fig. 2.7). By EPR, the rhombic signal (g_x =2.92, g_y =2.28, g_z =1.53) corresponding to hexacoordinate low-spin heme diminishes in intensity along with a pronounced increase in the two rhombic

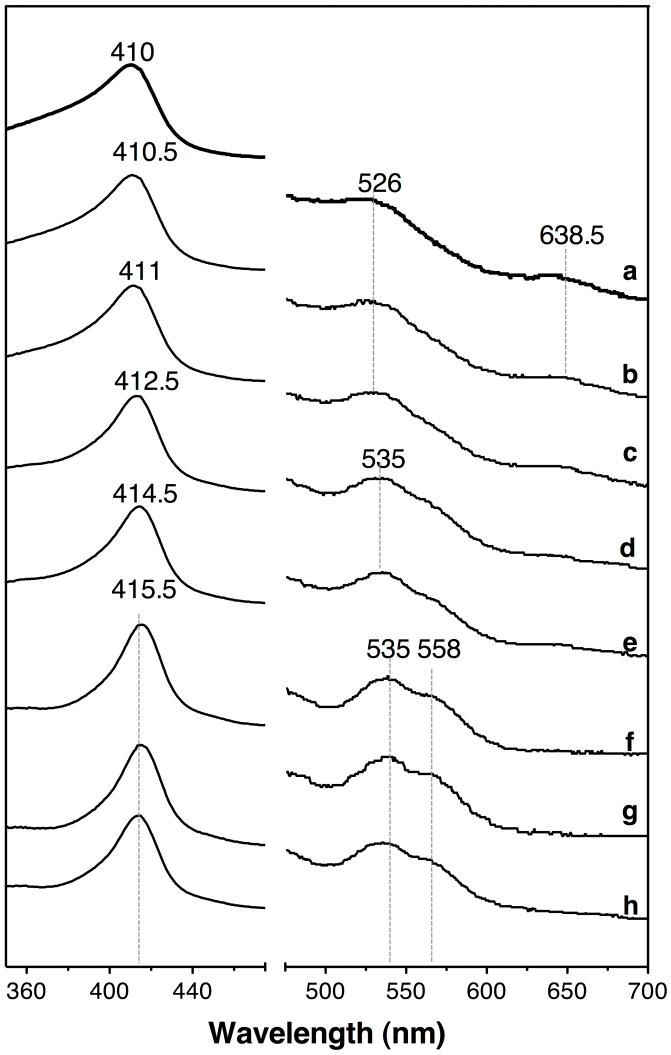

Figure 2.7: UV–visible absorption spectra of KatG^{N} following incubation with KatG^{C} or its I′-helix substitution variants.

Spectra were recorded for the following combinations: KatG^{N} + KatG^{C} (a), KatG^{N} + L690A KatG^{C} (b), KatG^{N} + Y697A KatG^{C} (c), KatG^{N} + R691A KatG^{C} (d), KatG^{N} + E695A KatG^{C} (e), KatG^{N} + L690A/R691A KatG^{C} (f), KatG^{N} + E695A/Y697A KatG^{C} (g) and KatG^{N} alone (h). All reactions contained 10 μM KatG^{N} and, if present, equimolar KatG^{C} (or variant thereof).

signals mentioned before corresponding to hexacoordinate and pentacoordinate high-spin heme, respectively (Fig. 2.8). To varying degrees single substitutions to the I'-helix of $KatG^C$ resulted in a greater residual proportion of hexacoordinate low-spin states than observed with unmodified $KatG^C$. The L690A variant most closely resembled unmodified $KatG^C$, producing a shift in Soret max to 410.5 nm, followed by Y697A (411 nm), R691A (412.5 nm), and E695A (414.5 nm) with the latter showing little ability to alter the coordination state of the heme in the $KatG^N$ active site (Fig. 2.7). A nearly identical trend was observed by EPR spectroscopy (Fig. 2.8). Individual EPR signals were integrated and spectra simulated to quantify the relative proportions of high-spin and low-spin species as described previously (Table 2.6). Of the single variants, E695A $KatG^C$ had the most diminished capacity to induce a return of high spin heme species in $KatG^N$, with over 50% of the $KatG^N$ heme remaining in its low-spin form. R691A and Y697 $KatG^C$ left 35 – 40% $KatG^N$ heme in its low-spin state. Meanwhile, L690A $KatG^C$ showed a capacity only slightly below unmodified $KatG^C$ to induce a return of high spin heme species in $KatG^N$. As evaluated by either UV- vis or EPR, $KatG^C$ double variants L690A/R691A and especially E695A/Y697A lost almost all ability to alter the $KatG^N$ heme coordination state.

2.3.6 Kinetic study of $KatG^N$ + $KatG^C$ I'-helix substitution variants:

It has been previously shown that incubation of $KatG^N$ with $KatG^C$ not only produces spectral shifts due to the change in heme environment, but also the return of both catalase and peroxidase activities [144]. Steady-state kinetic parameters for recovered catalase (Table 2.7) and peroxidase (Table 2.8) activities follow very closely the trends observed in spectroscopic experiments. Any substitution to the I'-helix diminished the ability of $KatG^C$ to recover catalase and peroxidase activity. The effect was most pronounced with the E695A substitution and

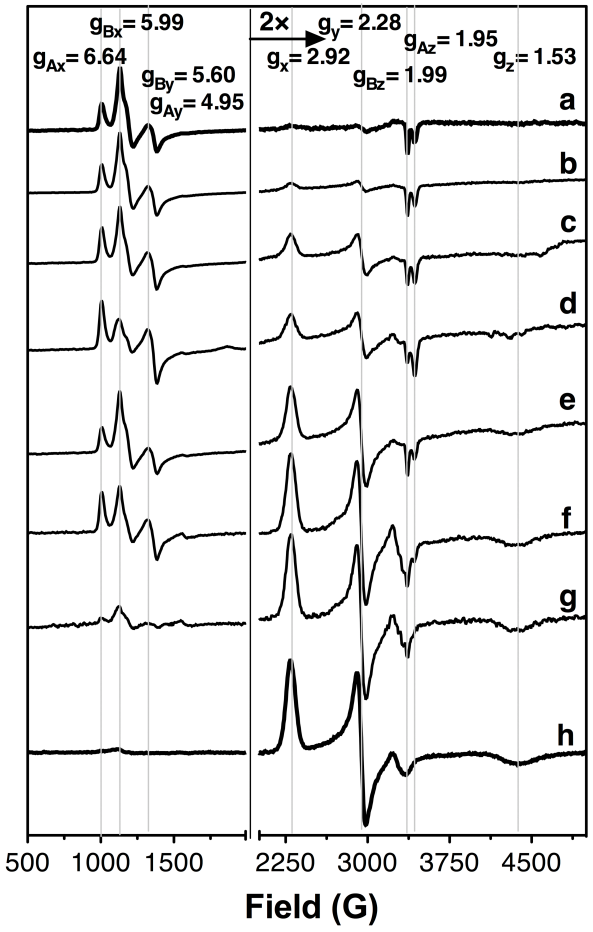

Figure 2.8: EPR spectra of KatG^N following incubation with KatG^C or its I′-helix substitution variants.

Spectra were recorded for the following combinations: KatG^N + KatG^C (a), KatG^N + L690A KatG^C (b), KatG^N + Y697A KatG^C (c), KatG^N + R691A KatG^C (d), KatG^N + E695AKatG^C (e), KatG^N + L690A/R691AKatG^C (f), KatG^N + E695A/Y697A KatG^C (g) and KatG^N alone (h). The g-values corresponding to RHS 1 (g_{Ax}, g_{Ay}, and g_{Az}) and RHS 2 (g_{Bx}, g_{By}, and g_{Bz}) are shown as those of the hexacoordinate low spin complex (g_x, g_y, and g_z).

Table 2.6: Ratios of EPR signals observed following $KatG^N$ incubation with $KatG^C$ or its I′helix substitution variants

Protein	**% contribution**		
	HS[a] : LS[b]	RHS 1[c]: RHS 2[d]	RHS 1: RHS 2 : LS
$KatG^N$+$KatG^C$	94 : 6	63 : 37	59 : 35 : 6
$KatG^N$+L690A $KatG^C$	88 : 12	60 : 40	53 : 35 : 12
$KatG^N$+R691A $KatG^C$	62 : 38	82 : 18	51 : 11 : 38
$KatG^N$+E695A $KatG^C$	45 : 55	60 : 40	27 : 18 : 55
$KatG^N$+Y697A $KatG^C$	63 : 37	71 : 29	44 : 19 : 37
$KatG^N$+L690A/R691A$KatG^C$	19 : 81	75 : 25	14 : 5 : 81
$KatG^N$+E695A/Y697A$KatG^C$	3 : 97	44 : 56	1 : 2 : 97
$KatG^N$	0 : 100	0 : 0	0 : 0 : 100

[a] : High Spin; HS = RHS 1+RHS 2

[b] : Low Spin (g_x =2.92 , g_y =2.28 , g_z =1.53)

[c] : Rhombic high-spin species 1 (g_x=6.64, g_y=4.95 and g_z=1.95)

[d] : Rhombic high-spin species 2 (g_x=5.99, g_y=5.60 and g_z=1.99)

progressively less for R690A, Y697A, and least for L690A. Likewise, multiple substitutions to I'-helix residues completely abrogated the ability of $KatG^C$ to restore catalytic function to the N-terminal domain.

I'-helix substitutions also diminished the rate of $KatG^N$ active site restructuring by $KatG^C$ (Fig. 2.9, Table 2.7). Here the same trend was observed as in the spectroscopic and steady-state activity experiments. The most rapid rate of $KatG^N$ activity recovery, of course, was facilitated by the unmodified $KatG^C$. Any substitution to the I'-helix diminished the rate with the E695A producing the largest effect followed by R691A, Y697A, and finally L690A. As described above, two or more substitutions to the I'-helix produced $KatG^C$ with no capacity to reactivate $KatG^N$.

2.4 Discussion:

All catalase-peroxidases have a two-domain structure which appears to have arisen from the gene duplication and fusion of a predecessor peroxidase [118]. Since that event, the N-terminal domain has either gained or retained the capacity for heme-dependent reduction *and* oxidation of H_2O_2 as well as a classical, albeit limited, peroxidatic activity. In contrast, the C-terminal domain has lost the ability to bind heme or catalyze any reaction. Nevertheless, the C-terminal domain is an integral component of catalase-peroxidase structure and catalysis [142, 144, 145], but its precise roles in KatG function are still unknown.

One hypothesis has been that the C-terminal domain serves as a platform to support the folding of the N-terminal domain [143] that in the absence of the C-terminal domain, the N-

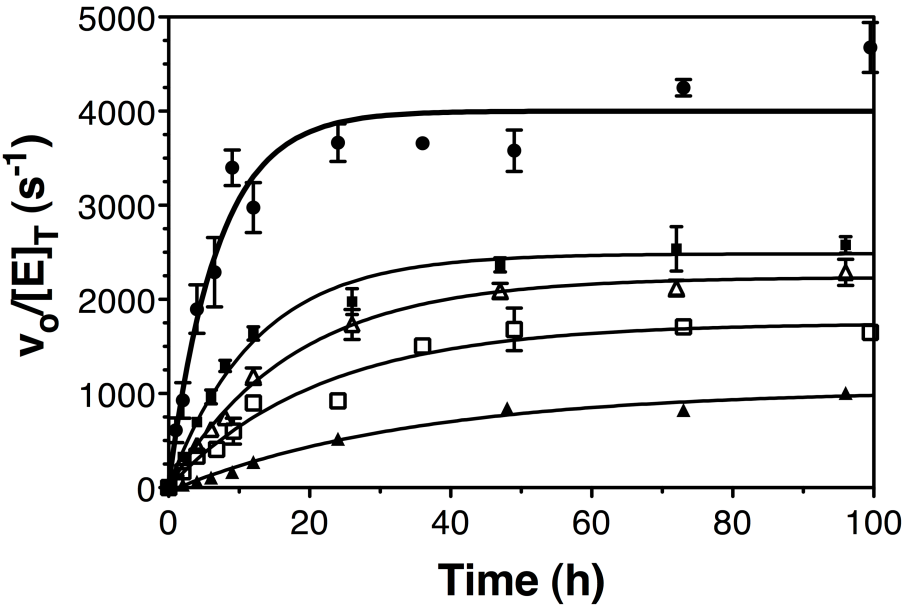

Figure 2.9: Time course for recovery of KatG^N catalase activity upon addition of equimolar KatG^c or one of its I′helix substitution variants.

Activity measurements were made for the following combinations: KatG^N + KatG^C (●), KatG^N + L690A KatG^C (■), KatG^N + Y697A KatG^C (Δ), KatG^N + R691A KatG^C (□), and KatG^N + E695A KatG^C (▲). Incubations were carried out at 4 °C in 100 mM phosphate buffer, pH 7.0. Assays of the activity contained 50 nM KatG^N and KatG^C (or variant thereof), 10 mM H_2O_2, and 100 mM phosphate buffer, pH 7.0. Assays were all performed at 23 °C.

Table 2.7: $KatG^N$ reactivation k_{obs} and apparent catalase parameters for reactivated enzyme.

Protein	**Catalase cycle parameter**[a]			**Reactivation**[b]
	k_{cat} (s^{-1})	K_M (mM)	k_{cat}/K_M (10^6 M^{-1} s^{-1})	k_{obs} (10^{-5} s^{-1})
$KatG^N$+$KatG^C$	4000 ± 350	2.4 ± 0.6	1.7	3.83 ± 0.56
$KatG^N$+L690A $KatG^C$	3500 ± 340	4.0 ± 0.9	0.9	2.25 ± 0.18
$KatG^N$+R691A $KatG^C$	2200 ± 220	3.6 ± 0.3	0.6	1.36 ± 0.08
$KatG^N$+E695A $KatG^C$	1050 ± 170	6.0 ± 1.9	0.2	0.81 ± 0.11
$KatG^N$+Y697A $KatG^C$	2700 ± 180	3.3 ± 0.5	0.8	1.53 ± 0.26
$KatG^N$+L690A/R691A $KatG^C$	ND[c]	ND	ND	ND
$KatG^N$+E695A/Y697A $KatG^C$	ND	ND	ND	ND

[a] All assays included 50 nM enzyme in 100 mM phosphate buffer, pH 7.0, at 23 °C.

[b] Incubation conditions for reactivation: 100 mM phosphate buffer, pH 7.0, at 4 °C.

[c] Not determined.

Table 2.8: Apparent Peroxidase parameters for reactivated $KatG^N$ by $KatG^C$ or its I' helix variants.[a]

Protein	**Peroxide-dependent parameters**			
	k_{cat} (s^{-1})	K_M (mM H_2O_2)	k_{cat}/K_M (M^{-1} s^{-1})	Ki (mM H_2O_2)
$KatG^N$+$KatG^C$	48.7 ± 1.0	0.068 ± 0.007	7.20×10^5	-
$KatG^N$+ L690A $KatG^C$	16.0 ± 0.4	0.075 ± 0.008	2.13×10^5	-
$KatG^N$+ R690A $KatG^C$	22.8 ± 0.5	0.077 ± 0.007	2.98×10^5	-
$KatG^N$+ E695A $KatG^C$	6.10 ± 0.1	0.039 ± 0.003	1.54×10^5	-
$KatG^N$+ Y697A $KatG^C$	10.8 ± 1.4	0.027 ± 0.020	4.07×10^5	-
$KatG^N$+L690A/R691A$KatG^C$	ND	ND	ND	-
$KatG^N$+E695A/Y697A$KatG^C$	ND	ND	ND	-
Protein	**ABTS-dependent parameters**			
	k_{cat} (s^{-1})	K_M(mM ABTS)	k_{cat}/K_M (M^{-1} s^{-1})	Ki (mM ABTS)
$KatG^N$+$KatG^C$	56.2 ± 2.9	0.423 ± 0.061	1.32×10^5	9.81 ± 1.4
$KatG^N$+ L690A $KatG^C$	14.0 ± 0.8	0.116 ± 0.024	1.20×10^5	13.5 ± 3.2
$KatG^N$+ R690A $KatG^C$	22.0 ± 1.7	0.086 ± 0.021	2.56×10^5	7.67 ± 1.9
$KatG^N$+ E695A $KatG^C$	5.60 ± 0.4	0.042 ± 0.010	1.33×10^5	7.30 ± 1.5
$KatG^N$+ Y697A $KatG^C$	14.0 ± 0.6	0.095 ± 0.014	1.47×10^5	9.72 ± 1.5
$KatG^N$+L690A/R691A$KatG^C$	ND	ND	ND	-
$KatG^N$+E695A/Y697A$KatG^C$	ND	ND	ND	-

[a] Assay included 50 nM enzyme in 50 mM acetate buffer, pH 5.0 at 23 °C.

terminal domain alone has no apparent activity, and its heme is in a hexacoordinate low-spin ferric state [142]. This is remedied by the reintroduction of the separately expressed and isolated C-terminal domain ($KatG^C$) which restores a correct coordination state as well as both catalase and peroxidase activities [144].

Visual inspection of known KatG structures reveals substantial intrasubunit as well as intersubunit interactions between N- and C-terminal domains. One prominent example is the I'-helix which appears at the interface between the two domains and contacts several elements of the N-terminal domain. As such, the I'-helix may serve as a central component of a hypothetical folding platform provided by the C-terminal domain [119, 143].

One aspect of our approach to test this hypothesis was to evaluate the effect of substitution to the I'-helix on the ability of $KatG^C$ to reactivate $KatG^N$. Indeed, our data indicate that even single substitutions to the I'-helix substantially limit the ability of $KatG^C$ in this respect. All of the single variants showed a decrease in the rate and extent of $KatG^N$ reactivation. With two substitutions to the I'-helix, $KatG^C$ become completely incapable of directing the restructuring of $KatG^N$ reactivation. Clearly, the I'-helix is a critical component in this process.

Because preparation of $KatG^N$ involves denatured purification, refolding, and reconstitution, it is reasonable to argue that the reactivation of $KatG^N$ by $KatG^C$ may not adequately reveal the extent to which the C-terminal domain directs folding events and structural adjustments to the N-terminal domain during expression in vivo. In light of this, it is compelling that we observed similar trends and phenomena for I′-helix substitutions to intact KatG. All of

the intact KatG variants showed a greater tendency toward expression in inclusion bodies. In addition, the double and quadruple variants showed a substantially increased propensity to form the hexacoordinate low-spin state as well as clear compromises to active site and overall protein structural stability. Indeed, the quadruple variant showed properties nearly identical to $KatG^N$ in all respects even though it retained what appeared to be a correctly folded C-terminal domain. We hasten to add that the effects of I′-helix substitutions were more subtle for the intact protein than $KatG^C$. Where most single substitutions produced notable defects in the restructuring activity of $KatG^C$, those same substitutions to intact KatG showed only modest influences on stability, coordination state, and catalytic function.

There are extensive hydrogen-bonded networks between the I′-helix of the C-terminal domain and its intersubunit N-terminal domain partner [119-122] (Fig. 2.10A). In particular, E695 (Fig. 2.10B) forms an H-bond with conserved W159 at the N-terminal end of the d-helix. Further, in conjunction with the R126 side chain, E695 typically coordinates two water molecules. Interestingly, this same R126 guanidium group, a strictly conserved residue of the BC interhelical connecting loop, makes several additional polar contacts including the carbonyl oxygen of residue 188, and through a well-ordered water molecule, the invariant D187 carboxylate, and the carbonyl oxygens of residues 122 and 123. The former pair is located on the DE helical connecting loop, and the latter pair is found on the BC loop. Interestingly, in Class II peroxidases (e.g. manganese peroxidase), which depend on Ca^{2+} to maintain the heme coordination environment that supports activity, the relevant calcium-binding site is established

in part by this same portion of the BC loop [168, 169]. More broadly, this network connects the I′-helix with several core components of the peroxidase fold of the N-terminal domain.

Interestingly, E695 also appears to participate in another network that also includes R691 and R144 (Fig. 2.10B). Though less well defined, these strictly conserved arginines form additional hydrogen bonds with the backbone carbonyl of Q293 (Met in *M. tuberculosis* KatG), a residue from large loop 2 (LL2). In addition, the side chain of amino acid 293 forms tight interactions with hydrophobic residues from the I′-helix. Notably, our EPR spectra of R691A showed a greater contribution from the RHS 1 component, the pentacoordinate high-spin species, than either wild-type or the other single variants. In an interesting corroboration of those results, we have observed that KatG lacking LL2 (or Q293-containing portions thereof) shows nearly identical spectroscopic signatures and catalytic properties [130].

Unlike E695 and R691, L690 and Y697 side chains are located such that they make contact with both inter- and intrasubunit N-terminal domain partners (Fig. 2.10 A and C). The lesser impact of L690 and Y697 may owe to the fact that both residues are in contact with the N-terminal end of the N-terminal domain rather than its core structures like the BC loop, C helix or LL2, all of which appear to be crucial for protein active site folding and catalytic ability.

In summary, at first glance the KatG C-terminal domain has all the appearances of a vestigial structure. It bears the general structure of a peroxidase and even the correct helical framework to support an active site, but this domain shows no ability to bind heme or catalyze any reaction. The closest relatives of KatG, cytochrome *c* peroxidase and ascorbate peroxidase, have no C-terminal domain. Indeed, it is proposed that the single domain peroxidases were

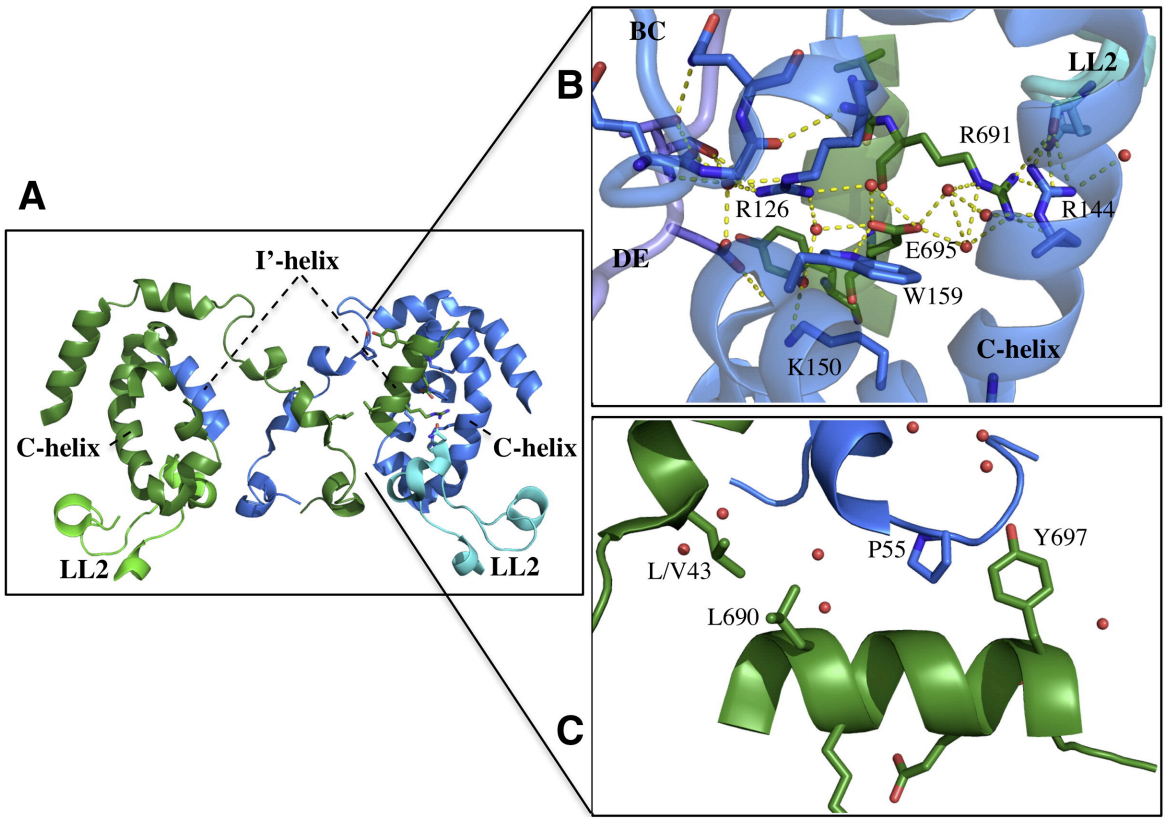

Figure 2.10: Interfaces between the KatG N-terminal domain and I′-helix from the C-terminal domain.

The secondary structural context of the I′-helix from each KatG subunit is shown in panel A. A magnified view of the interactions of E695 and R691 is shown in panel B, and that corresponding to L690 and Y697 is shown in panel C. Coordinates are from the structure of *Burkholderia pseudomallei* KatG (PDB:1MWV). Numbering reflects *Escherichia coli* KatG sequence. Secondary structures in green are from subunit A and those in blue are from subunit B. Dotted lines indicate inferred polar contacts. Red spheres represent water molecules.

obtained from the deletion of one domain from a two-domain predecessor [92]. Nevertheless, the C-terminal domain is a universal component of KatGs, and without it, the enzyme does not function. Such a large structure could conceivably have several roles in KatG function, but one proposal has been that it serves as a folding platform for the active site-bearing N-terminal domain [143]. We have capitalized on the unique ability of $KatG^{C}$ to restructure and reactivate an otherwise inactive $KatG^{N}$ to show that the C-terminal domain's I′-helix may be a central component of a platform to facilitate folding events and/or conformational adjustments in the N-terminal domain. Though less dramatic, our results with intact KatG corroborate those obtained with the separately prepared domains. In particular, substituting four strongly conserved residues in I′-helix resulted in a protein whose properties were nearly identical to $KatG^{N}$ even though it retained what appeared to be a correctly folded C-terminal domain.

CHAPTER THREE

FACILITATING KATG INTERDOMAIN COMMUNICATION: CONNECTING THE REMOTE I'-HELIX TO ACTIVE SITE CONFORMATION, STABILITY, AND CATALYTIC FUNCTION

3.1 Introduction:

Two of the most common enzymes in nature for disposing of H_2O_2 are heme-dependent peroxidases and catalases. A unique family of enzymes that show both catalase and peroxidase activities (KatGs) are found among archaea, eubacteria, fungi and protists [93, 170, 171]. The typical catalase and peroxidase cycles both start with the heterolytic reduction of H_2O_2 along with the oxidation of the ferric heme to a ferryl porphyrin/protein radical intermediate (compound I). In the typical catalase cycle, compound I is then reduced back to resting enzyme by a second equivalent of H_2O_2, generating O_2 and H_2O. Conversely, the peroxidase returns to the ferric state by two sequential one-electron steps using an exogenous reducing substrate. The first reduction produces one equivalent of substrate radical and either a ferryl or a ferric-hydroxy/protein radical intermediate (compound II), and the second reductive step produces the resting enzyme and a second equivalent of substrate radical.

Catalase-peroxidases belong to class I of a superfamily formerly designated as the fungal, plant and bacterial peroxidases [118]. Driven in part by the dramatic increase in sequence data for all types of peroxidases, the nomenclature has recently been adjusted to designate this

superfamily as the peroxidase-catalases [21]. KatGs are observed either as homodimers or homotetramers, where each subunit is composed of two homologous domains. Neither domain bears any resemblance to monofunctional catalases, but both have the topological structure of monofunctional peroxidases. Only the N-terminal domain retains an active site, and it is superimposable with those of typical peroxidases [119, 120, 122, 146]. The C-terminal domain is ≥ 30 Å from the active site. It is conserved across all catalase-peroxidases, and its topological similarity to peroxidases suggests that it originated from a gene-duplication and fusion event [118, 128, 141]. However, the roles of this second, apparently "inactive", domain in catalysis are not immediately obvious. It bears a striking resemblance to monofunctional peroxidases, but it neither binds heme nor catalyzes any discernable reaction [119, 120, 122, 143, 146]. It has been suggested that the C-terminal domain might serve as a platform to direct proper folding of the N-terminal domain and facilitate dimerization [143, 144]. Our own results support this assertion and further suggest that the I'-helix is a necessary structure for directing structural adjustments in the adjacent N-terminal domain active site (See Chapter 2) [172]. We noted that E695 was particularly important as substitution of this strictly conserved residue was destructive to KatG active site integrity and profoundly disrupted the ability of $KatG^C$ to induce structural adjustment in its $KatG^N$ partner.

Visual inspection of the crystal structures of KatG indicates that E695 forms an H-bond with conserved W159 found at the N-terminal end of the D-helix. It also, through two well-ordered water molecules, forms substantial contacts with R126, a residue found on the BC helical connecting loop [119, 120, 122, 146]. These are core structures of the peroxidase fold, and may account for the substantial effect of E695 substitution on KatG active site, conformation,

stability and function. Therefore, E695 located 25 Å from the active site may through these interactions modulate the N-terminal domain active site conformation and functionality.

To address these interactions and their impacts on the KatG active site. We produced single and double alanine substitution variants of intact KatG, $KatG^N$ and $KatG^C$. These were expressed, isolated and characterized. Here, we report the effect of these substitutions not only on active site structure, stability and bifunctionality in intact KatG, but also on $KatG^N$ reactivation by $KatG^C$. The spectroscopic and kinetic results demonstrate that strictly conserved R126 and W159 are critical for KatG active site structure, stability and catalytic function. Through its interaction with these residues, E695 of the I'-helix modulates the active site conformation and function.

3.2 Materials and Methods:

3.2.1 Materials:

Hydrogen peroxide (30%), imidazole, hemin, ampicillin, chloramphenicol, sodium dithionite, phenylmethylsulfonyl fluoride (PMSF), 2,2′-azino-bis (3-ethylbenzthiazoline-6-sulfonate) (ABTS), and guanidine hydrochloride (GuHCl) were purchased from Sigma (St. Louis, MO). Isopropyl-β-d-thiogalactopyranoside (IPTG), urea, mono- and dibasic sodium phosphate, acetic acid, and sodium acetate were obtained from Fisher (Pittsburgh, PA). Bugbuster and benzonase were purchased from Novagen (Madison, WI). All restriction enzymes were purchased from New England Biolabs (Beverly, MA). All oligonucleotide primers were purchased from Invitrogen (Carlsbad, CA). All *E. coli* strains (BL-21-Gold [DE3] pLysS and XL-1 Blue), *Pfu* polymerase, and T4 DNA ligase were obtained from Agilent (La Jolla, CA).

Nickel-nitrilotriacetic acid (Ni-NTA) resin was purchased from Qiagen (Valencia, CA). Desalting 10DG chromatography columns were purchased from Bio-Rad. All buffers and media were prepared using water purified through a Barnstead EasyPure II system (18.2 MΩ/cm resistivity).

3.2.2 Cloning:

All plasmids were prepared using mutagenic coding and non-coding primers (Table 3.1) according to the Round-the-Horn procedure [152]. Amplification products were subjected to blunt-end ligation with T4 DNA ligase and used to transform *E. coli* (XL-1 Blue) by heat shock according to manufacturer instructions, and transformants were selected on the basis of ampicillin resistance. Plasmids from candidate colonies were isolated and evaluated by diagnostic restriction digest (Table 3.1) and DNA sequence analysis (Davis Sequencing, Davis, CA). Plasmids verified to carry the correct mutations were used to transform *E. coli* (BL-21-Gold [DE3] pLysS).

3.2.3 Expression and Purification:

All expression was carried out in *E. coli* (BL-21-Gold [DE3] pLysS) using liquid Luria–Bertani broth supplemented with ampicillin and chloramphenicol with constant agitation. Wild-type KatG was over-expressed in a soluble form as previously described [151]. However, variants with substitutions to E695 and W159 were expressed in inclusion bodies at 37 °C. In order to express soluble forms, we reduced the temperature for expression to 18 °C. The $KatG^C$ was over-expressed in a soluble form with a six His-tag at 37 °C as previously described [144]. In all other respects, expression and purification was carried out as previous described (Chapter 2). Concentrations of purified enzyme were estimated according to the method of Gill and von

Table 3.1: Primer sets for site-directed mutagenesis.

Protein:	Primer Sequences:	Restriction enzymes
E695A	5'-Phos-GCAGTTTACGCCAGTAGCGATGCCCACG-3' 5'-Phos-AGCCACCGCACGCAGGACGGAGTTA-3'	*Pst I*
E695Q	5'-Phos-GCAAGTATACGCCAGTAGCGATGCCACG-3' 5'-Phos-GCCACCGCACGCAGGACGGAGTTAG-3'	*Acc I*
R126A	5'-Phos-CTTTTGCACCGCTGAACTCCTGGCCG-3' 5'-Phos-CTTGCTGACCACGACCCGCGCC-3'	*Hind III*
W159A	5'-Phos-GTCAGAAAATCTCCGCGGCCGACCTGTT-3' 5'-Phos-CATATTTCTGTTTGATTGGCCACAACAGGCGACGC-3'	*Eag I*

Hippel [154]. $KatG^N$, R126A$KatG^N$ and W159A$KatG^N$ were expressed in inclusion bodies and were purified under denaturing conditions as described in Chapter 2.

3.2.4 Enzyme reconstitution:

Enzyme reconstitution followed the procedures described in Chapter 2. In order to minimize effects of free or adventitiously bound hemin to spectral or kinetic measurement after domain incubation, reconstitution of $KatG^N$ was carried out by adding 0.75 equivalents of hemin to enzyme. These solutions were allowed to incubate for at least 24 h at 4 °C. These solutions were then centrifuged to remove insoluble unincorporated heme and other debris. Molar absorptivities were as follows: W159A $KatG^N$ and $KatG^N$ (ε_{416} = 98 mM^{-1} cm^{-1}); R126A $KatG^N$ (ε_{416} = 113 mM^{-1} cm^{-1}) $KatG^C$, E695Q $KatG^C$, and E695A $KatG^C$ (ε_{280} = 34 mM^{-1} cm^{-1}); Solutions containing 1:1 ratios of $KatG^N$ and $KatG^C$ or one of its variants were incubated for times ranging from 0 to 96 h in the presence of 50 mM phosphate buffer, pH 7.0, 50 mM NaCl at 4 °C. Optimal results were obtained with freshly purified and reconstituted $KatG^N$ and freshly purified $KatG^C$.

3.2.5 Absorption spectra:

The final concentration of incorporated hemin was determined by the pyridine hemichrome method of Falk [155] and used to calculate molar absorptivities of the heme absorption spectra of each protein. Spectra for the ferrous states of these proteins were obtained by adding a small amount (< 10 mg) solid dithionite to the ferric form of each. All spectra were obtained at room temperature on a Shimadzu UV-1601 spectrophotometer (Columbia, MD) with a cell path length of 1.0 cm.

3.2.6 Catalase and peroxidase activity assays:

Peroxidase activity was evaluated by monitoring the production of the ABTS radical over time at 417 nm ($34.7\ mM^{-1}\ cm^{-1}$) [156]. All assays were carried out at room temperature in 50 mM acetate buffer, pH 5.0. Catalase activity was evaluated by monitoring the decrease in H_2O_2 concentration with time at 240 nm ($39.4\ M^{-1}\ cm^{-1}$) [157]. All assays were carried out at room temperature in 100 mM phosphate buffer, pH 7.0. Initial velocities ($v_o/[E]_T$) were fit to a Michaelis–Menten equation (Eq. (1)) by non-linear regression analysis to determine apparent kinetic parameters k_{cat}, K_M, and k_{cat}/K_M.

$$v_o/[E]_T = \frac{k_{cat}[S]}{K_M + [S]} \qquad (1)$$

Here, $[E]_T$ is determined on the basis of the heme content of the protein(s) present. In all instances reported here, k_{cat} is the asymptotic maximum catalytic output, the apparent K_M simply corresponds to the concentration of substrate necessary to produce $v_o/[E]_T$ equal to ½ k_{cat}, and k_{cat}/K_M, the apparent second-order rate constant, represents the efficiency with which the substrate is processed and corresponds to the slope of the tangent line to rates obtained at low [S] (i.e., $<K_M$). When evaluating peroxidase activity as a function of H_2O_2 concentration, H_2O_2-dependent inhibition was frequently observed. In order to account for the inhibitory effect and make accurate determinations of the apparent parameters k_{cat}, K_M, and k_{cat}/K_M, the data were fit to Eq. (2) derived from a general model for substrate-dependent inhibition [173], where K_I is an apparent dissociation constant corresponding to inhibition due to the substrate.

$$v_o/[E]_T = \frac{k_{cat}[S]}{K_M + [S] + [S]^2/K_I} \qquad (2)$$

3.2.7 Circular Dichroism Spectropolarimetry:

Far-UV (190–300 nm) circular dichroism (CD) spectra were recorded using a Jasco J-810 spectropolarimeter (Tokyo, Japan). To minimize buffer interference at wavelengths below 200 nm, all spectra were recorded using 5 μM enzyme in the presence of 5 mM phosphate buffer, pH 7.0, and Suprasil quartz cells (0.1 mm path length). All spectra were recorded at 23 °C.

3.2.8 Magnetic Circular Dichroism:

All spectra of intact wild-type KatG and its variants were obtained using 15 μM enzyme. Spectra for $KatG^N$ alone or incubated with $KatG^C$ or one of its variants were obtained using 10 μM $KatG^N$. All concentrations were determined on the basis of heme content (see above). Spectra (700–350 nm) were recorded in presence of 50 mM phosphate buffer, pH 7.0 and 50 mM NaCl at 23 °C on a Jasco J-810 spectropolarimeter equipped with a magnetic cell holder (1.4 T) (Tokyo, Japan). Baseline subtraction and spectral analysis were carried out using Jasco J-720 software. The ferrous states of all heme-containing variants/domain combinations were prepared by adding a small amount (< 10 mg) of sodium dithionite to the ferric state.

3.2.9 Electron Paramagnetic Resonance:

Spectra were recorded using a Bruker EMX instrument equipped with an Oxford ESR 900 cryostat and ITC temperature controller. Additional sample concentration was performed using Amicon Ultra-4 centrifugal devices. The settings for the spectrometer were as follows: temperature, 10 K; microwave frequency, 9.38 GHz; microwave power, 0.1 mW; modulation amplitude, 10 G; modulation frequency, 100 kHz; time constant, 655.36 ms; conversion time, 655.36 ms; and receiver gain, 1.0×10^5. Spin quantification was carried out using the

Biomolecular EPR Spectroscopy Software package available online [159, 160].

3.2.10 Evaluation of protein stability:

The effect of GuHCl on the stability of wtKatG and its intersubunit interface variants was evaluated by two methods similar as previous described in Chapter 2 except unfolding study by CD spectroscopy was carried out using 5 μM KatG (or variants). Thermal denaturation of KatG at the active site level was monitored by visible absorption due to the heme prosthetic group as described in Chapter 2. Due to protein aggregation at high temperature, all spectra were background corrected based on their absorbance at 450 nm. Calculation of thermodynamic parameters was carried out according to equations 3-7 as described in Chapter 2.

3.3 Results:

3.3.1 Mutagenesis, expression and purification of KatG and its intersubunit variants:

As confirmed by DNA sequence analysis, we successfully produced constructs for expression of alanine substitutions involving three strictly conserved residues along the intersubunit interface: R126, W159 and E695. As described in *Materials and methods*, all the single substitution variants, as well as the double variants R126A/E695A and W159A/E695A, were successfully expressed and isolated. There was no observable change to secondary structural content as determined on the basis of the circular dichroism spectra of the variants when compared to the wild-type enzyme (Fig. 3.1).

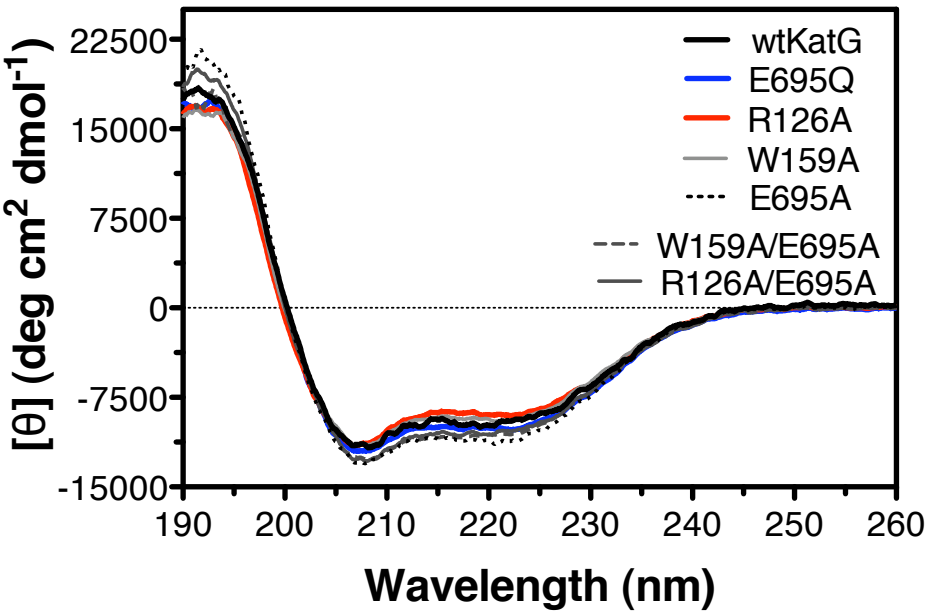

Figure 3.1: Far-UV circular dichroism of wtKatG, and its E695, R126 and W159 substitution variants.

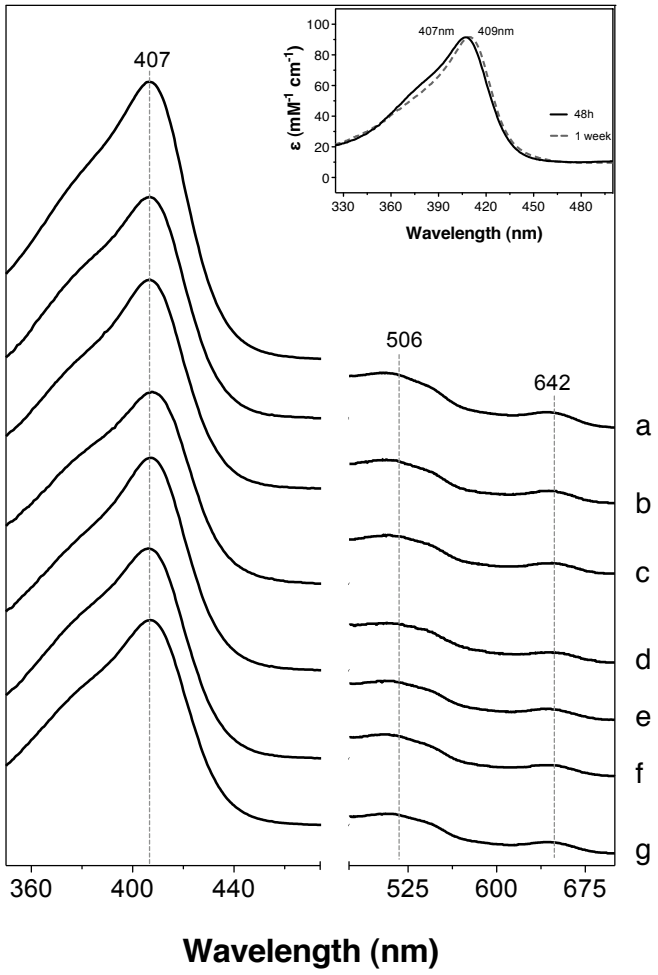

Figure 3.2: UV-visible absorption spectra of ferric wtKatG and its E695, R126 and W159 substitution variants.

All spectra were recorded for the proteins wtKatG (a), E695Q (b), E695A (c), R126A (d), R126A/E695A (e), W159A (f), W159A/E695A (g) in their native ferric state in 100 mM phosphate buffer, pH 7.0, in a 1.0 cm quartz cell at 23 °C. The inset shows a comparison of spectra of R126A/E695A taken after 48 h (solid line) and taken after 1 week (dashed line) reconstituted by hemin.

3.3.2 Spectroscopic properties of R126A, W159A and E695Q:

UV-visible absorption spectra for all the single and double substitution variants were nearly identical to the wild-type enzyme with Soret band maxima between 407 and 407.5 nm and charge transfer transitions around 506 and 640 nm, indicating the active site was dominated by high-spin ferric heme species (Fig. 3.2). With the exception of the R126A/E695A variants, all spectra recorded following storage for one week at 4 °C were unchanged. For R126A/E695A there was a red shift in the Soret band to 409 nm along with increased contributions from the β and α bands at 538 nm and 558 nm, respectively, and diminished intensity of the charge transfer transitions. These features are consistent with increased contribution from hexacoordinate low-spin heme (Fig. 3.2-inset).

In order to more effectively differentiate the high- and low-spin contributions of these variants, magnetic circular dichroism (MCD) spectra were recorded and analyzed. The distinction between the high- and low-spin states is particularly stark in the ferrous rather than ferric oxidation state (as described in Chapter 2). The dominant feature in the ferrous MCD spectra for all the substitution variants was the B-term near 440 nm, similar to the wild-type enzyme. Only the R126A/E695A double variant showed a more intense A-term centered near 560 nm along with a diminished B-term at 440 nm. These data are consistent with a greater contribution from hexacoordinate low-spin heme as observed in UV-vis spectra (Fig. 3.3).

Electron paramagnetic resonance (EPR) spectroscopy was used to further evaluate the influence of substitutions on heme iron environment in the native ferric state (Fig. 3.4). All the substitution variants showed EPR spectra similar to the wild-type, especially in that high-spin

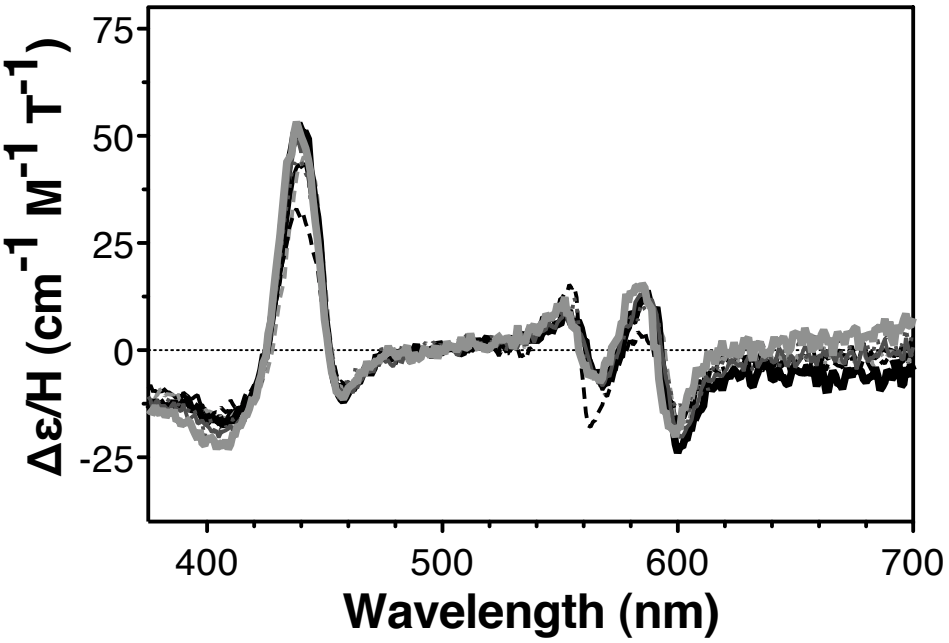

Figure 3.3: MCD spectra of ferrous wtKatG and its E695, R126 and W159 substitution variants.

Spectra were recorded for 15 μM wtKatG (bold line black), W159A (solid line black), E695A (bold line grey), E695Q (solid line grey), W159A/E695A (dotted line), R126A/E695A (dashed line) in presence of 50 mM phosphate 50 mM NaCl pH 7.0 using a 5.0 quartz cell in a 1.4 T magnetic cell holder.

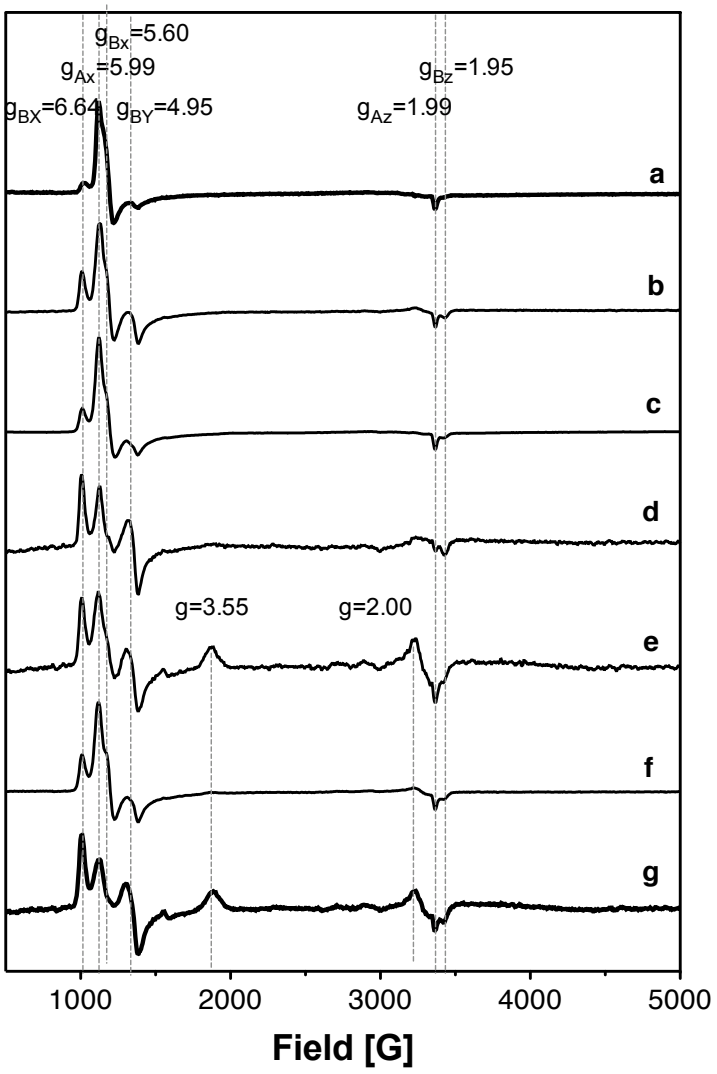

Figure 3.4: EPR spectra of wtKatG and its E695, R126 and W159 substitution variants.

Spectra for ferric wtKatG (a), E695Q (b), E695A (c), R126A (d), R126A/E695A (e), W159A (f), W159A/E695A (g) are shown. Spectrometer settings were as follows: temperature, 10 K; microwave frequency, 9.38 GHz; microwave power, 0.1 mW; modulation amplitude, 10 G; modulation frequency, 100 kHz. The g-values corresponding to RHS 1 (g_{Ax}, g_{Ay}, and g_{Az}) and RHS 2 (g_{Bx}, g_{By}, and g_{Bz}) are shown as those of the HALS-type low spin complex (g=3.55, g=2.0).

species dominated over low-spin states. However, the spectra showed greater detail in the distribution of the various high- and low-spin states present. Similar to the wild-type enzyme, both E695A and E695Q KatG showed a prominent contribution from the rhombic high-spin signal we designate as RHS 2 (g_x=5.99 g_y=5.60 g_y=1.99) with relatively small contributions from the second rhombic signal, RHS 1 (g_x=6.64, g_y=5.60 and g_z=1.95). The same features were observed with the R126A variant, but the distribution among the high spin states was distinct with a greater contribution from the RHS 1 component, and less from the RHS 2 signal. The E695A-bearing double variants (R126A/E695A and W159A/E695A) showed a similar preference for the RHS 1 species, but unexpectedly, a highly anisotropic low spin (HALS)-type EPR signal, characterized by features at g = 3.55, g = 2.00 was also detectable with these variants. This latter spectral feature is proposed to arise due to strain on the heme iron, at the near perpendicular orientation of the imidazole side chains of two histidine ligands [174-176]. To quantify the relative proportions of each species, the spectra were simulated and the individual signals were integrated (Table 3.2).

3.3.3 Steady-state kinetics of R126A, W159A and E595Q:

Single substitutions to intersubunit interface residues resulted in minimal changes in catalase activity as determined by comparing apparent k_{cat} and k_{cat}/K_M values. Even with the double variants, only moderate effects were observed with respect to k_{cat}, and the apparent second-order rate constants were unchanged compared to wtKatG (Table 3.3). Likewise, any substitution to E695, R126 or W159 resulted in only small decreases in peroxidase k_{cat} values with respect to both H_2O_2 *and* the electron donor substrate (ABTS in these studies). The most detrimental substitution with respect to peroxidase activity was R126A, which showed an order

Table 3.2: Ratios of EPR signals observed in wtKatG and its E695, R126 and W159 substitution variants.

Protein	**% contribution**			
	HS[a] : LS[b]	RHS 1[c]: RHS 2[d]	RHS 1: RHS 2 : LS	RHS 1: RHS 2 : LS (H) [e]
wtKatG	92 : 8	24 : 76	22 : 70 : 8	ND [f]
E695Q	97 : 3	60 : 40	58 : 39 : 3	ND
E695A	96 : 4	42 : 58	40 : 56 : 4	ND
R126A	96 : 4	78 : 22	75 : 21 : 4	ND
W159A	95 : 5	56 : 44	53 : 42 : 5	ND
R126A/E695A	ND	69 : 31	ND	34 : 15 : 51
W159A/E695A	ND	80 : 20	ND	40 : 10 : 50

[a] High spin; HS = RHS 1 + RHS 2.

[b] Low spin (g_x = 2.92, g_y = 2.28, g_z = 1.53).

[c] Rhombic high-spin species1 (g_x=6.64, g_y=4.95 and g_z=1.95).

[d] Rhombic high-spin species 2 (g_x=5.99, g_y=5.60 and g_z=1.99).

[e] HALS-type low-spin species (g=3.55, g=2.00).

[f] Not determined.

Table 3.3: Apparent catalase kinetic parameters for wtKatG and its E695, R126 and W159 substitution variants [a]

Protein	Parameter		
	k_{cat} (s^{-1})	K_M (mM H_2O_2)	k_{cat}/K_M (M^{-1} s^{-1})
wtKatG	11500 ± 200	4.5 ± 0.2	2.5×10^6
E695Q	15300 ± 1000	5.3 ± 0.7	2.9×10^6
E695A	9000 ± 500	2.9 ± 0.4	3.1×10^6
R126A	14000 ± 1200	8.0 ± 1.3	1.7×10^6
W159A	13500 ± 1200	2.6 ± 0.6	5.2×10^6
R126A/E695A	7400 ± 600	1.9 ± 0.4	4.0×10^6
W159A/E695A	5900 ± 300	1.7 ± 0.3	3.5×10^6

[a] Assay included 20 nM enzyme in 100 mM phosphate buffer, pH 7.0, 23 °C.

Table 3.4: Apparent peroxidase kinetic parameters for wtKatG and its E695, R126 and W159 substitution variants [a]

Protein	Peroxide-dependent peroxidase parameters			
	k_{cat} (s^{-1})	K_M (mM H_2O_2)	k_{cat}/K_M (M^{-1} s^{-1})	Ki (mM H_2O_2)
wtKatG	72.0 ± 5.1	0.27 ± 0.06	3.60×10^5	27.3 ± 10.4
E695Q	67.9 ± 2.7	0.39 ± 0.04	1.74×10^5	10.1 ± 1.0
E695A	58.8 ± 5.1	0.13 ± 0.03	4.41×10^5	4.6 ± 1.0
R126A	19.0 ± 1.5	0.34 ± 0.07	0.55×10^5	7.4 ± 1.6
W159A	56.3 ± 4.5	0.43 ± 0.08	1.08×10^5	10.1 ± 2.0
R126A/E695A	33.4 ± 2.4	0.17 ± 0.04	1.96×10^5	7.7 ± 1.6
W159A/E695A	40.0 ± 2.0	0.16 ± 0.02	2.50×10^5	6.7 ± 0.9
Protein	**ABTS-dependent peroxidase parameters**			
	k_{cat} (s^{-1})	K_M(mM ABTS)	k_{cat}/K_M (M^{-1} s^{-1})	Ki (mM ABTS)
wtKatG	76.0 ± 4.0	0.134 ± 0.023	5.66×10^5	-
E695Q	40.0 ± 1.0	0.076 ± 0.007	5.26×10^5	-
E695A	57.6 ± 5.2	0.078 ± 0.019	7.38×10^5	-
R126A	39.6 ± 8.9	0.090 ± 0.041	4.40×10^5	0.51 ± 0.2
W159A	35.8 ± 1.2	0.067 ± 0.009	5.34×10^5	-
R126A/E695A	26.9 ± 0.9	0.035 ± 0.006	7.68×10^5	-
W159A/E695A	34.4 ± 0.7	0.065 ± 0.007	5.29×10^5	-

[a] Assay included 20 nM enzyme in in 50 mM acetate buffer, pH 5.0 at 23 °C

of magnitude decrease in k_{cat}/K_M with respect to H_2O_2. Interestingly, R126A was also the only variant to show ABTS- dependent inhibition (Table 3.4). However, the peroxidase activity was not diminished to the same degree for the double substitution variant R126A/E695A, where the apparent k_{cat}/K_M was nearly 50% of that of wtKatG.

3.3.4 The influence of substitution of R126, W159 and E695 on KatG stability:

As mentioned in *Material and methods*, substitution of strictly conserved residues E695 and W159 resulted in the expression of protein in insoluble inclusion bodies using standard expression conditions (i.e., 37 °C). However, soluble protein was obtained if expression was carried out at lower temperatures (i.e., 18 °C). This suggested that these residues might be central to the proper folding and stability of the enzyme. To investigate this further, we evaluated the effect of guanidine hydrochloride (GuHCl) on the secondary structural content of KatG and its variants by far-UV CD. In addition, the sensitivity of the KatG active site to disruption with temperature variation or GuHCl concentration were monitored by UV–visible absorption and stopped-flow spectrophotometry, respectively.

From far-UV CD data, free energies of unfolding were extrapolated and mid-point unfolding concentration (C_m) of GuHCl were determined (Table 3.5). They were all similar for wild-type KatG, E695A, and E695Q. Even the W159 substitution variants showed only modest decreases in the C_m for GuHCl-mediated unfolding in comparison to the wild-type enzyme (Fig. 3.5). In contrast, far greater sensitivity of the *active site* to GuHCl-mediated disruption was observed, with about an order magnitude faster rate constants for heme loss in the presence of 2 M GuHCl for these variants as compared to those measured for the wild-type enzyme. Likewise,

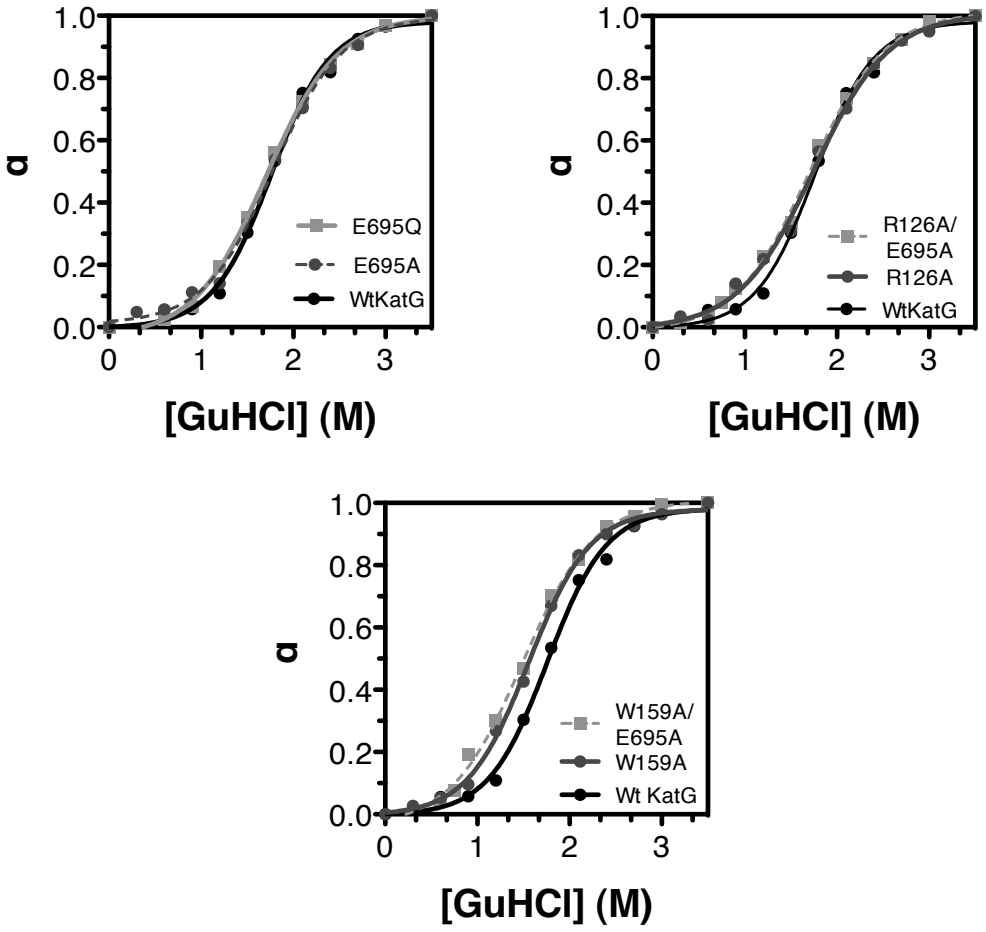

Figure 3.5: GuHCl-mediated unfolding of wtKatG and E695, R126 and W159 substitution variants as monitored by far-UV circular dichroism (CD) spectroscopy.

Table 3.5: Parameters of GuHCl-mediated unfolding wtKatG and E695, R126 and W159 substitution variants.

	Parameter			
Protein	$\Delta G°_{H_2O}$ **(kJ mol $^{-1}$)**	***m*** [a] **(kJ mol^{-1} M^{-1})**	C_m [b] **(M)**	k_{obs} [c] **(s^{-1})**
wtKatG	12.3 ± 0.63	6.86 ± 0.32	1.76 ± 0.03	0.020 ± 0.001
E695A	10.9 ± 0.37	7.00 ± 0.23	1.78 ± 0.03	0.130 ± 0.001
E695Q	12.5 ± 0.44	6.16 ± 0.22	1.71 ± 0.02	0.139 ± 0.030
R126A	10.9 ± 0.59	6.25 ± 0.32	1.74 ± 0.04	0.312 ± 0.024
W159A	10.7 ± 0.45	6.53 ± 0.24	1.56 ± 0.03	0.100 ± 0.011
R126A/E695A	12.0 ± 0.43	7.02 ± 0.24	1.70 ± 0.02	0.604 ± 0.150
W159A/E695A	11.0 ± 0.50	7.10 ± 0.29	1.48 ± 0.02	0.116 ± 0.010
KatG^N	9.63 ± 1.27	51.9 ± 4.8	0.19 ± 0.01	8.77 ± 0.019

[a] *m*, efficacy of GuHCl in unfolding.

[b] C_m, GuHCl concentration with K=[U]/[N]=1

[c] From single exponential fit of $A_{413.9nm}$ decrease in the presence of 2 M GuHCl

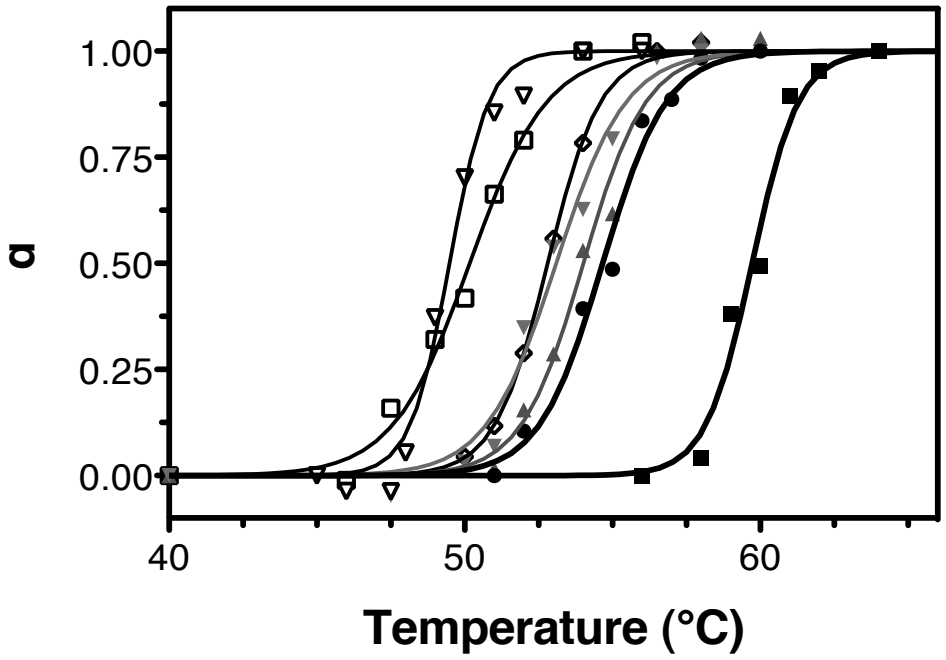

Figure 3.6: Thermal stability of the heme cavity of wtKatG and E695, R126 and W159 substitution variants as monitored by UV-visible absorption due to the heme retention. Enzymes wtKatG (■), E695A (●), W159A (▲), R126A (▼), E695Q (◇), W159A/E695A (□), R126A/E695A (▽) were in 100 mM phosphate buffer, pH 7.0 in a 1.0 cm quartz cell. All spectra backgrounds were calibrated from 350 nm to 450 nm. α was calculated based on derived equation (1), $\alpha = (A_{N\ soret}/A_{380nm} - A_{soret}/A_{380nm})/(A_{N\ soret}/A_{380nm} - A_{U\ soret}/A_{380nm})$.

evaluation of thermally induced heme loss showed that any substitution to E695, R126 or W159 diminished active site stability compared to wtKatG. The midpoint temperatures of transition (T_m) were 6 - 8 °C lower for the single substitution variants and 9 - 10 °C lower for the double substitution variants (Fig. 3.6).

3.3.5 Effect of E695, W159 and E695 substitution on the spectroscopic properties of KatG^C reactivated KatG^N:

The stand-alone N-terminal domain of KatG ($KatG^N$) has neither catalase nor peroxidase activity and the dominant form of heme is a hexacoordinate low-spin complex [142]. Introducing the separately expressed and isolated C-terminal domain ($KatG^C$) results in restructuring of $KatG^N$ as evident from a return of high-spin coordination states typical of wild-type enzyme as well as the restoration of catalase and peroxidase activities [144]. Specifically, incubation of $KatG^N$ with equimolar $KatG^C$ at 4 °C results in a blue shift of the Soret band from 415.5 to 410.5 nm and a decrease in the intensity of the β and α bands at 535 and 560 nm, respectively. Along with this there is an increase in intensity of charge transfer bands at 505 and 640 nm. By EPR, the typical rhombic signal of the hexacoordinate low-spin state (g_x =2.92, g_y =2.28, g_z =1.53) diminishes in intensity along with a pronounced increase in the RHS 2 and RHS 1 signals corresponding to hexacoordinate and pentacoordinate high-spin heme states, respectively [144]. Substitution of E695 in $KatG^C$ or R126 or W159 in $KatG^N$ resulted in a greater residual proportion of hexacoordinate low-spin states after domain incubation than observed with the recombined unmodified domains. The R126A variant most resembled unmodified $KatG^N$, producing a shift in λ_{max} for the Soret band to 411.5 nm; however, W159A (413.5 nm) showed little ability to alter the coordination state of the heme. Interestingly, any substitution of the E695

side chain in $KatG^C$ whether the more dramatic E695A or the more conservative E695Q substitution limited its ability to return of high-spin heme states to the $KatG^N$ active site, producing the maxima of 414.5 nm and 414 nm, respectively. With two substitutions, the ability to change the active site heme coordination state was almost completely abrogated (Fig. 3.7).

A nearly identical trend was observed by EPR spectroscopy (Fig. 3.8). As before the relative proportions of high-spin and low-spin species were estimated by integration and simulation of the individual EPR spectra (Table 3.6). Any single substitution to R126 and E695 limited the return of $KatG^N$ to active high-spin heme states. The most detrimental substitution was E695A, which showed the greatest proportion of low-spin species followed by E695Q and R126A. We also noticed that substitution of W159 resulted in a protein with poor heme binding property as shown from EPR spectra. Its activation by $KatG^C$ or its variants showed similar EPR features distinct from that of $KatG^N$. By UV-vis and EPR spectroscopy, the double variants R126A/E695A and W159A/E695A showed little ability to alter the N-terminal domain active site heme coordination state.

3.3.6 Effect of E695, W159 and E695 substitution on the catalytic function of $KatG^C$ reactivated $KatG^N$:

As we have observed previously, both catalase and peroxidase activities reemerge concomitant with the spectral changes associated with incubation of $KatG^N$ with $KatG^C$ [144]. The steady-state kinetic parameters for catalase and peroxidase activities following $KatG^N$ reactivation are shown in Table 3.7 and Table 3.8, respectively. Any substitution to E695, R126 or W159 diminished recovery of catalase and peroxidase activities. The effect was most

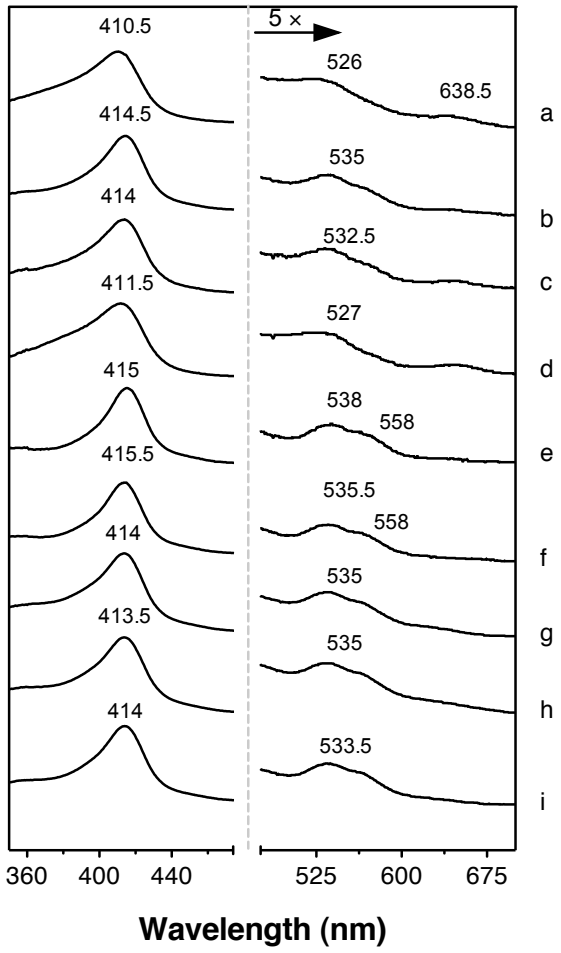

Figure 3.7: UV-visible absorption spectra of KatG^{N} (or its R126A, W159A substitution variants) following incubation with KatG^{C} (or its E695A, E695Q substitution variants). Spectra were recorded for the following combinations: KatG^{N}+KatG^{C} (a), KatG^{N}+E695AKatG^{C} (b), KatG^{N}+E695QKatG^{C} (c), R126AKatG^{N}+KatG^{C} (d), R126AKatG^{N}+E695AKatG^{C} (e), KatG^{N} (f), W159AKatG^{N} (g), W159AKatG^{N}+KatG^{C} (h) and W159AKatG^{N}+E695A KatG^{C} (i). All reactions contained 10 μM KatG^{N} (or variant thereof) and, if present, equimolar KatG^{C} (or variant thereof). All incubations were carried out for 96 h at 4 °C in the presence of 100 mM phosphate buffer, pH 7.0. Spectra were recorded using the same buffer at 23 °C

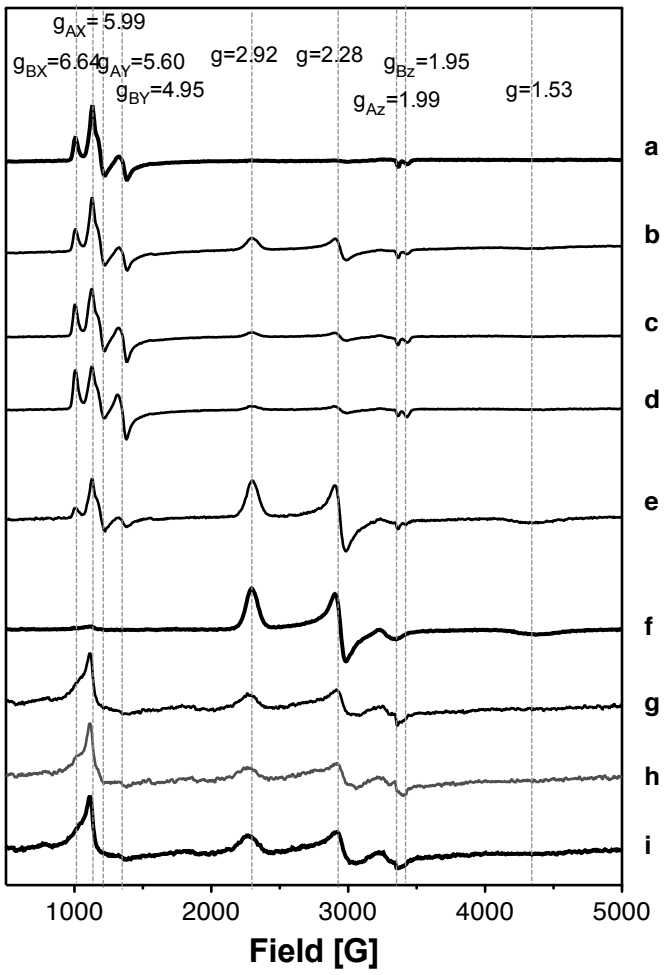

Figure 3.8: EPR spectra of KatG^N (or its R126A, W159A substitution variants) following incubation with KatG^C (or its E695A, E695Q substitution variants).

Spectra were recorded for the following combinations: KatG^N+KatG^C (a), KatG^N+E695A KatG^C (b), KatG^N+E695QKatG^C (c), R126AKatG^N+KatG^C (d), R126AKatG^N+E695AKatG^C (e), KatG^N (f), W159AKatG^N (g), W159AKatG^N +KatG^C (h), W159AKatG^N+E695AKatG^C (i). The g-values corresponding to RHS 1 (g_{Ax}, g_{Ay}, and g_{Az}) and RHS 2 (g_{Bx}, g_{By}, and g_{Bz}) are shown as those of the hexacoordinate low spin complex (g_x, g_y, and g_z). All incubations were carried out as described for Fig. 3.7, and spectrometer settings were as described for Fig. 3.4.

Table 3.6: Ratios of EPR signals observed following $KatG^N$ (or its R126A, W159A substitution variants) following incubation with $KatG^C$ (or its E695A, E695Q substitution variants)

Protein		**% Contribution**	
	HS[a] : LS[b]	RHS 1[c]: RHS 2[d]	RHS 1: RHS 2 : LS
$KatG^N$+$KatG^C$	94 : 6	63 : 37	59 : 35 : 6
$KatG^N$+E695A $KatG^C$	45 : 55	60 : 40	27 : 18 : 55
$KatG^N$+E695Q$KatG^C$	64 : 36	71 : 29	45 : 18 : 36
R126A$KatG^N$+$KatG^C$	67 : 33	75 : 25	50 : 17 : 33
R126A$KatG^N$+E695A$KatG^C$	15 : 85	50 : 50	7 : 7 : 85
$KatG^N$	0 : 100	0 : 0	0 : 0 : 100

[a] High Spin; HS = RHS 1+RHS 2

[b] Low Spin (g_x =2.92 , g_y =2.28 , g_z =1.53)

[c] Rhombic high-spin species 1 (g_x=6.64, g_y=4.95 and g_z=1.95)

[d] Rhombic high-spin species 2 (g_x=5.99, g_y=5.60 and g_z=1.99)

pronounced with W159A substitution and progressively less for E695A, R126A, and least for E695Q. The R126A and E695A substitution appeared to be additive as the R126A $KatG^N$ + E695A $KatG^C$ combination, recovered only half the catalase activity of $KatG^N$ + E695A$KatG^C$; and W159A $KatG^N$ + E695A $KatG^C$ combination completely lost the ability to restore catalytic function to the N-terminal domain. Notably, the trend of reactivation of peroxidase activity was not the same as that of catalase activity. Any substitution to these residues limited recovery of peroxidase activity. This effect was more dramatic upon substituting the residues (R126 and W159) in the stand-alone N-terminal domain (Table 3.8).

Any substitution to E695, R126 and W159 diminished the first order rate constant associated with $KatG^N$ functional recovery. The largest effect was observed with the W159A variant followed by E695Q, E695A, and finally R126A (Fig. 3.9, Table 3.7). Interestingly, the E695Q substitution had the smallest effect on the amplitude of catalase activity recovery, but the rate constant was one order magnitude below that observed for the unmodified $KatG^C$. With two substitutions (i.e, R126A$KatG^N$ + E695A$KatG^C$), the rate constant for activity recovery was decreased by an order of magnitude. As observed above, W159A $KatG^N$ + E695A $KatG^C$ showed little capacity to restructure the N-terminal domain active site. Thus, it was not surprising to find little, if any, ability to recover either catalase or peroxidase activity.

3.5 Discussion:

3.5.1: Intrasubunit interactions *vs.* intersubunit interactions:

The C-terminal domain of KatG is a structure found in all catalase-peroxidases. It appears to have arisen from gene duplication and fusion of a predecessor peroxidase [118]. The

Table 3.7: Apparent catalase kinetic parameters for $KatG^N$ (or its R126A, W159A substitution variants) following incubation with $KatG^C$ (or its E695A, E695Q substitution variants) [a]

Protein	**Catalase cycle parameter[a]**			**Reactivation[a,b]**
	k_{cat} (s^{-1})	K_M (mM H_2O_2)	k_{cat}/K_M (M^{-1} s^{-1})	k_{obs} (10^{-5} s^{-1})
$KatG^N$+$KatG^C$	4000 ± 350	2.4 ± 0.6	1.7×10^6	3.83 ± 0.56
$KatG^N$+E695A $KatG^C$	1000 ± 200	6.0 ± 1.9	0.2×10^6	0.81 ± 0.11
$KatG^N$+E695Q $KatG^C$	2600 ± 90	2.2 ± 0.2	1.8×10^6	0.55 ± 0.07
R126A$KatG^N$+$KatG^C$	1700 ± 90	1.7 ± 0.3	1.0×10^6	2.35 ± 0.30
R126A$KatG^N$+E695A$KatG^C$	550 ± 40	1.3 ± 0.3	0.4×10^6	0.54 ± 0.12
W159A$KatG^N$+$KatG^C$	230 ± 10	2.5 ± 0.4	0.1×10^6	0.36 ± 0.14
W159A$KatG^N$+E695A$KatG^C$	ND [c]	ND	ND	ND

[a] All assays included 50 nM enzyme in 100 mM phosphate buffer, pH 7.0, at 23 °C.

[b] Incubation conditions for reactivation: 100 mM phosphate buffer, pH 7.0, at 4 °C.

[c] Not determined.

Table 3.8: Apparent peroxidase kinetic parameters for $KatG^N$ (or its R126A, W159A substitution variants) following incubation with $KatG^C$ (or its E695A, E695Q substitution variants) [a]

Protein	**Peroxide-dependent peroxidase parameters**			
	k_{cat} (s^{-1})	K_M (mM H_2O_2)	k_{cat}/K_M (M^{-1} s^{-1})	K_I (mM H_2O_2)
$KatG^N$+$KatG^C$	56.3 ± 2.9	0.42 ± 0.06	1.34×10^5	9.80 ± 1.4
$KatG^N$+E695A$KatG^C$	5.60 ± 0.4	0.04 ± 0.01	1.40×10^5	7.30 ± 1.5
$KatG^N$+E695Q$KatG^C$	16.3 ± 2.1	0.10 ± 0.03	4.41×10^5	11.0 ± 4.7
R126A$KatG^N$+$KatG^C$	3.60 ± 0.2	0.09 ± 0.02	0.04×10^5	10.9 ± 2.3
W159A$KatG^N$+$KatG^C$	0.50 ± 0.1	0.03 ± 0.01	0.02×10^5	27.2 ± 7.2
R126A$KatG^N$+E695A$KatG^C$	2.30 ± 0.1	0.08 ± 0.01	0.03×10^5	9.30 ± 1.4
W159A$KatG^N$+E695A$KatG^C$	ND	ND	ND	-
Protein	**ABTS-dependent peroxidase parameters**			
	k_{cat} (s^{-1})	K_M(mM ABTS)	k_{cat}/K_M (M^{-1} S^{-1})	K_I (mM ABTS)
$KatG^N$+$KatG^C$	48.7 ± 1.1	0.068 ± 0.007	6.96×10^5	-
$KatG^N$+E695A$KatG^C$	6.10 ± 0.1	0.039 ± 0.003	1.56×10^5	-
$KatG^N$+E695Q$KatG^C$	17.7 ± 0.4	0.043 ± 0.004	4.11×10^5	-
R126A$KatG^N$+$KatG^C$	6.40 ± 0.4	0.014 ± 0.002	4.57×10^5	0.231 ± 0.04
W159A$KatG^N$+$KatG^C$	0.50 ± 0.1	0.032 ± 0.007	0.15×10^5	-
R126A$KatG^N$+E695A$KatG^C$	5.00 ± 1.9	0.089 ± 0.053	0.56×10^5	0.144 ± 0.07
W159A$KatG^N$+E695A$KatG^C$	ND	ND	ND	-

[a] Assay included 20 nM enzyme in in 50 mM acetate buffer, pH 5.0 at 23 °C

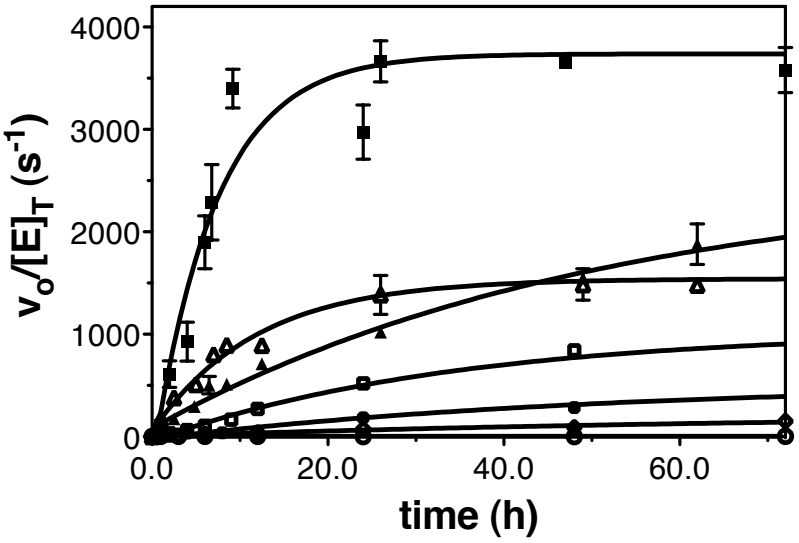

Figure 3.9: Time course for recovery of KatG^N (or its R126A, W159A substitution variants) catalase activity upon addition of equimolar KatG^C (or its E695A, E695Q substitution variants).

Activity measurements were made for the following combinations: KatG^N+KatG^C (■), KatG^N+E695QKatG^C (▲), KatG^N+E695AKatG^C (□), R126AKatG^N+KatG^C (△), W159AKatG^N+KatG^C (◇), R126AKatG^N+E695AKatG^C (●), W159AKatG^N+E695AKatG^C (○). Incubations were carried out at 4 °C in 100 mM phosphate buffer, pH 7.0. Assays of the activity contained 50 nM KatG^N (or variant thereof) and KatG^C (or variant thereof), 10 mM H_2O_2, and 100 mM phosphate buffer, pH 7.0. Assays were all performed at 23 °C.

functional adaption to this event appears to have resulted in an N-terminal domain with the ability to oxidize and reduce hydrogen peroxide and remain peroxidatically active. In contrast, the C- terminal domain has lost the ability to even bind heme, let alone catalyze any reaction with it. Because it is clear that the C-terminal domain does not bring an activity of its own, it is reasonable to suppose that it may address the needs of the N-terminal domain through several points of contact by which it may direct conformational adjustments, maintain the active site coordination environment and fine tune for bifunctional activity [144]. This is verified by visual inspection of the crystal structures for KatG enzyme that show substantial interactions between the two domains [119, 120, 122, 146], and supported further by the effect not only of deletion of the C-terminal domain, but also its reintroduction as a separately expressed and isolated protein [142, 144].

Interestingly, the effect of removing the C-terminal domain from KatG produces very similar results as removal of calcium from fungal secretory peroxidases (i.e., class II enzymes like lignin peroxidase). Specifically, there is a shift in heme coordination from pentacoordinate high-spin to hexacoordinate low-spin. In the class II enzymes, calcium is coordinated above the B-helix, and its loss due to temperature increase or disruption of its coordination environment by mutagenesis allows the distal histidine (a residue found on the B-helix) to coordinate the heme iron (Fig. 3.12) [81, 169, 177-179]. It is striking that the class III peroxidases (e.g., horseradish peroxidase) contain a calcium ion in essentially the same position. However, in these enzymes the metal iron coordination site is further stabilized by a disulfide bond where the two cysteine residues straddle aspartate residues that serve to coordinate the calcium [65, 180]. None of the class I enzymes, including KatG contain Ca^{2+} nor is there a disulfide bond at the analogous

position. However, in the case of KatG there are extensive *intra*subunit contacts between the BC loop of the N-terminal domain and the B'C' loop from the C-terminal domain. Along the two-domain interface, residues contribute to two prominent hydrogen-bonded networks (Tyr 111-Asp 482-Arg 479 and Arg 117-Asp 597) both of which are highly conserved. These interactions would appear to have the same capacity to stabilize the B-helix and prevent the distal histidine from entering the coordination sphere of the heme iron (Fig. 3.10). However, previous studies from the Goodwin laboratory have shown that disruption of these hydrogen-bonded networks is sufficient neither to replicate the effects observed in KatG upon removal of its C-terminal domain nor those in class II peroxidase upon removal calcium [181]. These data tend to suggest that the C-terminal domain may direct the active site structural adjustment through some other points of contact with N-terminal domain.

As revealed in Chapter 2, the I'-helix which appears at the intersubunit interface plays an essential role in stabilizing the N-terminal domain in its active conformation, as multiple substitutions to this structure produced substantial increases in the population of hexacoordinate low-spin heme and diminished enzyme activity, similar to that observed with N-terminal domain on its own ($KatG^N$). Indeed, multiple substitutions to the I'-helix produced a KatG with spectroscopic and kinetic properties, as well as thermodynamic stability, virtually indistinguishable from $KatG^N$. We noted that substitution of E695 was especially destructive to KatG active site integrity; the stability at the active site level was substantially compromised as observed by the thermally-induced loss of active site heme.

3.5.2: Connecting the I'-helix to the active site:

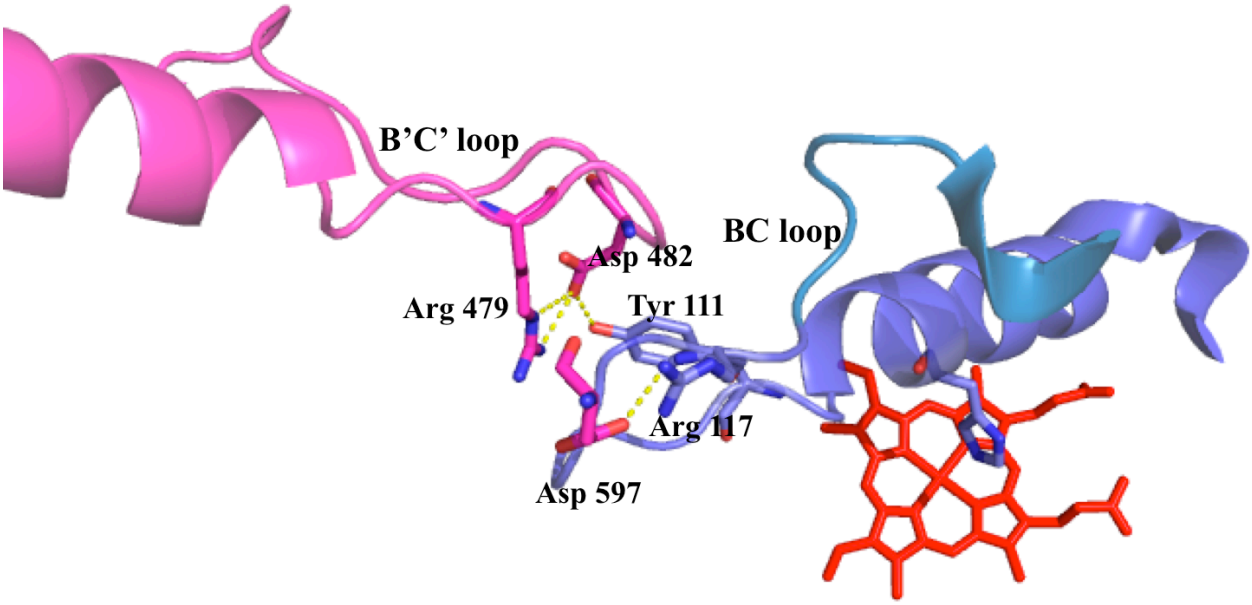

Figure 3.10: Interactions between the N-terminal domain BC loop and the B'C' loop from the intrasubunit C-terminal domain.

Coordinates from the structure of *Mycobacterium tuberculosis* KatG were used (PDB: 2CCA). Numbering reflects *E. coli* KatG sequence. Dashes indicate the inferred polar contacts.

Although the I'-helix clearly has an essential role in maintaining the conformation and integrity of active site, the mechanisms by which this structure connects to the active site and controls its conformation are not clear. Visual inspection of crystal structures shows that E695 makes contacts with several core structures of N-terminal domain with connections to the active site. One of these is an apparent H-bond with strictly conserved W159 where the indole nitrogen appears to be a H-bond donor to the E695 carboxylate. Further, E695 coordinates one or two water molecules in conjunction with the R126 side chain between two domains [119, 120, 122, 146].

At first glance, replacement of W159 with alanine did not appear to produce any notable defect in KatG structure or function as evaluated by its nearly identical spectral and kinetic properties to wtKatG. Even in terms of global protein structural stability, this substitution only resulted in modest losses as evaluated by effects of denaturing agents on overall secondary structural content. In contrast, the protein stability at the active site level was substantially compromised as observed by thermally induced loss of active site heme similar to what we observed in E695A. This was further corroborated by the analogous variant in $KatG^N$, which retained little if any ability to respond to active site restructuring by $KatG^C$. Interestingly, substitution of R126 with alanine produced results highly similar to the W159A variant where the most obvious detriment to the function of the enzyme was the stability of its active site to temperature and denaturants. Taken together, the impacts of single substitutions on KatG were most obvious in the stability of the active site, indicating these residues are the key connections through which the remote I'-helix controls the active site integrity and conformation.

Visual inspection of crystal structures of KatGs shows that the R126 guanidinium group anchors another hydrogen-bonded network through another well-ordered water molecule and strictly conserved D187 (Fig. 3.11). This network includes the backbone carbonyl oxygen of Arg 122 (Gly in *M.tuberculosis* KatG), the backbone of which further associates with another water molecule that appears to stabilize the BC loop located above the B-helix bearing the distal His (Fig. 3.11). These well-ordered water molecules which are observed in all structures of KatG enzymes provide a potential connection from the remote I' helix to R126, and finally to the active site (Fig. 3.12). As we mentioned previously, in class II (e.g. manganese peroxidase) and III peroxidases, which depend on Ca^{2+} to maintain a heme coordination environment that supports activity, the relevant calcium-binding site is established in part by this same portion of the BC loop. Therefore, it is reasonable to predict that these extended hydrogen-bonded networks serve in similar roles roles as those of the distal Ca^{2+} in manganese peroxidases to maintain the heme coordination environment. Indeed, our data are consistent with this hypothesis, disruption of the H-bonds between R126 and E695 by double substitutions (R126A/E695A) showed a greater propensity to form a hexacoordinate low-spin state as well as clear compromises to active site stability.

3.5.3: Multiple substitutions *vs.* single substitution:

The most obvious impact of multiple substitutions is that double substitutions have a greater effect on the thermal stability of the active site, consistent with our hypothesis that the remote I'-helix controls the active site integrity through these interactions. In addition, the EPR spectra of R126A/E695A and W159A/E695A both exhibited highly anisotropic low-spin signals termed HALS-type EPR spectra. This type of spectrum, as distinct the more typical rhombic

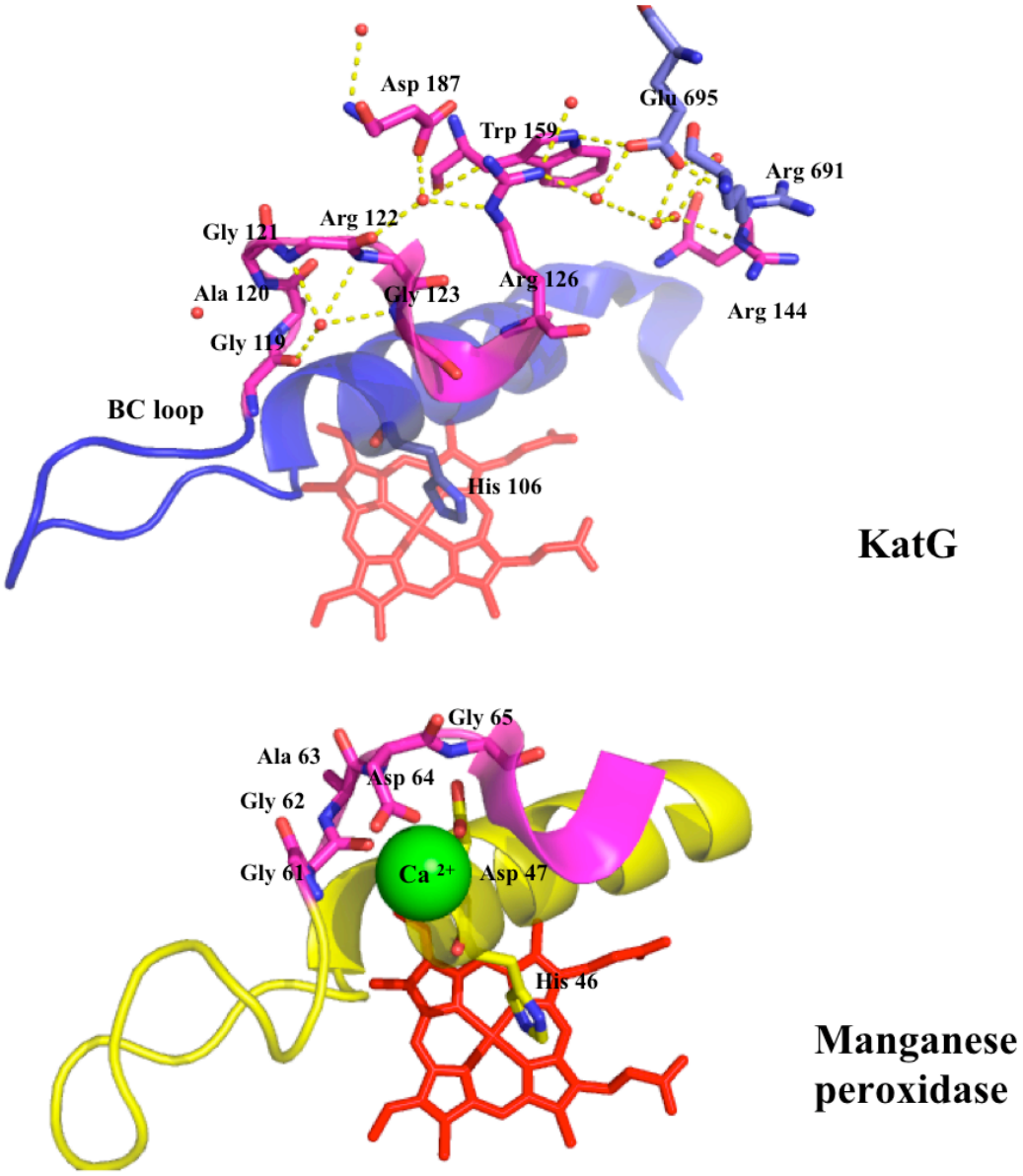

Figure 3.11: Interactions between R126, W159 and E695 and a water-mediated hydrogen-bonded network along the BC loop (upper); BC loop in manganese peroxidase and Ca^{2+} (bottom).

Coordinates from the structure of *Mycobacterium tuberculosis* KatG (PDB: 2CCA) and manganese peroxidase were used (PDB: 1MNP). Numbering reflects *E. coli* KatG.

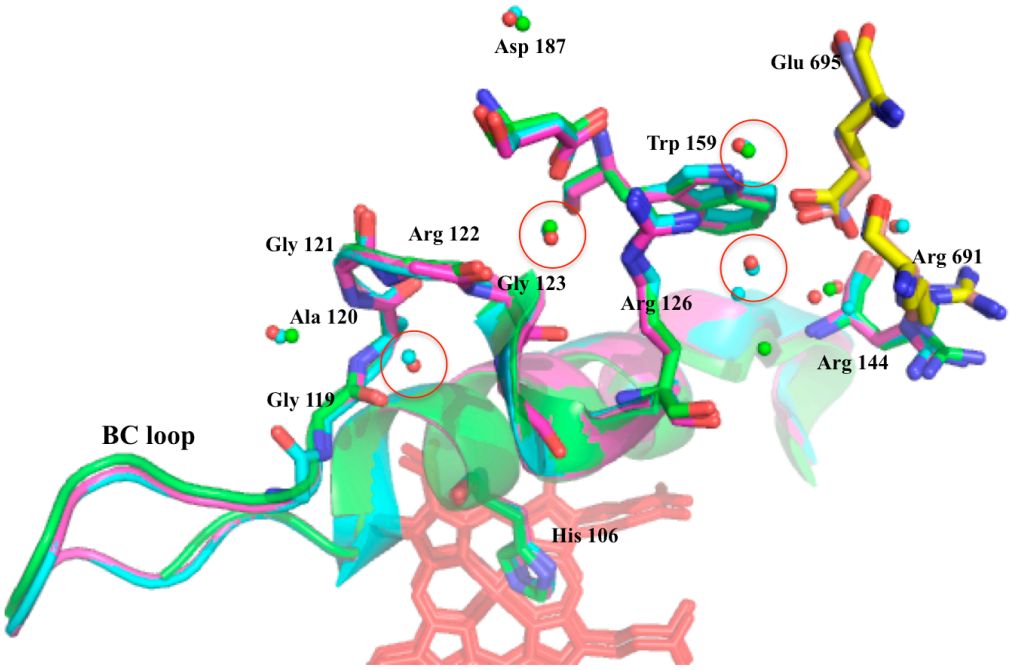

Figure 3.12: Overlaid structures of KatGs and the water molecules.

(PDB: 2CCA, 1SJ2 and 1MWV). Numbering reflects *E. coli* KatG sequence. Spheres represent water molecules. Red circles highlight the invariant water molecules in these three structures.

signal, is purported to arise from the orientation of the planes of the imidazoles of the two histidine ligands. A perpendicular orientation of the planes relative to one another produces the HALS-type spectrum, whereas the parallel alignment produces the typical rhombic low spin signal (g_x =2.93, g_y =2.28, g_z =1.53) (i.e., that which we observe for $KatG^N$). This shift indicates the distal His must undergo a change in orientation relative to the heme. One possible explanation is multiple substitutions interrupting the water-mediated interactions between R126, W159 and E695 may lead to the loss of polar contacts between R126, D187 and R122. Loss of these contacts along BC loop may ultimately lead to modest shifting of B-helix, allowing a shift in orientation of the distal His. Furthermore, the effects of multiple substitutions on active site heme coordination state and enzyme activity, especially for R126A/E695A, were more dramatic. It is noteworthy that the influence of multiple substitutions appears to be additive. This additive influence is also apparent in the reactivation of the stand-alone N-terminal domain. One possible explanation is that each one of the target amino acids plays multiple roles, one of which is through interaction with this connection to the active site.

3.5.4: E695Q *vs.* E695A:

Interestingly, substitution of E695 with either alanine or glutamine produced proteins with similar stability as well as spectroscopic and kinetic properties, indicating the water molecule-mediated polar contacts between E695 and R126 are essential. In addition to association with W159 and R126, E695 appears to participate in another network including R691 and R144 through a water matrix. Given that these are all polar contacts, it seems odd that E695Q would be more similar in properties to E695A than the wild-type enzyme. However, given that all of the residues in these networks with E695 are H-bond donors (W159 indole N-H, R144, and R126),

to accommodate the appropriate H-bonding through intervening H_2O molecules. Therefore, a side chain that behaves as an exclusive H-bond acceptor is necessary. In this, glutamate but not glutamine, is ideal. Therefore, even the very subtle modification E695Q was sufficient to substantially destabilize the enzyme active site.

In summary, our previous studies demonstrated a central role for the I'-helix of the C-terminal domain in maintaining active site conformation and stability. A large distance separates this structure from the active site, and it was not clear how this effect is communicated to the active site. Available structures of KatG reveal that E695 in I'-helix is a central component of several hydrogen-bonded networks also including strictly conserved R126 and W159 from the adjacent N-terminal domain and a well-ordered water matrix from domain interface to active site which appear to stabilize the BC loop. Indeed, disruption of these interactions in the intact protein had little effect on the catalytic function and the stability of global structure of the protein but had a profound impact on the stability of the active site. In addition, substitutions of these residues substantially decreased the reactivation of $KatG^N$ by $KatG^C$. These studies demonstrate a clear connection between the I'-helix and active site conformation and function.

CHAPTER FOUR

BORROWING THE *E.COLI* CATALASE-PEROXIDASE C-TERMINAL DOMAIN AS A SCAFFOLD FOR GENERATION OF NEW HEME-DEPENDENT CATALYSTS

4.1 Introduction:

Of reactive oxygen species, H_2O_2 is the most frequently observed in biological systems. In most organisms, H_2O_2 is scavenged by either catalases or peroxidases [147]. Catalase-peroxidases (KatGs) are unique in that they use a single active site to carry out both peroxidase and substantial catalase activities. KatGs all have a two-domain structure, where each domain resembles a plant peroxidase with respect to its sequence and three-dimensional structure. These data suggest that the two-domain structure arose from the fusion of two adjacent genes following a gene-duplication event [118, 119]. In the intervening time, it would appear that the N-terminal domain has maintained the heme-dependent active site. In contrast, the C-terminal domain has lost its ability to bind heme and catalyze any reaction of its own. Due to its large separation from the N-terminal domain active site (≥30 Å), it cannot play a *direct* role in the catalytic function of that domain either. Nevertheless, the C-terminal domain is essential to KatG function as without it, the protein is no longer expressed in soluble form but is instead found in inclusion bodies. In addition, following denatured purification, refolding and reconstitution, the stand-alone N-terminal domain ($KatG^N$) shows a shift in its active site structure, allowing the direct

coordination of the distal histidine to the heme iron. Consequently, $KatG^N$ has neither catalase nor peroxidase activity [142, 144].

Sequence alignments and structural comparisons show that the "inactive" C-terminal domain retains all 10 major helices of a typical peroxidase, strongly resembles the N-terminal domain and other members of the peroxidase-catalase superfamily (e.g. cytochrome *c* peroxidase [CCP] and ascorbate peroxidase [APX]) [119]. Indeed, an overlay of CCP and the KatG C-terminal domain indicates that the latter retains the helical architecture and topological arrangement of a typical plant peroxidase [143] (Fig. 4.1). However, even though the active site framework is present, the basis for the lack of catalytic function in the C-terminal domain is also readily apparent. With respect to heme binding, there are two side chains within the C-terminal domain vestigial "active site" that are conspicuously different than the functional active sites of the peroxidase-catalase superfamily. First, the typical His ligand for the heme has been replaced by an Arg (617 by *E. coli* numbering). Adjacent to R617, M616 appears in place of a glycine, alanine or serine residue. The large aliphatic methionine side chain protrudes into the cavity normally occupied by the heme. The other difference is the presence of a loop that serves to insert an additional hydrophobic side chain into the space vacated by the heme and to cap access to the site using an Arg side chain (Fig. 4.2).

The typical distal side histidine, a general acid/base catalyst, is replaced by A473 [182-184]. Likewise, at position 469, the arginine purported to stabilize developing negative charge on the distal oxygen of the peroxide substrate is replaced by a serine [182, 183, 185].

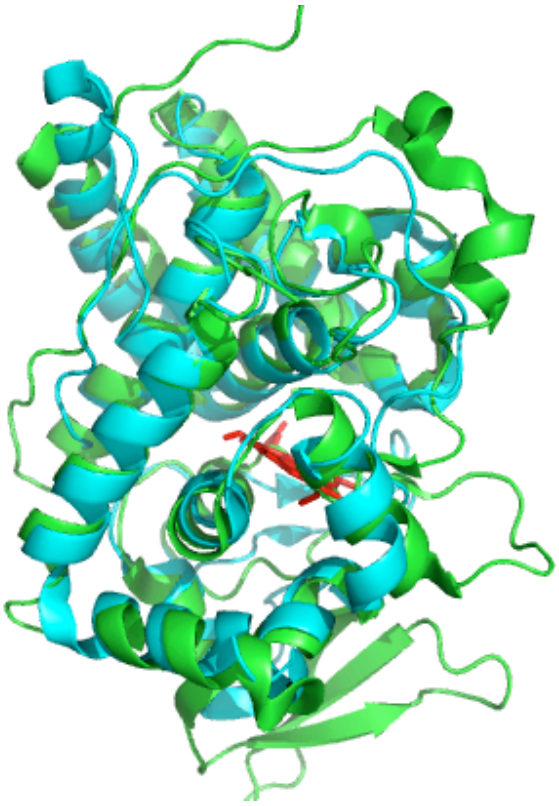

Figure 4.1: Overlaid structures of KatG^{C} (green) and CCP (cyan) with a bound Heme (red).

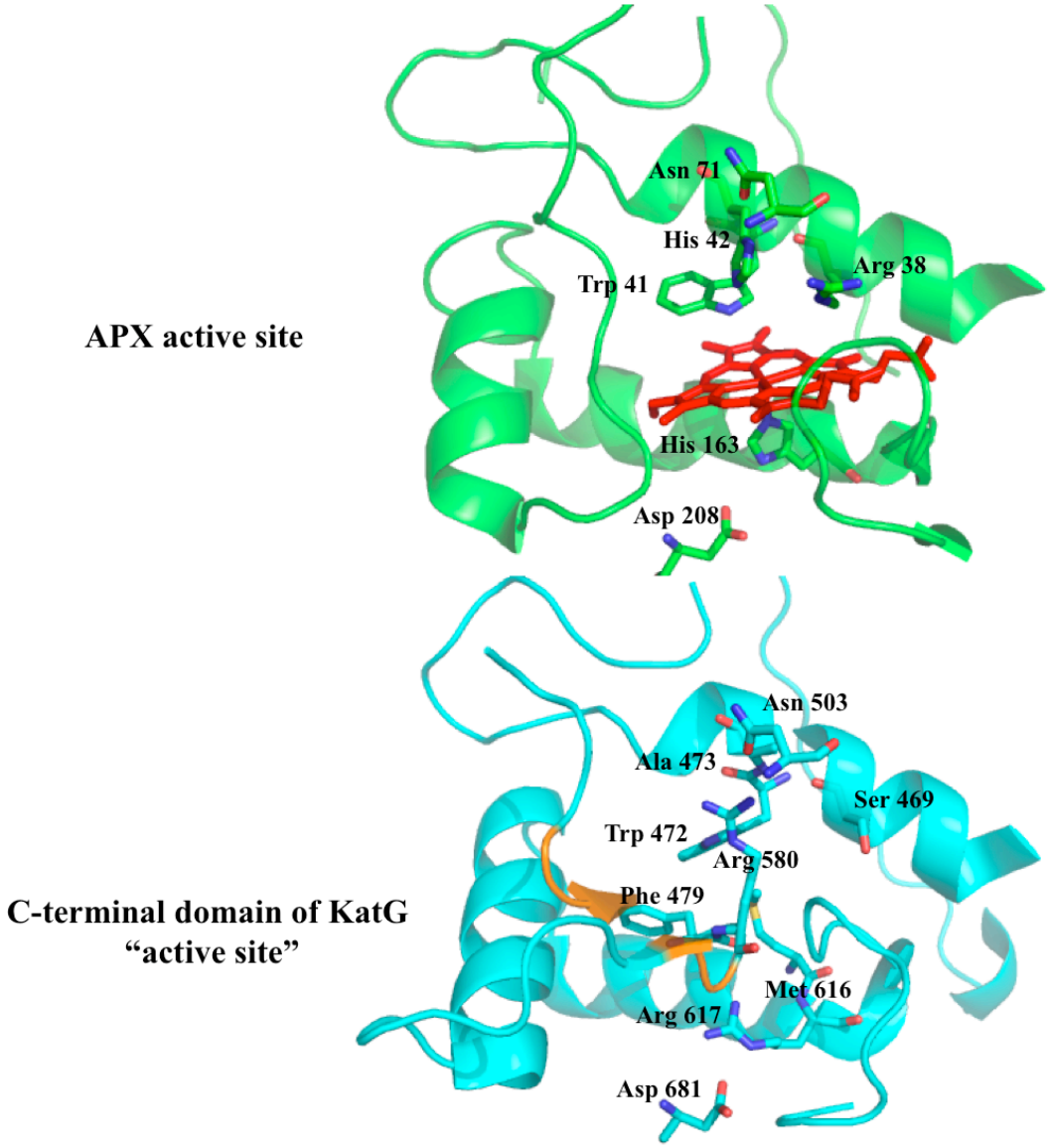

Figure 4.2: Comparison of the "active site" environments of APX and KatG^{C}.

APX (PDB: 1OAF), KatG^{C} (PDB: 1U2K)

Interestingly, the distal active site tryptophan is retained as W472, and the H-bond partners of the proximal and distal histidines are retained as D681 and N503, respectively (Fig. 4.2) [70, 186-190]. Taken together, these data indicate that the C-terminal domain may provide an ideal "blank slate" for engineering new heme-dependent catalysts. The objective of this study was to capitalize on the existing active site framework of the C-terminal domain as a starting point for engineering new heme-dependent peroxidative catalysts based on the separately isolated C-terminal domain ($KatG^C$). Here, UV-vis absorption, MCD and EPR spectroscopy were used to evaluate the heme-binding environment, and steady kinetic analyses were employed to evaluate the restoration of peroxidase activity.

4.2 Materials and methods:

4.2.1 Materials:

Hydrogen peroxide (30%), imidazole, hemin, ampicillin, chloramphenicol, sodium dithionite, phenylmethylsulfonyl fluoride (PMSF), 2,2′-azino-bis (3-ethylbenzthiazoline-6-sulfonate) (ABTS) were purchased from Sigma (St. Louis, MO). Isopropyl-β-d-thiogalactopyranoside (IPTG), urea, mono- and dibasic sodium phosphate, acetic acid, and sodium acetate were obtained from Fisher (Pittsburgh, PA). Benzonase was purchased from Novagen (Madison, WI). All restriction enzymes were purchased from New England Biolabs (Beverly, MA). All oligonucleotide primers were purchased from Invitrogen (Carlsbad, CA). All *E. coli* strains (BL-21-Gold [DE3] pLysS and XL-1 Blue), *Pfu* polymerase, and T4 DNA ligase were obtained from Agilent (La Jolla, CA). Nickel-nitrilotriacetic acid (Ni-NTA) resin was purchased from Qiagen (Valencia, CA). All buffers and media were prepared using water purified through a Barnstead EasyPure II system (18.2 MΩ/cm resistivity).

4.2.2 Cloning:

With the exception of the M616A/R617H variant, plasmids encoding variants of $KatG^C$ were prepared using mutagenic coding and non-coding primers according to the "Round-the-Horn" procedure [152]. The M616A/R617H variants expression construct was prepared using the QuickChange procedure with the complementary primers (Table 4.1). Amplification products from "Round-the-Horn" procedure were subjected to blunt-end ligation with T4 DNA ligase and used to transform *E. coli* (XL-1) Blue by a standard heat shock procedure. Plasmids from candidate colonies were isolated based on conferred ampicillin resistance and evaluated by diagnostic restriction digest (see Table 4.1). Plasmids from positive candidates were subjected to DNA sequence analysis to verify that the correct mutation had been incorporated without any unintended mutations. Plasmids verified to carry the correct mutations were used to transform our *E. coli* expression host (BL-21 *Gold* [DE3] pLysS).

4.2.3 Expression and Purification:

Expression was carried out in *E. coli* (BL-21-Gold [DE3] pLysS) using cultures supplemented with ampicillin and chloramphenicol as previously described. The $KatG^C$ was expressed in a soluble form and purified as previously described [144]. $KatG^N$, and all variants of $KatG^C$ variants were expressed in inclusion bodies. Therefore, purification was carried out according to the procedure previously described for $KatG^N$ (see Chapter 2). Concentrations of purified enzyme were estimated according to the method of Gill and von Hippel [154].

Table 4.1: Primer sets for site-directed mutagenesis of $KatG^C$

	Primer Sequences:	Restriction enzymes
M616G/R617H	TGGTGGGCGGCGGCCACGTACTGGGTG CACCCAGTACGTGGCCGCCGCCCACCA	***Sph I***
G614A/M616G/R617H	5'-Phos-GCCGGCGGTCATGTACTGGGTG-3' 5'-Phos-CACCAGCGCAGTCATTTCCGGC-3'	***Ngo MI***
Δ575-582	5'-Phos-CGCGCTCGTCTGGACGTTT-3' 5'-Phos-TGGCTCCAGCAGCTCAAACA-3'	***Mfe I***
A473H	5'-Phos-TGGCCTGGCACAGCGCTTCTACCTT-3' 5'-Phos-CCGATACCAGCTCACTAACAGACAGACCAGAATC-3'	***Afe I***
S469R/A473H	5'-Phos-CGTGGCCTGGCATTCTGCTTCTACCTTCC-3' 5'-Phos-CGTACCAGCTCACTAACAGACAGACCAGAATCCG-3'	***Mlu I***

4.2.4 Enzyme reconstitution and heme absorption spectra:

Due to the poor solubility of hemin at neutral and acidic pH, hemin solutions for reconstitution were prepared by dissolving solid hemin in 0.1 M KOH. Hemin concentration was determined by the method of Falk [155] and 0.75 equivalents added to modified KatG^{C} variants. These solutions were allowed to incubate for at least 24 h at 4 °C. The reconstituted enzyme solution was then centrifuged in order to remove precipitated heme and other insoluble material. Concentrations of reconstituted enzymes were determined using the pyridine hemichrome assay [155]. Protein containing heme in the ferrous state was prepared by adding a small amount (<10 mg) of sodium dithionite to the ferric form of the enzyme. All spectra were obtained at room temperature on a Shimadzu UV-1601 spectrophotometer (Columbia, MD) with a cell path length of 1.0 cm.

4.2.5 Peroxidase activity assays and spectroscopy:

Peroxidase assays and initial velocity fitting were performed as described in Chapter 2. If inhibition was evident, the fitting equation was modified to a general substrate-dependent inhibition model (Chapter 2) [191]. Settings and parameters of (magnetic) circular dichroism (CD) and Electron Paramagnetic Resonance (EPR) measurements were the same as described in Chapter 2.

4.3 Results:

4.3.1 Engineering strategy:

In order to restore heme binding capability to KatG^{C}, we used site-directed mutagenesis to substitute R617 with histidine and M616 with glycine (HB1) (Table 4.2). In doing so, an

appropriate ligand for heme binding was introduced and a large aliphatic side chain obstructing the active site cavity was removed, respectively. This modification resulted in a contiguous stretch of three glycine residues (G614, G615 and M616G). We were concerned that the conformational flexibility resulting from three consecutive glycines would be overly disruptive to the $KatG^C$ structure. Thus, we replaced the first glycine in the sequence with alanine (i.e., G614A), a variant we designated as HB2. We anticipated that the apex of an extended loop may obstruct heme binding by the HB1 and HB2 vaiants. Variants from which this structure was excised were generated from HB1 and HB2, generating HB1a and HB2a, respectively). Of these variants, HB2a showed the spectroscopic features that seemed most appropriate for further modification. Therefore, HB2a was modified sequentially by site directed mutagenesis to produce the A473H and S469R/A473H variants (His as a general base/acid and Arg as an electrostatic catalyst) generating PX1 and PX2, respectively, with the purpose of restoring peroxidase activity.

4.3.2 Mutagenesis, expression and purification of $KatG^C$ and its variants:

As confirmed by DNA sequence analysis, we successfully produced constructs for expression of all of these $KatG^C$ variants. All of them were successfully expressed and isolated. The far-UV CD spectra recorded for each variant were indistinguishable from that of the unmodified $KatG^C$, suggesting that the modifications did not introduce catastrophic disruptions of protein structure (Fig. 4.3).

Table 4.2: Variants name corresponding to the detailed mutagenesis strategy

Variants name:	
HB1	M616G/R617H KatG^{C}
HB2	G614A/M616G/R617H KatG^{C}
HB1a	M616G/R617H Δ575-582 KatG^{C}
HB2a	G614A/M616G/R617H Δ575-582 KatG^{C}
PX1	A473H/G614A/M616G/R617H Δ575-582 KatG^{C}
PX2	S469R/A473H/G614A/M616G/R617H Δ575-582 KatG^{C}

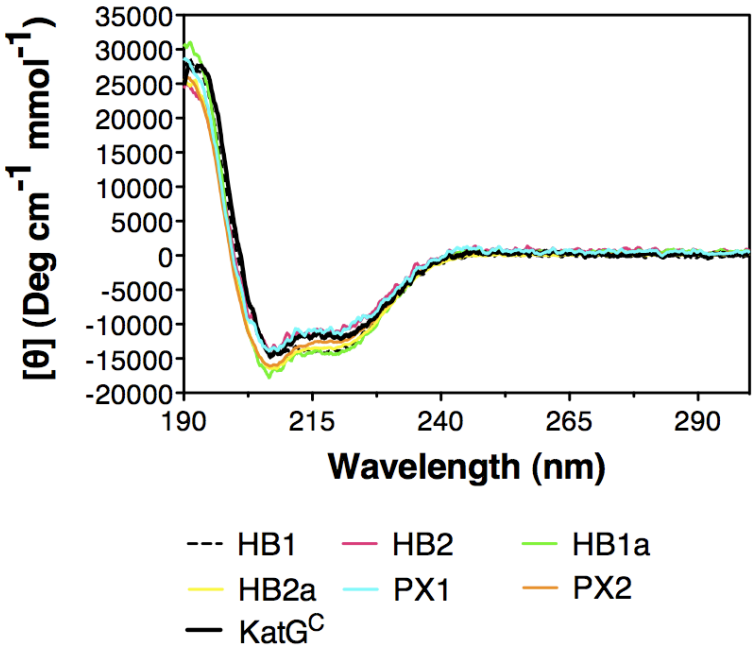

Figure 4.3: Far-UV circular dichroism of KatG^C and KatG^C variants.

Spectra were recorded at 23 °C in 5 mM phosphate buffer, pH 7.0 using a 0.5 mm quartz cell.

4.3.3 UV-vis spectroscopic properties of modified KatG^C:

As isolated, the stand-alone C-terminal domain ($KatG^C$) does not contain heme [143]. Consistent with this property, the spectrum of $KatG^C$ incubated with 0.75 eq. hemin showed typical features of free hemin with an absorption maximum near 380 nm. In contrast, the UV-visible absorption spectrum of HB1 showed a signature low-spin heme spectrum with a Soret band maximum near 415 nm and β and α band maxima at 538 nm and 558 nm, respectively. These features closely resembled those of the stand-alone KatG N-terminal domain of KatG ($KatG^N$). It indicated that heme binding was restored as a result of introducing proximal His ligand and that the bound heme was in a hexacoordinate, low-spin ferric state. However, HB1 showed a lower molar absorptivity than $KatG^N$ (Fig. 4.4 and Table 4.3). As described previously, construction of the HB1 variant resulted in three consecutive Gly residues. The greater conformational flexibility imparted by glycine residues is potentially problematic with respect to protein stability as it introduces a greater entropic tendency toward misfolded states. The variant we generated to minimize this problem, HB2, produced absorption spectra with similar maxima as those observed for HB1 but with enhanced molar absorptivity. The loop excision variants (HB1a and HB2a) showed a similar trend in spectra as that observed from their parent proteins HB1 and HB2 (Fig. 4.5). Finally, spectra recorded for the PX1 and PX2 variants were also dominated by hexacoordinate low-spin features. Of all the variants, overall, PX1 and PX2 spectra were most similar to those observed for $KatG^N$.

4.3.4 MCD spectroscopic properties of modified KatG^C:

In order to more effectively differentiate the high-spin and low-spin state contributions of

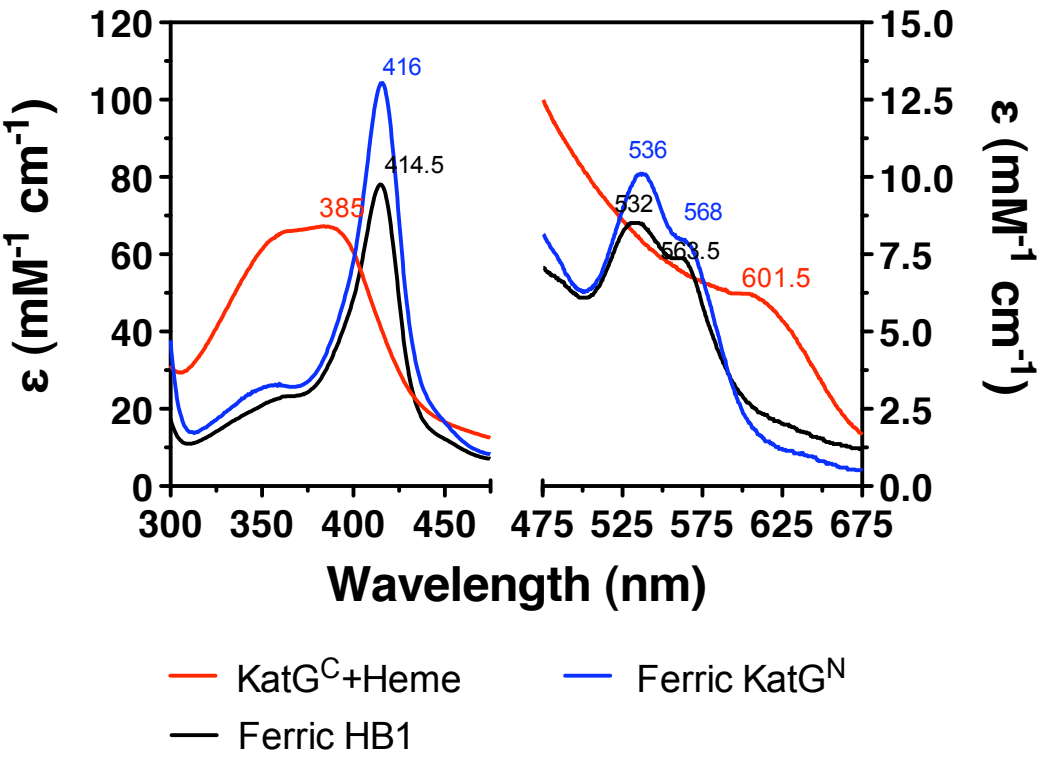

Figure 4.4: UV-vis spectra of ferric KatG^{C}, KatG^{N} and KatG^{C} variants (HB 1).

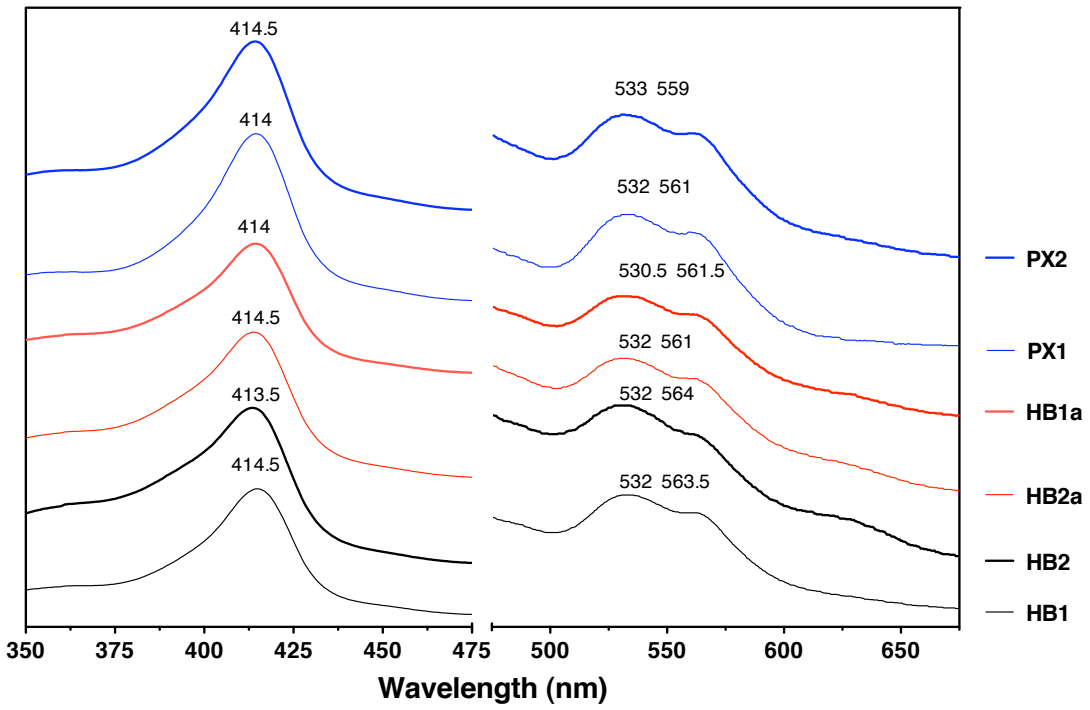

Figure 4.5: UV-vis spectra of ferric KatG^{C}, KatG^{N} and KatG^{C} variants.

Table 4.3: Absorption characteristics of $KatG^N$ and $KatG^C$ variants

Enzyme	**Absorption maxima [nm] (absorptivity [mM^{-1} cm^{-1}])**		
Ferric	Soret	β	α
$KatG^N$	416 (104.3)	536 (10.1)	568 (7.7)
HB 1	414.5 (77.8)	532(8.5)	563.5 (7.0)
HB 2	413.5 (98.9)	532 (11.7)	564 (9.8)
HB 1a	414 (81.6)	530.5 (9.4)	561.5 (8.2)
HB 2a	414.5 (91.5)	532 (10.1)	561 (8.8)
PX 1	414 (103.9)	532 (10.1)	561 (8.9)
PX 2	414.5 (101.8)	533 (9.6)	559 (8.5)

these variants, magnetic circular dichroism (MCD) spectra were recorded and analyzed. With the exception of HB1 and HB2 the ferric state of all the variants showed an intense derivative feature centered at 415 nm (Fig. 4.6B). This is typical of the hexacoordinate low-spin state. One interpretation for the less intense spectra for HB1 and HB2 would be that there is a much greater contribution from high spin species. MCD spectra recorded for the ferrous states of all the variants (Fig. 4.6A) consistently showed an intense A-term centered around 557 nm, indicative of substantial contribution from hexacoordinate low-spin heme species. In the ferrous state, high-spin heme produces an intense B-term with a maximum around 440 nm. This feature was particularly prominent for the HB2a and PX1 variants and less so for HB1 and HB2, indicating that the former pair of proteins were more favorable to high-spin heme states. Thus, while HB2a and PX1 do show a greater tendency toward heme ligation environments that give rise to high-spin heme iron, HB1 and HB2 do not. It would seem, then, in conjunction with UV-visible and ferrous MCD spectra, that the less intense features of the ferric MCD spectra of HB1 and HB2 are due to an inability of these variants to bind heme in a uniform environment. A greater proportion of adventitiously bound heme would be expected to contribute to broader and lower intensity spectra.

4.3.5 EPR spectroscopic properties of modified KatG^{C}:

A more definitive assessment of the heme-binding environment was carried out using EPR spectroscopy (Fig. 4.7). Consistent with the low molar ellipticity in their ferric MCD spectra, HB1 and HB2 showed only weak signals in the low-temperature EPR spectra. However, removal of the "active site" placeholder loop (i.e, HB1a and HB2a) produced a domain (and derivatives thereof) with more sharply defined EPR spectra. Similar to those observed for the stand-alone

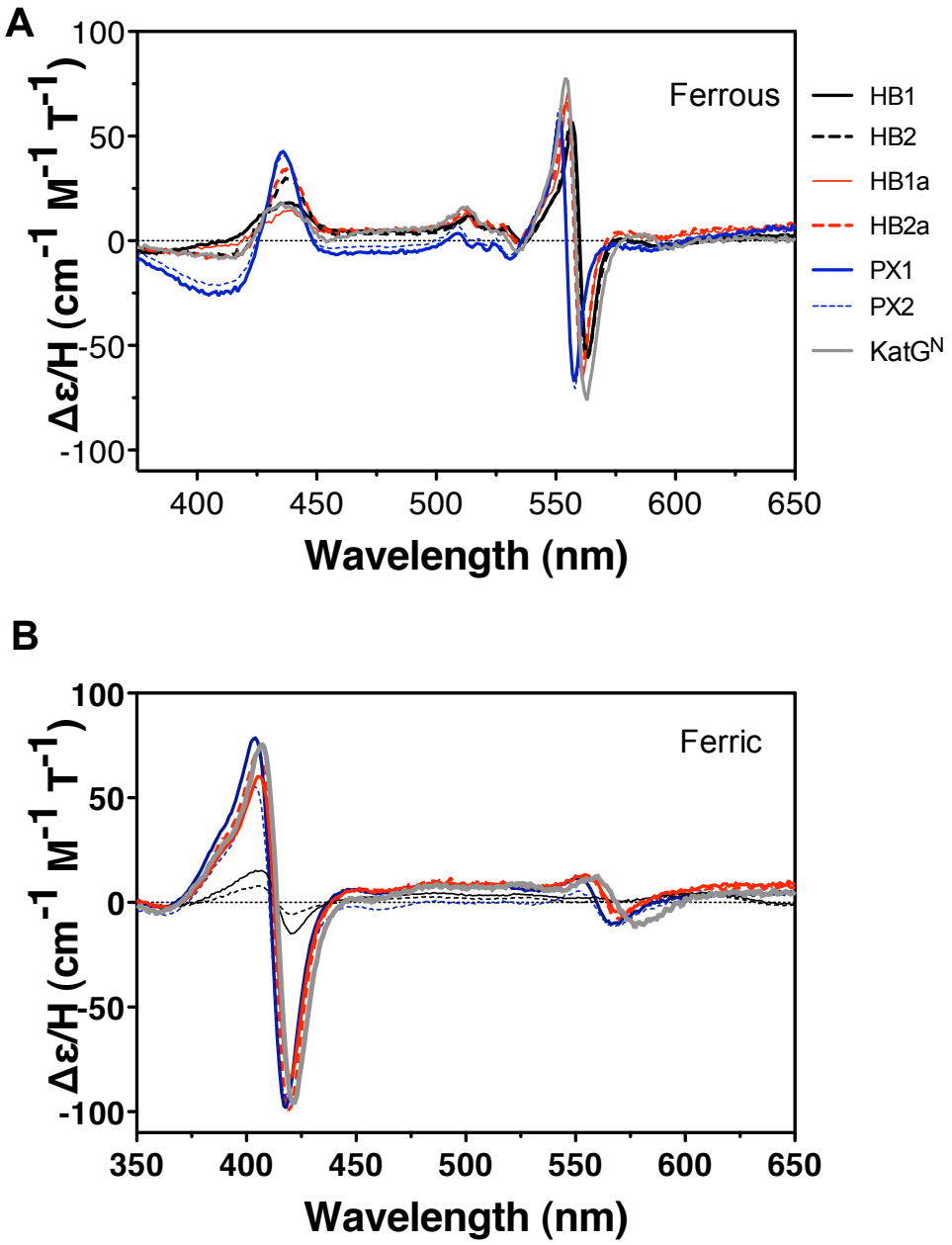

Figure 4.6: Magnetic circular dichroism (MCD) spectra for KatG^{C} and KatG^{N} variants.

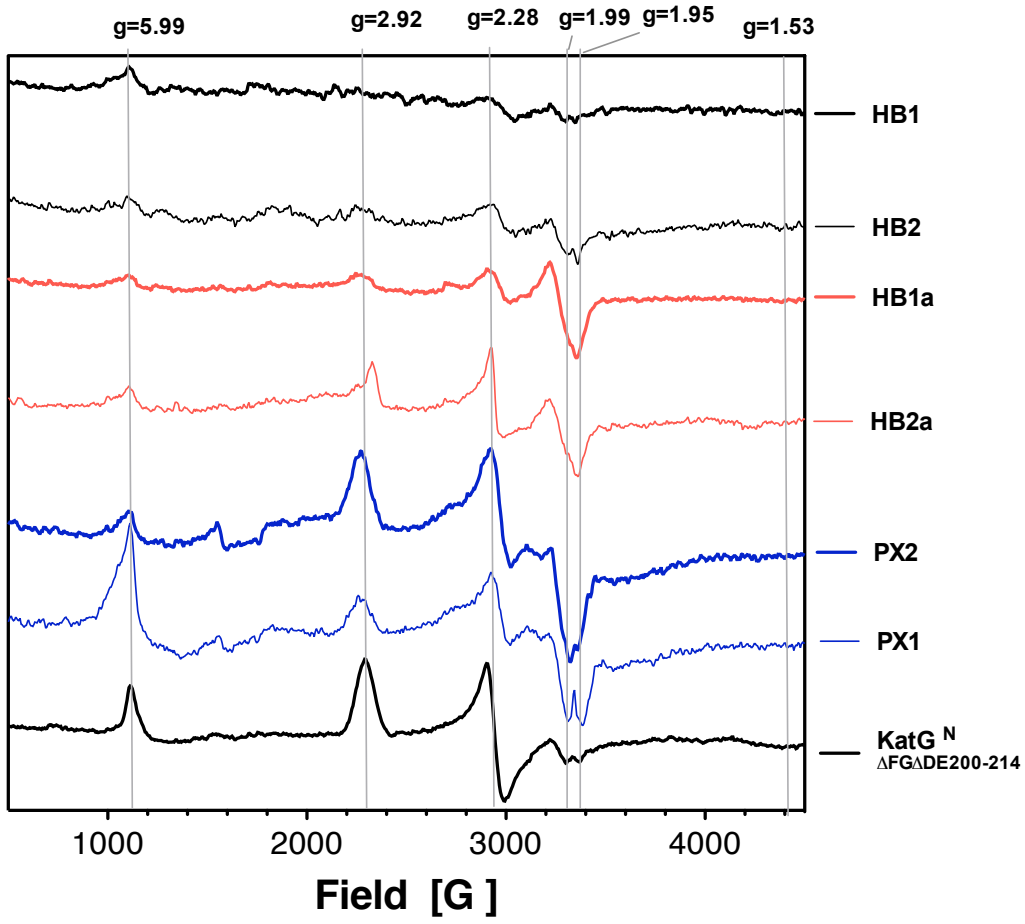

Figure 4.7: EPR spectra for ferric state of KatG^{C} and KatG^{N} variants.

N-terminal, the most prominent features were observed near g=2.92 and g=2.28, consistent with a hexacoordinate low-spin Fe (III) complex. Notably, for PX1, a much more pronounced feature was detected at g=5.99, indicating the presence of a greater proportion of a high-spin state. However, the EPR spectra of PX2, where Arg had been introduced as an electrostatic catalyst showed a diminished intensity in high-spin state along with increased intensity of signals corresponding to low-spin species (Fig. 4.7).

4.4.6 Steady-state kinetics of KatG^C:

To date, none of the modifications to KatG^C have produced an enzyme with catalase and peroxidase activities.

4.4 Discussion and conclusion:

Due to its sequential and structural resemblance to monofunctional peroxidases, the C-terminal domain retains the *general architecture* of a functional peroxidase active site. Indeed, the sequence alignments and the structures solved for KatG's indicate that the C-terminal domain retains an active site helical topology essentially identical to that observed in the N-terminal domain of KatG as well as other class I peroxidases. However, we speculate that side chain substitutions and other modifications accumulated since gene duplication and fusion have rendered the site unable to bind heme or have catalytic activity of its own.

We surmised that this set of circumstances presented the C-terminal domain as an ideal "blank slate" for generating new heme-dependent catalysts. Strategically, it seemed that a reintroduction of peroxidatic activity would be the most straightforward approach to evaluate this

hypothesis. Consistent with our hypothesis, dramatic improvement in heme binding was observed with the double substitution variant HB1 (i.e., M616G/R617H) where a steric impediment to occupancy of the active site by heme was eliminated and an appropriate ligand to the heme iron was introduced, respectively. However, the preponderance of spectral evidence (reduced molar absorptivity and reduced molar ellipticity in UV-vis and ferric MCD spectra, respectively, and the absence of clearly defined EPR spectral features) indicated a large diversity of heme association states. The data suggested a need for further modification to produce more uniformly bound heme.

Visual inspection of a crystal structure solved for the *E. coli* KatG C-terminal domain shows F579 and R580 located at the apex of a loop structure oriented toward the former active site [143]. In this, the structure is reminiscent of Large Loop 1 (LL1) found in the N-terminal domain. The phenylalanine at position 579 appears to be a hydrophobic placeholder for the now absent heme and the arginine at position 580 obstructs access to the active site. Both of these residues and the loop which bears them would be expected to limit appropriate heme binding in HB1 and HB2. Consistent with this hypothesis, excision of the loop (i.e., Δ575-582) in combination with M616G/R617H substitution produced proteins with more sharply defined spectral characteristics. In particular with HB2a, the EPR spectrum suggested a successful mimic of the stand-alone N-terminal domain.

For the native class I plant peroxidases, the distal His-Arg-Trp triad is strongly conserved and essential for peroxidative catalysis, especially for compound I formation [182-184, 25]. The distal histidine is employed as a general base/acid during catalysis [182-184]. As expected,

substitution of histidine with alanine substantially decreases the rate of compound I formation in cytochrome *c* peroxidase (CCP) [192]. The presence of Ala in the analogous position in $KatG^C$, HB1, HB2, HB1a, and HB2a would account for a lack of peroxidase activity in those proteins. In an attempt to introduce peroxidase catalytic ability, we replaced A473 with histidine in the HB2a variant to generate the PX1 protein; the protein with heme characteristics most similar to $KatG^N$. However, no apparent peroxidase activity was detected in PX1. In order to restore the peroxidatic activity, an arginine was introduced distal to the heme group by replacing S469 (i.e., PX2). Crystal structures of CCP have revealed that the distal arginine has "in" and "out" conformations, and only the "in" position allows the arginine side chain to form an H-bond with iron-linked oxygen [99]. Therefore, the arginine is proposed to stabilize the ferryl-oxo center in of compound I and presumably compound II.

However, these modifications do not appear to be sufficient to introduce peroxidatic activity, possibly attributed to both "active sites" in PX1 and PX2 having been shifted, allowing distal residues to directly coordinate the heme iron. As previously described (see Chapters 2 and 3), KatG without its C-terminal domain ($KatG^N$) is no longer expressed in a soluble form but is instead found in inclusion bodies. In addition, following denatured purification, refolding and reconstitution, $KatG^N$ shows a shifted active site structure, allowing what appears to be the direct coordination of the heme iron by the distal histidine [142]. This can be remedied by introducing the stand-alone C-terminal domain [144]. Interestingly, the stand-alone C-terminal domain is expressed in a soluble form and demonstrates substantial structural stability on its own. However, variants directed toward reintroduction of heme binding and catalytic activity were no longer expressed in a soluble form. Moreover, after denatured purification, refolding and

reconstitution, the "active site" heme environment appears to be highly similar to that of $KatG^N$, indicating our modifications successfully produced a mimic of $KatG^N$ where similar structural elements (i.e, an extra domain such as C-terminal domain in KatG or a helical structure such as I'-helix in KatG) may be necessary to stabilize the active site conformation and thereby modulate the catalytic ability. Therefore, future modification will focus on finding certain structural elements to direct the active site return of high-spin species, allowing the distal His to exert its function as a general base/acid [182-184].

In addition, the distal side arginine is critical and must be appropriately positioned to allow for the formation of compound I upon reaction with H_2O_2. In addition, Asp 681 and Asn 503 fulfill the function of active site His H-bond partners. However, our substitutions may not be ideally situated to reestablish these critical hydrogen bonded interactions. Therefore, additional modifications will also focus on reorienting and adjusting residues to optimize active site H-bonding to fully restore peroxidase activity.

Due to the sequence and structural similarity between the C-terminal domain of KatG and typical plant peroxidases, the most straightforward approach of engineering $KatG^C$ is reintroduction of peroxidatic activity by restructuring a typical plant peroxidase active site. In addition, $KatG^C$ also provides a practical starting point for engineering other heme-dependent enzymes. First, the existing structure and its "active site" framework could be exploited to engineer other types of peroxidases. For instance, a DyP-type peroxidase active site may be obtainable by introducing aspartate as an acid/base catalyst starting with the HB2a template. Likewise, Cys instead of His, can be introduced as the proximal heme-binding ligand; in the

distal site, Glu rather than His is used as catalytic acid/base to engineer $KatG^C$ into a fungal heme-dependent chloroperoxidase (see Chapter 1). Second, the KatG active site is highly versatile: catalase, peroxidase, dioxygenase, and peroxynitritase activities have all been observed [193, 194, 195]. The existing $KatG^C$ active site framework can be refined toward a particular reaction and set of substrates rather than building an entirely new activity from first principles.

CHAPTER FIVE

RAPID DIAGNOSIS OF MET-TYR-TRP COVALENT ADDUCT FORMATION IN KATG BY SDS-PAGE

5.1 Introduction:

Catalase-peroxidases (KatGs) are bifunctional enzymes, using a single active site to degrade H_2O_2 by either a catalase or peroxidase mechanism. All available crystal structures for intact KatG show two unique covalent bonds between three amino acid side chains, W105, Y226, and M252 (*E. coli* numbering). This adduct is located on the distal side of the heme (Fig. 5.1) [119-121, 131], where it appears to be indispensable for the unique catalase activity of KatG [132, 134, 135, 149, 196-198]. The formation of this covalent adduct is proposed to be autocatalytic wherein a peroxide oxidizes the KatG heme to a compound I (i.e. Fe^{IV}=O [porphyrin$^{\cdot+}$]) species, which then oxidizes the Trp and Tyr residues leading to establishment of the adduct by radical-radical coupling [135].

In addition to crystal structures for various KatGs, the M-Y-W adduct has also been observed in the enzyme in solution by LC/MS/MS peptide mapping techniques [132-135]. Evaluation of this adduct by mass spectrometric approaches requires a relatively large amount of protein, long analysis time, and expensive instrumentation.

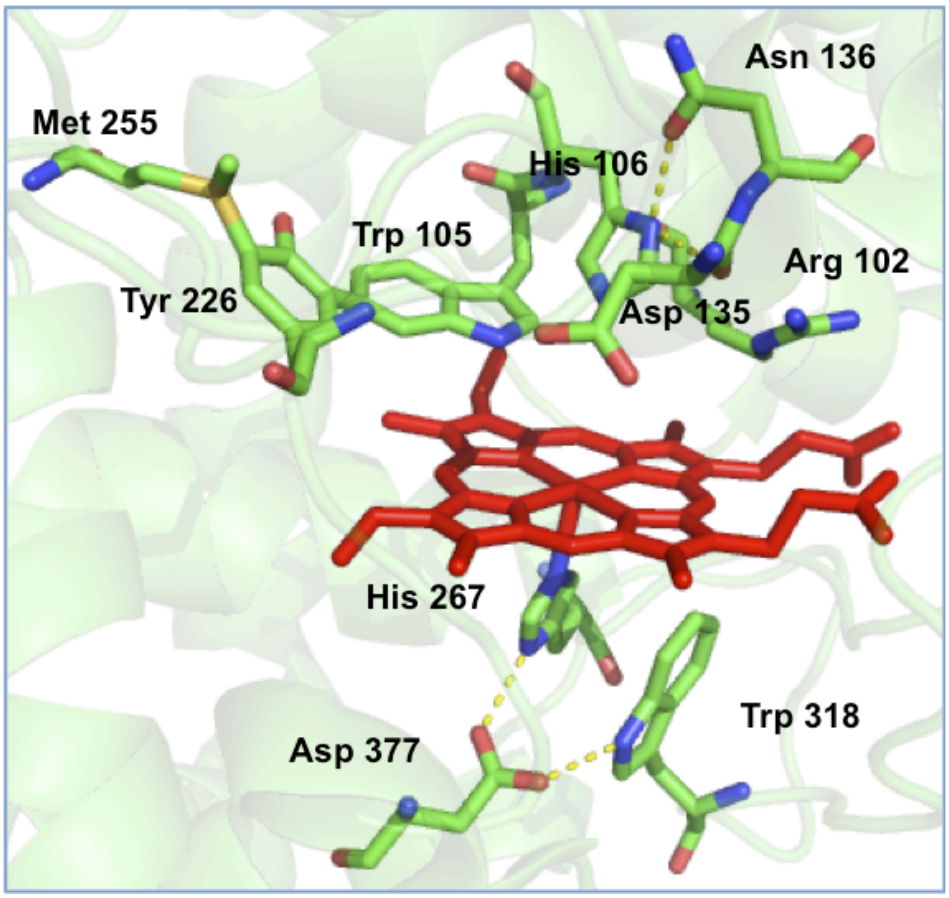

Figure 5.1: Distal active site M-Y-W covalent adduct in KatG from *M. tuberculosis* (PDB: 1SJ2).

It has been reported that SDS-PAGE separation of recombinant KatP (a periplasmic catalase–peroxidase from *Escherichia coli* O157:H7) resulted in two forms of the protein [153]. Each band was determined to be a single protein, and each one was identified as KatP by HPLC as well as peptide sequence analysis. The presence of heme and catalase activity was only observed in the protein with lower apparent molecular weight [153]. Similarly, two forms of protein have been observed by SDS-PAGE in our laboratory with our reconstituted wild-type KatG (*E.coli* K-12). A reasonable explanation for these observations is that these post-translational covalent bonds are established within a subunit and not subject to disruption by SDS or thiol-based reductants. In theory then, KatG bearing the covalent adduct should be prohibited from completely denaturing in the presence of SDS, and as a result, should have a lower hydrodynamic volume, and more rapid migration through the acrylamide matrix than KatG lacking this novel covalent structure.

5.2 Methods:

Expression and purification of wtKatG and ΔLL2 variants [151] as well as $KatG^C$ and $KatG^N$ were carried out as previously described [142, 144]. Likewise, expression and purification of Δ200-214, Δ209-228 and Y226F followed procedures that we have recently described [136]. The reconstituted protein solutions were allowed to incubate for at least 24 h at 4 °C. These solutions were then centrifuged to remove insoluble unincorporated heme and other debris. Solutions containing 1:1 ratios of $KatG^N$ and $KatG^C$ were incubated for 24 hours in the presence of 50 mM phosphate buffer, pH 7.0, 50 mM NaCl at 4 °C as previously described in Chapter 2 and 3.

For analyses by SDS-PAGE, a 7.6% acrylamide resolving gel and 4% acrylamide stacking gel were used. Protein samples (0.015 nmol) were loaded and separated. In order to avoid peracetic acid (PAA)-induced protein aggregation, protein samples were mixed with SDS loading buffer immediately after treatment with 2 equivalents of PAA.

5.3 Results:

It has been shown that the M-Y-W covalent adduct is essential for the catalase activity of KatG, and its formation in KatG is heme-dependent. *E. coli* KatG expressed in a T7-based system produces the enzyme predominantly (~95%) in its apoprotein form [151]. Apo-KatG can be reconstituted with heme to produce an enzyme with full catalase and peroxidase activities [151]. As such, this establishes a system by which to evaluate covalent adduct formation by SDS-PAGE. Without added heme, a single band (~80 kD) is observed by SDS-PAGE (Fig. 5.2A). Reconstitution of KatG with hemin resulted in the appearance of a second band with a lower apparent molecular weight, and the relative intensity of this band increased with an increasing amount of heme added up to 1 molar equivalent. Above 1 equivalent, no further increases in the intensity of the lower band were observed [199] (Fig. 5.2A).

Reconstitution of KatG with redox-inactive Zn-protoporphyrin IX prevented the appearance of the lower band as one would anticipate given the oxidative chemistry necessary to establish the M-Y-W adduct. It has been shown previously that full establishment of the adduct requires hydroperoxide. Accordingly, hemin-reconstituted KatG treated with two equivalents of PAA migrated almost entirely as the lower apparent molecular weight band. Conversely, KatG reconstituted with Zn-protoporphyrin IX and then reacted with 2 equivalents of PAA showed no

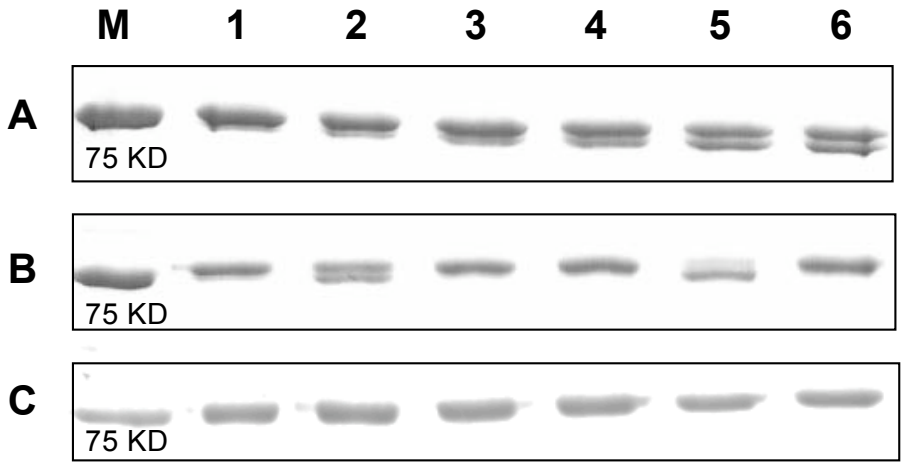

Figure 5.2: Evaluation of M-Y-W covalent adduct formation by SDS-PAGE [199].

(A) Denaturing electrophoretic separation of apo-KatG (lane 1) was reconstituted with 0.3 equivalents (lane 2), 0.6 equivalents (lane 3), 1.0 equivalent (lane 4), 2.0 equivalents (lane 5) and 5.0 equivalents (lane 6) of heme. Marker (M) was shown as 75 KD. (B) Effect of heme and peroxide on migration of apo-KatG. Apo-KatG (lane 1) with heme (lanes 2 and 5), Zn-PPIX (lanes 3 and 6), and 2 equivalents of PAA (lanes 4-6) added. (C) Effect of substituting Y226 on the protein migration. Apo-Y226F (lane 1) with heme (lanes 2 and 5), Zn-PPIX (lanes 3 and 6), and 2 equivalents of PAA (lanes 4-6) added.

shift in SDS-PAGE migration compared to the untreated Zn-protein or apo-KatG [199] (Fig. 5.2B). Substitution of the critical tyrosine (Y226 in *E. coli* KatG) with phenylalanine prevents formation of the covalent adduct and eliminates catalase activity [128, 136]. With Y226F KatG only the higher apparent molecular weight band was observed regardless of reconstitution (with hemin or Zn-protoporphyrin IX) or treatment with PAA [199] (Fig. 5.3C).

We have applied this SDS-PAGE based technique to other KatG variants designed to target various aspects of structure and function. For example, the strictly conserved Tyr residue (Y226) is contained within the KatG-unique structure Large Loop 1 (LL1). In order to evaluate the role of the larger LL1 structure in KatG function, we have generated two deletion variants (Δ200-214 and Δ209-228) [136]; the latter (Δ209-228) lacks Y226, while the former does not.

Analyses by SDS-PAGE gel showed the presence of two bands for Δ200-214, but only one for Δ 209-228. Accounting for the difference in molecular weight caused by the deletion, Δ200-214 showed an increased proportion of protein migrating as the lower molecular weight band following treatment with two equivalents of PAA, consistent with the wild-type enzyme. Accounting for the decreased molecular weight caused by the deletion, Δ209-228 showed behavior analogous to that of Y226F KatG (Fig. 5.3A).

Large Loop 2 (LL 2) is another structure unique to KatG. It has been shown to be essential for the catalase activity of KatGs. Indeed, deletion of LL2 or portions thereof produces proteins with a 99.8% decrease in catalase activity [151, 130]. In these variants, the mechanistic explanation for the loss of catalase activity is less obvious. The LL2 structure does not contain

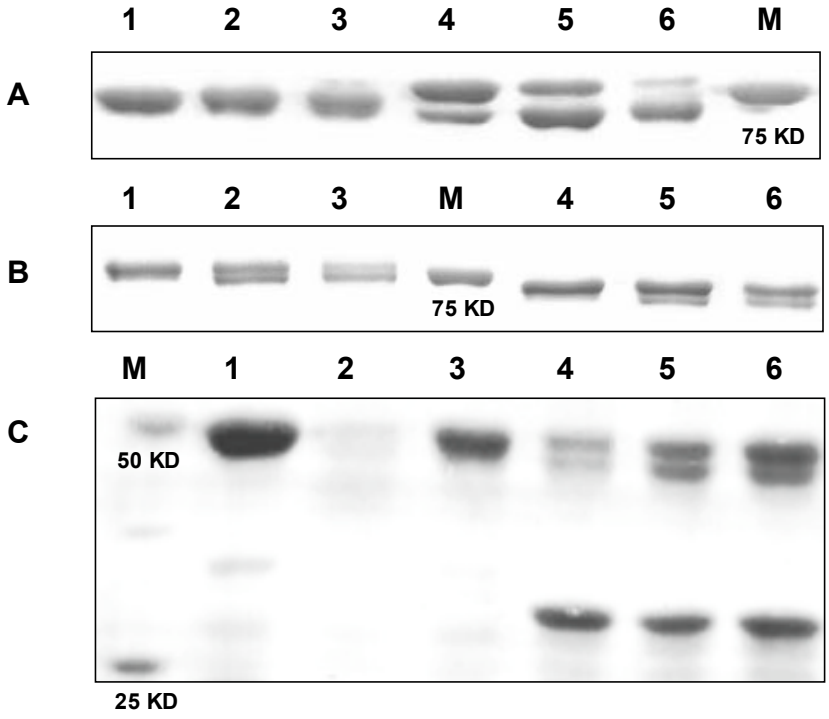

Figure 5.3: The influence of peripheral structures on the formation of M-Y-W adduct.

(A) SDS-PAGE separation of Δ209-228 and Δ200-214 prior to reconstitution with heme (lane 1 and 4, respectively) following reconstitution with 1 equivalent of heme (lanes 2 and 5, respectively), and treatment of reconstituted Δ209-228 and Δ200-214 with 2 equivalents of PAA (lanes 3 and 6, respectively). (B) Effect of deletion of LL2 on formation of covalent adduct. Apo-wtKatG and apo-ΔLL2 (lanes 1 and 4, respectively) following reconstitution with heme (lanes 2 and 5, respectively) and treatment with 2 equivalents of PAA (lanes 3 and 6, respectively). (C) Effect of removal and reintroduction of the C-terminal domain on the formation of MYW covalent adduct. Lanes 1-3 showed $KatG^N$ reconstituted with heme (lane 1), in presence of 200 equivalents of H_2O_2 (lane 2) or in presence of 2 equivalents of PAA (lane 3). Lanes 4-6 showed the domain mixture ($KatG^N$+$KatG^C$) reconstituted with heme (lane 6), in presence of 200 equivalents of H_2O_2 (lane 5) or in presence of 2 equivalents of PAA (lane 4).

any of the amino acids of the M-Y-W adduct. As such, the loss of catalase activity might be due to a failure to establish this adduct or due to some other mechanisms. Here, a straightforward analysis of covalent adduct formation by SDS-PAGE helps to deconvolute the role(s) of a structure like LL2. We took the KatG deletion variant lacking the entire LL2 structure (KatG [ΔLL2]). Reconstitution of this protein with 1 equivalent of heme and subsequent exposure of reconstituted enzyme to 2 equivalents of PAA produced a similar SDS-PAGE migration shift as those observed for wild-type KatG (Fig. 5.3B). Independent evaluation of covalent adduct formation by MS techniques verified the presence of the covalent adduct by peptide mapping in KatG (ΔLL2) [130].

As described elsewhere, the C-terminal domain of KatG likely originated from a gene duplication and fusion event, and this structure is located 30 Å away from the active site [118]. From this position it appears to serve as a platform to direct active site structural adjustment (see Chapters 2 and 3). Deletion of the C-terminal domain produces a protein ($KatG^N$) in which the structure of the active site has shifted, allowing what appears to be the direct coordination of the heme iron by the distal histidine [142].

The expression of $KatG^N$ in inclusion bodies, its purification under denaturing conditions, reconstitution with hemin following purification, and lack of catalase activity following reconstitution would suggest that the covalent adduct is not formed in this protein. However, $KatG^N$ incubation with the stand-alone C-terminal domain ($KatG^C$) does result in the reemergence of catalase activity, suggesting that the covalent adduct is formed at least to some extent when $KatG^N$ and $KatG^C$ are incubated together. Here again, SDS-PAGE provides a

straightforward way to qualitatively assess this hypothesis. Analyses of $KatG^N$ migration by SDS-PAGE showed a single band for the protein even following reconstitution with hemin *and* exposure to PAA, indicating that without the C-terminal domain, $KatG^N$ was incapable of establishing the M-Y-W adduct (Fig. 5.3C). Interestingly, incubation of $KatG^N$ with 200 molar equivalents of H_2O_2 resulted in the loss of protein at the expected molecular weight. Due to its inability to consume H_2O_2 by either catalatic or peroxidatic turnover, excess H_2O_2 appears to result in extensive oxidation of the protein as well as subsequent aggregation (Fig. 5.3C). In contrast, our SDS-PAGE analyses indicated that incubation of $KatG^N$ with equimolar $KatG^C$ did allow for the formation of M-Y-W adduct (Fig. 5.3C). Furthermore, the introduction of $KatG^C$ clearly enhanced the ability of $KatG^N$ to metabolize large quantities of H_2O_2, consistent with an enzyme that has substantial catalase activity.

5.4 Conclusions:

SDS-PAGE is universally applied in biochemical research to separate proteins based upon their subunit molecular weight. Interestingly, as all residues contributing to the M-Y-W adduct are found within the same subunit, KatG bearing the covalent adduct should 1) be prohibited from completely denaturing in the presence of SDS, 2) have a lower hydrodynamic volume, and therefore, 3) migrate more rapidly through the acrylamide matrix than KatG lacking this novel covalent structure. For KatGs, this migration shift was easy to identify using SDS-PAGE. Compared to LC/MS/MS approaches, SDS-PAGE is more rapid and easily executed. Less sample is required, and it is less time and material intensive to quickly and qualitatively evaluate the influence of a range of conditions on formation of the adduct. Therefore, it can be used as a complementary procedure to more intensive LC/MS/MS procedures. By this fast diagnosis, we

observed the formation of this adduct in KatG required a redox active protoporphyrin and was aided by the addition of an oxidant like peracetic acid. In addition, we demonstrated that the technique was useful for evaluating variants like KatG (ΔLL2) where the mechanistic explanation for the loss of catalase activity is unclear. Likewise, the technique is useful for making a determination regarding the timing for M-Y-W adduct formation in a protein like $KatG^{N}$ which only gains catalatic activity in the presence of a partner protein, $KatG^{C}$. In conclusion, we suggest that this technique is not only useful for evaluating KatG, but also for other proteins where the establishment of novel post-translational covalent adducts leads to enzyme activation or inactivation.

CHAPTER SIX

SUMMARY

Catalases and peroxidases scavenge H_2O_2, the most abundant of the reactive oxygen species. By direct and indirect mechanisms, H_2O_2 is able to inflict damage on most cellular components, and it is generated as an inevitable consequence of aerobic metabolism. As a result, catalases and peroxidases are essential protective enzymes found in all aerobic organisms. Interestingly, copious production of H_2O_2 forms a critical component of the inflammatory responses of higher eukaryotes against infection by pathogenic organisms. For these pathogens, defenses against the accumulation of H_2O_2 are particularly important for their survival within the host organism.

Heme-dependent catalases are able to rapidly and efficiently disproportionate H_2O_2, generating H_2O and O_2 as relatively harmless products. These enzymes do so with impressive second order rate constants ranging from 10^6 to 10^7 $M^{-1}s^{-1}$. In contrast to the catalases, heme-dependent peroxidases degrade H_2O_2 at the expense of exogenous reducing substrates (i.e., electron donors) whose oxidation products often have other important physiological functions. Therefore, peroxidases have a variety of essential but organism/cell-specific physiological roles in addition to reducing oxidative stress. Catalase-peroxidase (KatG) are unique in nature in that they are capable of degrading H_2O_2 via peroxidase ***and*** catalase activity, both of which are at levels comparable to those monofunctional counterparts. KatG is found exclusively in

prokaryotic and lower eukaryotic organisms where it serves as an essential component of the oxidative stress response.

The structure of a heme-dependent protein and its connection to functionality can be evaluated at four levels: 1) the structure of the heme prosthetic group itself, 2) the heme environment as dictated by protein-derived ligand(s), 3) the immediate heme environment as dictated by protein-derived groups other than the ligands, and 4) protein features peripheral to, and in some cases, distant from the active site. The research described in this dissertation tackles the structure-function equation on all of these levels. Certainly, the most convoluted and most difficult to address is level four. KatGs have a novel two-domain structure. Neither domain bears any resemblance to monofunctional catalases but both domains strongly resemble the overall fold monofunctional peroxidases. In fact, the N-terminal domain has an active site that is virtually indistinguishable from those of monofunctional peroxidases. Given the high similarity of KatG and monofunctional peroxidase in terms of heme structure, iron coordination and protein-derived heme environment, it is reasonable to suggest the protein structures/features external to the KatG active site are essential for imparting the hallmark bifunctional catalytic abilities of the enzyme. Therefore, KatG provides an excellent opening to evaluate the contributions of distant protein structure to active site structure and function.

Comparisons of the protein structures and amino acid sequences of KatGs versus monofunctional peroxidases reveal three structural features unique to KatG: two interhelical insertions (LL1 and LL2) and a C-terminal domain. The Goodwin laboratory has shown that all of these structures have a profound influence on the function of KatG, but the mechanism by

which this distant control is exerted is still poorly understood, particularly, the C-terminal domain. The crystal structure of the stand-alone C-terminal domain reveals that the features of easy folding, protease-resistance, the conserved residues pattern involved in inter- and intra-subunit interactions make the C-terminal domain has the appearance of a platform to direct the proper folding of the N-terminal domain.

1: The integral role of I'-helix in the function of C-terminal domain:

I'-helix appears at the interface between the two domains. It makes contacts with several elements from the N-terminal domain of the adjacent subunit using strongly conserved Leu 690, Arg 691, Glu 695, and Tyr 697. As such, it has all the appearances of a platform by which the C-terminal domain may direct structural adjustments to the N-terminal domain and modulate active site conformation. Our data showed multiple substitutions of I'-helix substantially increased the propensity of KatG to form the hexacoordinate low-spin state as well as clear compromises to active site and overall protein structural stability. Indeed, the quadruple variant showed properties nearly identical to $KatG^N$ in all respects even though it retained what appeared to be a correctly folded C-terminal domain.

Another important outcome of the work is that it showed the separated domains as an advantageous tool to address these distant interactions. We have capitalized on the unique ability of $KatG^C$ to reactivate an otherwise inactive $KatG^N$ in order to show that the C-terminal domain's I′-helix is a central component of a platform to facilitate folding events and/or conformational adjustments in the N-terminal domain. Indeed, our data indicate that even single substitutions to the I′-helix substantially limit the ability of $KatG^C$ in this respect. With two substitutions to the

I′-helix, $KatG^C$ became completely incapable of directing the restructuring of $KatG^N$ for reactivation. Taken together, we demonstrated that the C-terminal domain I' helix is essential to direct structural adjustments in the adjacent N-terminal domain.

2: Distant interactions connecting the remote I'-helix to active site conformation, stability and catalytic function:

Though we established the I'-helix as an important structure for conformational control of the active site, how this effect is communicated to the active site remaines to be determined. We noted some important interactions with E695, a residue that seemed particularly important to the function of the I'-helix. Using a similar approach we observed that interactions of E695 with two other residues, R126 and W159 were also important. Most strikingly, we found that disruption of these interactions in the intact protein had little effect on the stability of the global structure of the protein but a profound impact on the stability of the active site. Even the subtle modification represented in the E695Q substitution was sufficient to substantially destabilize the enzyme active site. Here again, the behavior of the separately expressed and isolated domains indicated that these residues are essential for C-terminal domain-dependent control of the N-terminal domain active site.

The primary significance of this work is that it reveals a structural basis for a connection via remote interactions to active site conformation. Well-ordered water molecules from the domain interface to the active site appear to stabilize the BC loop, which further adjust the B-helix bearing distal His. The importance of this structure is apparent from the attention it receives in terms of increasing its stability in enzymes related to KatG. In Class II (e.g. manganese

peroxidase) and III peroxidases, which depend on Ca^{2+} to maintain the heme coordination environment that supports activity, the relevant calcium-binding site is established in part by this same portion of the BC loop. The roles of these polar contacts may resemble that of Ca^{2+} in class II peroxidases, providing a possible explanation for the evolutionary persistence of the C-terminal domain dedicated to stabilizing the catalytic active domains, adapted to the variable environment.

3： Borrowing the C-terminal domain as a scaffold for engineering a new heme-dependent catalyst:

The work described here also has special bearing on levels two and three of heme protein structure and function. In particular, principles understood from investigations of other heme protein structures were applied toward engineering new heme-based catalysts. KatGs have a novel two-domain structure, which appears to be the result of a gene duplication and fusion event. Taking advantage of this evolutionary history, we borrow the "peroxidase-like" C-terminal domain as a scaffold to engineer a new heme-dependent catalyst, and in particular, restore its peroxidative ability. A pathway toward restored peroxidase activity and enzymes with alternative catalytic abilities has been laid. With new proteins competent for association with the cofactor, directed evolutionary approaches can now be employed in which the target activity serves as the basis for selection of variants from one round of mutagenesis to the next.

4：Diagnosis of the M-Y-W covalent adduct in KatG by SDS-PAGE:

This dissertation describes a novel technique to monitor an important component of KatG structure (M-Y-W covalent adduct). As we demonstrated, formation of this M-Y-W in the KatG

adduct required the redox-active porphyrin as the prosthetic group in the presence of oxidant. This technique is sensitive to the identity of the cofactor and rightly identifies substitutions and deletions that prevent formation of the adduct. Most importantly, for this dissertation, the technique demonstrates that part of the active site conformational control exerted by the C-terminal domain is that which is required to establish the critical M-Y-W adduct.

KatG is a conundrum of protein structure and function. It has a robust catalase activity that is only observed in a class of enzymes to which it has no relation, and its closest relatives which share essentially identical active sites have virtually no capacity as catalases. In this regard, KatG does possess several novel protein structural components that are to one extent or another peripheral to the active site. This points to a clear model for evaluating how external structures exert control over active site conformation and catalytic ability. Among the novel structural features of KatG, the C-terminal domain was the first to be recognized. It has the clearest evolutionary origin. It is by far the largest and is situated the greatest distance from the active site. It is also the KatG structure about which the least is understood. Prior to the initiation of the research described in this dissertation, it was known that the C-terminal domain was indispensible to the function of KatG, and it showed a very specific impact on the KatG active site some 30 Å away. Works described in this dissertation first identify the critical structural component (I'-helix) in the C-terminal domain as a platform and discover the mechanism(s) by which the C-terminal domain communicates with and controls the active site. These findings contribute to answering fundamental questions of enzyme structure and function with clues to how new functions emerge in nature through evolutionary processes. These studies also point toward ways that new heme enzymes may be generated and improves our understanding of the

structure of a protein underneath antibiotic resistance in *Mycobacterium tuberculosis* and enhanced virulence of pathogenic organisms.

REFERENCES

[1] L.C. Seaver, J.A. Imlay, Are respiratory enzymes the primary sources of intracellular hydrogen peroxide?, J Biol Chem 279 (2004) 48742-48750.

[2] S. Mishra, J. Imlay, Why do bacteria use so many enzymes to scavenge hydrogen peroxide?, Arch Biochem Biophys 525 (2012) 145-160.

[3] S. Jang, J.A. Imlay, Micromolar intracellular hydrogen peroxide disrupts metabolism by damaging iron-sulfur enzymes, J Biol Chem 282 (2007) 929-937.

[4] J.M. Sobota, J.A. Imlay, Iron enzyme ribulose-5-phosphate 3-epimerase in Escherichia coli is rapidly damaged by hydrogen peroxide but can be protected by manganese, P Natl Acad Sci USA 108 (2011) 5402-5407.

[5] M. Zamocky, P.G. Furtmuller, C. Obinger, Evolution of catalases from bacteria to humans, Antioxid Redox Signal 10 (2008) 1527-1547.

[6] M. Zamocky, B. Gasselhuber, P.G. Furtmuller, C. Obinger, Molecular evolution of hydrogen peroxide degrading enzymes, Arch Biochem Biophys 525 (2012) 131-144.

[7] J. Bravo, M.J. Mate, T. Schneider, J. Switala, K. Wilson, P.C. Loewen, I. Fita, Structure of catalase HPII from Escherichia coli at 1.9 A resolution, Proteins 34 (1999) 155-166.

[8] M.S. Sevinc, J. Switala, J. Bravo, I. Fita, P.C. Loewen, Truncation and heme pocket mutations reduce production of functional catalase HPII in Escherichia coli, Protein Eng 11 (1998) 549-555.

[9] I. Fita, M.G. Rossmann, The active center of catalase, J Mol Biol 185 (1985) 21-37.

[10] J. Bravo, N. Verdaguer, J. Tormo, C. Betzel, J. Switala, P.C. Loewen, I. Fita, Crystal structure of catalase HPII from Escherichia coli, Structure 3 (1995) 491-502.

[11] S.P. de Visser, What external perturbations influence the electronic properties of catalase compound I?, Inorg Chem 45 (2006) 9551-9557.

[12] J. Bravo, I. Fita, J.C. Ferrer, W. Ens, A. Hillar, J. Switala, P.C. Loewen, Identification of a novel bond between a histidine and the essential tyrosine in catalase HPII of Escherichia coli, Protein Sci 6 (1997) 1016-1023.

[13] S.G. Kalko, J.L. Gelpi, I. Fita, M. Orozco, Theoretical study of the mechanisms of substrate recognition by catalase, J Am Chem Soc 123 (2001) 9665-9672.

[14] P, Nichols, I, Fita, P.C. Lowen. Enzymology and structure of catalases. In Advances in Inorganic Chemistry, Sykes, Academic Press, New York, 2001

[15] M. Alfonso-Prieto, X. Biarnes, P. Vidossich, C. Rovira, The molecular mechanism of the catalase reaction, J Am Chem Soc 131 (2009) 11751-11761.

[16] S. Kato, T. Ueno, S. Fukuzumi, Y. Watanabe, Catalase reaction by myoglobin mutants and native catalase: mechanistic investigation by kinetic isotope effect, J Biol Chem 279 (2004) 52376-52381.

[17] J.T. Groves, G.A. McClusky, Aliphatic hydroxylation by highly purified liver microsomal cytochrome P-450. Evidence for a carbon radical intermediate, Biochem Biophys Res Commun 81 (1978) 154-160.

[18] M. Zamocky, C. Jakopitsch, P.G. Furtmuller, C. Dunand, C. Obinger, The peroxidase-cyclooxygenase superfamily: Reconstructed evolution of critical enzymes of the innate immune system, Proteins 72 (2008) 589-605.

[19] F. Passardi, N. Bakalovic, F.K. Teixeira, M. Margis-Pinheiro, C. Penel, C. Dunand, Prokaryotic origins of the non-animal peroxidase superfamily and organelle-mediated transmission to eukaryotes, Genomics 89 (2007) 567-579.

[20] D. Koua, L. Cerutti, L. Falquet, C.J.A. Sigrist, G. Theiler, N. Hulo, C. Dunand, PeroxiBase: a database with new tools for peroxidase family classification, Nucleic Acids Res 37 (2009) D261-D266.

[21] E. Torres, M. Ayala, Biocatalysis based on heme peroxidases, Chapter 2, Molecular Phylogeny of heme peroxidases, Page 7-36, 2010, Springer, New York

[22] N. Ellfolk, R. Soininen, Pseudomonas cytochrome c peroxidase. I. Purification procedure, Acta Chem Scand 24 (1970) 2126-2136.

[23] A. Echalier, T. Brittain, J. Wright, S. Boycheva, G.B. Mortuza, V. Fulop, N.J. Watmough, Redox-linked structural changes associated with the formation of a catalytically competent form of the diheme cytochrome c peroxidase from Pseudomonas aeruginosa, Biochemistry-Us 47 (2008) 1947-1956.

[24] A. Echalier, C.F. Goodhew, G.W. Pettigrew, V. Fulop, Activation and catalysis of the di-heme cytochrome c peroxidase from Paracoccus pantotrophus, Structure 14 (2006) 107-117.

[25] N. Ellfolk, M. Ronnberg, R. Aasa, L.E. Andreasson, T. Vanngard, Properties and function of the two hemes in Pseudomonas cytochrome c peroxidase, Biochim Biophys Acta 743 (1983) 23-30.

[26] R. Gilmour, C.F. Goodhew, G.W. Pettigrew, S. Prazeres, I. Moura, J.J. Moura, Spectroscopic characterization of cytochrome c peroxidase from Paracoccus denitrificans, Biochem J 294 (Pt 3) (1993) 745-752.

[27] V. Fulop, C.J. Ridout, C. Greenwood, J. Hajdu, Crystal structure of the di-haem cytochrome c peroxidase from Pseudomonas aeruginosa, Structure 3 (1995) 1225-1233.

[28] L. De Smet, S.N. Savvides, E. Van Horen, G. Pettigrew, J.J. Van Beeumen, Structural and mutagenesis studies on the cytochrome c peroxidase from Rhodobacter capsulatus provide new insights into structure-function relationships of bacterial di-heme peroxidases, J Biol Chem 281 (2006) 4371-4379.

[29] M. Hoffmann, J. Seidel, O. Einsle, CcpA from Geobacter sulfurreducens Is a Basic Di-Heme Cytochrome c Peroxidase, J Mol Biol 393 (2009) 951-965.

[30] H. Shimizu, D.J. Schuller, W.N. Lanzilotta, M. Sundaramoorthy, D.M. Arciero, A.B. Hooper, T.L. Poulos, Crystal structure of Nitrosomonas europaea cytochrome c peroxidase and the structural basis for ligand switching in bacterial di-heme peroxidases, Biochemistry-Us 40 (2001) 13483-13490.

[31] J.M. Dias, T. Alves, C. Bonifacio, A.S. Pereira, J. Trincao, D. Bourgeois, I. Moura, M.J. Romao, Structural basis for the mechanism of Ca(2+) activation of the di-heme cytochrome c peroxidase from Pseudomonas nautica 617, Structure 12 (2004) 961-973.

[32] G.W. Pettigrew, A. Echalier, S.R. Pauleta, Structure and mechanism in the bacterial dihaem cytochrome c peroxidases, J Inorg Biochem 100 (2006) 551-567.

[33] R. Gilmour, C.F. Goodhew, G.W. Pettigrew, S. Prazeres, J.J. Moura, I. Moura, The kinetics of the oxidation of cytochrome c by Paracoccus cytochrome c peroxidase, Biochem J 300 (Pt 3) (1994) 907-914.

[34] T. Sato, S. Hara, T. Matsui, G. Sazaki, S. Saijo, T. Ganbe, N. Tanaka, Y. Sugano, M. Shoda, A unique dye-decolorizing peroxidase, DyP, from Thanatephorus cucumeris Dec

1: heterologous expression, crystallization and preliminary X-ray analysis, Acta Crystallogr D Biol Crystallogr 60 (2004) 149-152.

[35] Y. Sugano, R. Muramatsu, A. Ichiyanagi, T. Sato, M. Shoda, DyP, a unique dye-decolorizing peroxidase, represents a novel heme peroxidase family: ASP171 replaces the distal histidine of classical peroxidases, J Biol Chem 282 (2007) 36652-36658.

[36] H.J. Ogola, N. Hashimoto, S. Miyabe, H. Ashida, T. Ishikawa, H. Shibata, Y. Sawa, Enhancement of hydrogen peroxide stability of a novel Anabaena sp. DyP-type peroxidase by site-directed mutagenesis of methionine residues, Appl Microbiol Biotechnol 87 (2010) 1727-1736.

[37] Y. Sugano, Y. Matsushima, K. Tsuchiya, H. Aoki, M. Hirai, M. Shoda, Degradation pathway of an anthraquinone dye catalyzed by a unique peroxidase DyP from Thanatephorus cucumeris Dec 1, Biodegradation 20 (2009) 433-440.

[38] K.G. Welinder, J.M. Mauro, L. Norskov-Lauritsen, Structure of plant and fungal peroxidases, Biochem Soc Trans 20 (1992) 337-340.

[39] T. Yoshida, H. Tsuge, H. Konno, T. Hisabori, Y. Sugano, The catalytic mechanism of dye-decolorizing peroxidase DyP may require the swinging movement of an aspartic acid residue, The FEBS journal 278 (2011) 2387-2394.

[40] C. Zubieta, R. Joseph, S.S. Krishna, D. McMullan, M. Kapoor, H.L. Axelrod, M.D. Miller, P. Abdubek, C. Acosta, T. Astakhova, D. Carlton, H.J. Chiu, T. Clayton, M.C. Deller, L. Duan, Y. Elias, M.A. Elsliger, J. Feuerhelm, S.K. Grzechnik, J. Hale, G.W. Han, L. Jaroszewski, K.K. Jin, H.E. Klock, M.W. Knuth, P. Kozbial, A. Kumar, D. Marciano, A.T. Morse, K.D. Murphy, E. Nigoghossian, L. Okach, S. Oommachen, R. Reyes, C.L. Rife, P. Schimmel, C.V. Trout, H. van den Bedem, D. Weekes, A. White, Q.

Xu, K.O. Hodgson, J. Wooley, A.M. Deacon, A. Godzik, S.A. Lesley, I.A. Wilson, Identification and structural characterization of heme binding in a novel dye-decolorizing peroxidase, TyrA, Proteins 69 (2007) 234-243.

[41] M. Hofrichter, R. Ullrich, Heme-thiolate haloperoxidases: versatile biocatalysts with biotechnological and environmental significance, Appl Microbiol Biotechnol 71 (2006) 276-288.

[42] J.R. Beckwith, L.P. Hager, Biological Chlorination. Viii. Late Intermediates in the biosynthesis of caldariomycin, J Biol Chem 238 (1963) 3091-3094.

[43] J.R. Beckwith, R. Clark, L.P. Hager, Biological Chlorination. Vii. Studies on the biosynthesis of caldariomycin, J Biol Chem 238 (1963) 3086-3090.

[44] L.P. Hager, D.R. Morris, F.S. Brown, H. Eberwein, Chloroperoxidase. II. Utilization of halogen anions, J Biol Chem 241 (1966) 1769-1777.

[45] E.L. Patterson, W.W. Andres, L.A. Mitscher, Isolation of the bromo analogue of caldariomycin from Caldariomyces fumago, Appl Microbiol 15 (1967) 528-530.

[46] N. Itoh, Y. Izumi, H. Yamada, Characterization of nonheme iron and reaction mechanism of bromoperoxidase in Corallina pilulifera, J Biol Chem 262 (1987) 11982-11987.

[47] K. Kuhnel, W. Blankenfeldt, J. Terner, I. Schlichting, Crystal structures of chloroperoxidase with its bound substrates and complexed with formate, acetate, and nitrate, J Biol Chem 281 (2006) 23990-23998.

[48] M. Sundaramoorthy, J. Terner, T.L. Poulos, The crystal structure of chloroperoxidase: a heme peroxidase--cytochrome P450 functional hybrid, Structure 3 (1995) 1367-1377.

[49] E. Malle, P.G. Furtmuller, W. Sattler, C. Obinger, Myeloperoxidase: a target for new drug development?, Br J Pharmacol 152 (2007) 838-854.

[50] D.T. Akin, J.M. Kinkade, Jr., Processing of a newly identified intermediate of human myeloperoxidase in isolated granules occurs at neutral pH, J Biol Chem 261 (1986) 8370-8375.

[51] H.P. Koeffler, J. Ranyard, M. Pertcheck, Myeloperoxidase: its structure and expression during myeloid differentiation, Blood 65 (1985) 484-491.

[52] R. Wever, H. Plat, Spectral properties of myeloperoxidase and its ligand complexes, Biochim Biophys Acta 661 (1981) 235-239.

[53] J. Arnhold, E. Monzani, P.G. Furtmuller, M. Zederbauer, L. Casella, C. Obinger, Kinetics and thermodynamics of halide and nitrite oxidation by mammalian heme peroxidases, Eur J Inorg Chem (2006) 3801-3811.

[54] T.J. Fiedler, C.A. Davey, R.E. Fenna, X-ray crystal structure and characterization of halide-binding sites of human myeloperoxidase at 1.8 A resolution, J Biol Chem 275 (2000) 11964-11971.

[55] S. Shigeoka, T. Ishikawa, M. Tamoi, Y. Miyagawa, T. Takeda, Y. Yabuta, K. Yoshimura, Regulation and function of ascorbate peroxidase isoenzymes, J Exp Bot 53 (2002) 1305-1319.

[56] V.P. Skulachev, Cytochrome c in the apoptotic and antioxidant cascades, FEBS Lett 423 (1998) 275-280.

[57] J.E. Erman, L.B. Vitello, Yeast cytochrome c peroxidase: mechanistic studies via protein engineering, Biochim Biophys Acta 1597 (2002) 193-220.

[58] A.T. Martinez, M. Speranza, F.J. Ruiz-Duenas, P. Ferreira, S. Camarero, F. Guillen, M.J. Martinez, A. Gutierrez, J.C. del Rio, Biodegradation of lignocellulosics: microbial,

chemical, and enzymatic aspects of the fungal attack of lignin, Int Microbiol 8 (2005) 195-204.

[59] K. Piontek, A.T. Smith, W. Blodig, Lignin peroxidase structure and function, Biochem Soc Trans 29 (2001) 111-116.

[60] F. Passardi, D. Longet, C. Penel, C. Dunand, The class III peroxidase multigenic family in rice and its evolution in land plants, Phytochemistry 65 (2004) 1879-1893.

[61] M.A. Bernards, W.D. Fleming, D.B. Llewellyn, R. Priefer, X. Yang, A. Sabatino, G.L. Plourde, Biochemical characterization of the suberization-associated anionic peroxidase of potato, Plant Physiol 121 (1999) 135-146.

[62] S.D. Allison, J.C. Schultz, Differential activity of peroxidase isozymes in response to wounding, gypsy moth, and plant hormones in northern red oak (Quercus rubra L.), J Chem Ecol 30 (2004) 1363-1379.

[63] I.G. Gazaryan, L.M. Lagrimini, G.A. Ashby, R.N. Thorneley, Mechanism of indole-3-acetic acid oxidation by plant peroxidases: anaerobic stopped-flow spectrophotometric studies on horseradish and tobacco peroxidases, Biochem J 313 (Pt 3) (1996) 841-847.

[64] C. Mathe, A. Barre, C. Jourda, C. Dunand, Evolution and expression of class III peroxidases, Arch Biochem Biophys 500 (2010) 58-65.

[65] M. Gajhede, D.J. Schuller, A. Henriksen, A.T. Smith, T.L. Poulos, Crystal structure of horseradish peroxidase C at 2.15 A resolution, Nat Struct Biol 4 (1997) 1032-1038.

[66] T.G. Douroupi, I.S. Papassideri, D.J. Stravopodis, L.H. Margaritis, Molecular cloning and tissue-specific transcriptional regulation of the first peroxidase family member, Gene 362 (2005) 57-69.

[67] B. Lige, S. Ma, R.B. van Huystee, The effects of the site-directed removal of N-glycosylation from cationic peanut peroxidase on its function, Arch Biochem Biophys 386 (2001) 17-24.

[68] C. Gabaldon, L.V. Gomez-Ros, M.J. Nunez-Flores, A. Esteban-Carrasco, A.R. Barcelo, Post-translational modifications of the basic peroxidase isoenzyme from Zinnia elegans, Plant Mol Biol 65 (2007) 43-61.

[69] N.C. Veitch, Horseradish peroxidase: a modern view of a classic enzyme, Phytochemistry 65 (2004) 249-259.

[70] S. Nagano, M. Tanaka, K. Ishimori, Y. Watanabe, I. Morishima, Catalytic roles of the distal site asparagine-histidine couple in peroxidases, Biochemistry-Us 35 (1996) 14251-14258.

[71] H.S. Pappa, A.E. Cass, A step towards understanding the folding mechanism of horseradish peroxidase. Tryptophan fluorescence and circular dichroism equilibrium studies, Eur J Biochem 6 / FEBS 212 (1993) 227-235.

[72] A.T. Smith, N. Santama, S. Dacey, M. Edwards, R.C. Bray, R.N. Thorneley, J.F. Burke, Expression of a synthetic gene for horseradish peroxidase C in Escherichia coli and folding and activation of the recombinant enzyme with Ca^{2+} and heme, J Biol Chem 265 (1990) 13335-13343.

[73] H.B. Dunford., 1999. Heme peroxidases. Wiley-VCH, New York

[74] N.C.Veitch., Smith, A.T. 2001. Horseradish peroxidase. Adv. Inorg. Chem. 51, 107-162

[75] G.I. Berglund, G.H. Carlsson, A.T. Smith, H. Szoke, A. Henriksen, J. Hajdu, The catalytic pathway of horseradish peroxidase at high resolution, Nature 417 (2002) 463-468.

[76] T.K. Kirk, R.L. Farrell, Enzymatic "combustion": the microbial degradation of lignin, Annu Rev Microbiol 41 (1987) 465-505.

[77] D.W. Wong, Structure and action mechanism of ligninolytic enzymes, Appl Biochem Biotechnol 157 (2009) 174-209.

[78] K.E. Hammel, K.A. Jensen, Jr., M.D. Mozuch, L.L. Landucci, M. Tien, E.A. Pease, Ligninolysis by a purified lignin peroxidase, J Biol Chem 268 (1993) 12274-12281.

[79] M. Tien, T.K. Kirk, Lignin-Degrading Enzyme from the Hymenomycete Phanerochaete chrysosporium Burds, Science 221 (1983) 661-663.

[80] K. Valli, H. Wariishi, M.H. Gold, Oxidation of monomethoxylated aromatic compounds by lignin peroxidase: role of veratryl alcohol in lignin biodegradation, Biochemistry-Us 29 (1990) 8535-8539.

[81] T.L. Poulos, S.L. Edwards, H. Wariishi, M.H. Gold, Crystallographic refinement of lignin peroxidase at 2 A, J Biol Chem 268 (1993) 4429-4440.

[82] W. Blodig, W.A. Doyle, A.T. Smith, K. Winterhalter, T. Choinowski, K. Piontek, Autocatalytic formation of a hydroxy group at Cβ of trp171 in lignin peroxidase, Biochemistry-Us 37 (1998) 8832-8838.

[83] W.A. Doyle, W. Blodig, N.C. Veitch, K. Piontek, A.T. Smith, Two substrate interaction sites in lignin peroxidase revealed by site-directed mutagenesis, Biochemistry-Us 37 (1998) 15097-15105.

[84] W. Blodig, A.T. Smith, W.A. Doyle, K. Piontek, Crystal structures of pristine and oxidatively processed lignin peroxidase expressed in Escherichia coli and of the W171F variant that eliminates the redox active tryptophan 171. Implications for the reaction mechanism, J Mol Biol 305 (2001) 851-861.

[85] C.D. Millis, D.Y. Cai, M.T. Stankovich, M. Tien, Oxidation-reduction potentials and ionization states of extracellular peroxidases from the lignin-degrading fungus Phanerochaete chrysosporium, Biochemistry-Us 28 (1989) 8484-8489.

[86] M. Sundaramoorthy, K. Kishi, M.H. Gold, T.L. Poulos, Preliminary crystallographic analysis of manganese peroxidase from Phanerochaete chrysosporium, J Mol Biol 238 (1994) 845-848.

[87] M. Sundaramoorthy, K. Kishi, M.H. Gold, T.L. Poulos, Crystal structures of substrate binding site mutants of manganese peroxidase, J Biol Chem 272 (1997) 17574-17580.

[88] M. Perez-Boada, F.J. Ruiz-Duenas, R. Pogni, R. Basosi, T. Choinowski, M.J. Martinez, K. Piontek, A.T. Martinez, Versatile peroxidase oxidation of high redox potential aromatic compounds: site-directed mutagenesis, spectroscopic and crystallographic investigation of three long-range electron transfer pathways, J Mol Biol 354 (2005) 385-402.

[89] R. Pogni, M.C. Baratto, C. Teutloff, S. Giansanti, F.J. Ruiz-Duenas, T. Choinowski, K. Piontek, A.T. Martinez, F. Lendzian, R. Basosi, A tryptophan neutral radical in the oxidized state of versatile peroxidase from Pleurotus eryngii: a combined multifrequency EPR and density functional theory study, J Biol Chem 281 (2006) 9517-9526.

[90] M.H. Gold, H. Wariishi, K. Valli, Extracellular Peroxidases Involved in Lignin Degradation by the White Rot Basidiomycete Phanerochaete-Chrysosporium, Acs Sym Ser 389 (1989) 127-140.

[91] G.V. Reddy, M. Sridhar, M.H. Gold, Cleavage of nonphenolic beta-1 diarylpropane lignin model dimers by manganese peroxidase from Phanerochaete chrysosporium, Eur J Biochem / FEBS 270 (2003) 284-292.

[92] M. Zamocky, P.G. Furtmuller, C. Obinger, Evolution of structure and function of Class I peroxidases, Arch Biochem Biophys 500 (2010) 45-57.

[93] M.G. Klotz, P.C. Loewen, The molecular evolution of catalatic hydroperoxidases: evidence for multiple lateral transfer of genes between prokaryota and from bacteria into eukaryota, Mol Biol Evol 20 (2003) 1098-1112.

[94] I. Morgenstern, S. Klopman, D.S. Hibbett, Molecular evolution and diversity of lignin degrading heme peroxidases in the Agaricomycetes, J Mol Evol 66 (2008) 243-257.

[95] L.A. del Rio, F.J. Corpas, L.M. Sandalio, J.M. Palma, M. Gomez, J.B. Barroso, Reactive oxygen species, antioxidant systems and nitric oxide in peroxisomes, J Exp Bot 53 (2002) 1255-1272.

[96] A. Boveris, Acta Physiol. Latin. Am. 26 (1976) 31-37

[97] D.V. Dabir, E.P. Leverich, S.K. Kim, F.D. Tsai, M. Hirasawa, D.B. Knaff, C.M. Koehler, A role for cytochrome c and cytochrome c peroxidase in electron shuttling from Erv1, Embo J 26 (2007) 4801-4811.

[98] S.S. Giles, J.R. Perfect, G.M. Cox, Cytochrome c peroxidase contributes to the antioxidant defense of Cryptococcus neoformans, Fungal Genet Biol 42 (2005) 20-29.

[99] C.A. Bonagura, B. Bhaskar, H. Shimizu, H. Li, M. Sundaramoorthy, D.E. McRee, D.B. Goodin, T.L. Poulos, High-resolution crystal structures and spectroscopy of native and compound I cytochrome c peroxidase, Biochemistry-Us 42 (2003) 5600-5608.

[100] T.L. Poulos, Thirty years of heme peroxidase structural biology, Arch Biochem Biophys 500 (2010) 3-12.

[101] T.P. Barrows, B. Bhaskar, T.L. Poulos, Electrostatic control of the tryptophan radical in cytochrome c peroxidase, Biochemistry-Us 43 (2004) 8826-8834.

[102] M. Zamocky, Phylogenetic relationships in class I of the superfamily of bacterial, fungal, and plant peroxidases, Eur J Biochem 271 (2004) 3297-3309.

[103] B.C. Finzel, T.L. Poulos, J. Kraut, Crystal structure of yeast cytochrome c peroxidase refined at 1.7-A resolution, J Biol Chem 259 (1984) 13027-13036.

[104] K.H. Sharp, M. Mewies, P.C. Moody, E.L. Raven, Crystal structure of the ascorbate peroxidase-ascorbate complex, Nat Struct Biol 10 (2003) 303-307.

[105] Y. Zhang, B. Heym, B. Allen, D. Young, S. Cole, The catalase-peroxidase gene and isoniazid resistance of Mycobacterium tuberculosis, Nature 358 (1992) 591-593.

[106] S. Chouchane, I. Lippai, R.S. Magliozzo, Catalase-peroxidase (Mycobacterium tuberculosis KatG) catalysis and isoniazid activation, Biochemistry-Us 39 (2000) 9975-9983.

[107] B.F. Lei, C.J. Wei, S.C. Tu, Action mechanism of antitubercular isoniazid - Activation mycobacterium tuberculosis KatG, isolation, and characterization of InhA inhibitor, J Biol Chem 275 (2000) 2520-2526.

[108] C. Vilcheze, W.R. Jacobs, Jr., The mechanism of isoniazid killing: clarity through the scope of genetics, Annu Rev Microbiol 61 (2007) 35-50.

[109] X.B. Zhao, H. Yu, S.W. Yu, F. Wang, J.C. Sacchettini, R.S. Magliozzo, Hydrogen peroxide-mediated isoniazid activation catalyzed by Mycobacterium tuberculosis catalase-peroxidase (KatG) and its S315T mutant, Biochemistry-Us 45 (2006) 4131-4140.

[110] D.E. Minnikin, L. Kremer, L.G. Dover, G.S. Besra, The methyl-branched fortifications of Mycobacterium tuberculosis, Chem Biol 9 (2002) 545-553.

[111] E. Garcia, Y.A. Nedialkov, J. Elliott, V.L. Motin, R.R. Brubaker, Molecular characterization of KatY (Antigen 5), a thermoregulated chromosomally encoded catalase-peroxidase of Yersinia pestis, J Bacteriol 181 (1999) 3114-3122.

[112] R.J. Mehigh, R.R. Braubaker, Major stable peptides of Yersinia pestis synthesized during the low-calcium response, Infect Immun 61 (1993) 13-22.

[113] B.A. Chromy, M.W. Choi, G.A. Murphy, A.D. Gonzales, C.H. Corzett, B.C. Chang, J.P. Fitch, S.L. McCutchen-Maloney, Proteomic characterization of Yersinia pestis virulence, J Bacteriol 187 (2005) 8172-8180.

[114] P. Bandyopadhyay, B. Byrne, Y. Chan, M.S. Swanson, H.M. Steinman, Legionella pneumophila catalase-peroxidases are required for proper trafficking and growth in primary macrophages, Infect Immun 71 (2003) 4526-4535.

[115] G.A. Uhlich, C.Y. Chen, B.J. Cottrell, P.L. Irwin, J.G. Phillips, Peroxide resistance in Escherichia coli serotype O157 : H7 biofilms is regulated by both RpoS-dependent and -independent mechanisms, Microbiology 158 (2012) 2225-2234.

[116] G.A. Uhlich, KatP contributes to OxyR-regulated hydrogen peroxide resistance in Escherichia coli serotype O157 : H7, Microbiology 155 (2009) 3589-3598.

[117] V. Cannac-Caffrey, G. Hudry-Clergeon, Y. Petillot, J. Gagnon, G. Zaccai, B. Franzetti, The protein sequence of an archaeal catalase-peroxidase, Biochimie 80 (1998) 1003-1011.

[118] K.G. Welinder, Bacterial catalase-peroxidases are gene duplicated members of the plant peroxidase superfamily, Biochim Biophys Acta 1080 (1991) 215-220.

[119] Y. Yamada, T. Fujiwara, T. Sato, N. Igarashi, N. Tanaka, The 2.0 Å crystal structure of catalase-peroxidase from Haloarcula marismortui, Nat Struct Biol 9 (2002) 691-695.

[120] K. Wada, T. Tada, Y. Nakamura, T. Kinoshita, M. Tamoi, S. Shigeoka, K. Nishimura, Crystallization and preliminary X-ray diffraction studies of catalase-peroxidase from Synechococcus PCC 7942, Acta Crystallogr D Biol Crystallogr 58 (2002) 157-159.

[121] X. Carpena, S. Loprasert, S. Mongkolsuk, J. Switala, P.C. Loewen, I. Fita, Catalase-peroxidase KatG of Burkholderia pseudomallei at 1.7 Å resolution, J Mol Biol 327 (2003) 475-489.

[122] T. Bertrand, N.A. Eady, J.N. Jones, Jesmin, J.M. Nagy, B. Jamart-Gregoire, E.L. Raven, K.A. Brown, Crystal structure of Mycobacterium tuberculosis catalase-peroxidase, J Biol Chem 279 (2004) 38991-38999.

[123] H.A. Heering, C. Indiani, G. Regelsberger, C. Jakopitsch, C. Obinger, G. Smulevich, New insights into the heme cavity structure of catalase-peroxidase: A spectroscopic approach to the recombinant Synechocystis enzyme and selected distal cavity mutants, Biochemistry-Us 41 (2002) 9237-9247.

[124] C. Jakopitsch, M. Auer, G. Regelsberger, W. Jantschko, P.G. Furtmuller, F. Ruker, C. Obinger, The catalytic role of the distal site asparagine-histidine couple in catalase-peroxidases, Eur J Biochem 270 (2003) 1006-1013.

[125] C. Jakopitsch, M. Auer, G. Regelsberger, W. Jantschko, P.G. Furtmuller, F. Ruker, C. Obinger, Distal site aspartate is essential in the catalase activity of catalase-peroxidases, Biochemistry-Us 42 (2003) 5292-5300.

[126] C. Jakopitsch, E. Droghetti, F. Schmuckenschlager, P.G. Furtmuller, G. Smulevich, C. Obinger, Role of the main access channel of catalase-peroxidase in catalysis, J Biol Chem 280 (2005) 42411-42422.

[127] M. Zamocky, Q. Garcia-Fernandez, B. Gasselhuber, C. Jakopitsch, P.G. Furtmuller, P.C. Loewen, I. Fita, C. Obinger, X. Carpena, High conformational stability of secreted eukaryotic catalase-peroxidases -answers from first crystal structure and unfolding studies, J Biol Chem 2012.

[128] M. Zamocky, G. Regelsberger, C. Jakopitsch, C. Obinger, The molecular peculiarities of catalase-peroxidases, FEBS Lett 492 (2001) 177-182.

[129] Y.J. Li, D.C. Goodwin, Vital roles of an interhelical insertion in catalase-peroxidase bifunctionality, Biochem Biophys Res Commun 318 (2004) 970-976.

[130] S. N. Kudalkar, Roles of large loops in catalytic versatility of catalase-peroxidases: significance of peripheral structures in improvising enzyme functions (2012) Dissertation, Auburn University.

[131] T. Bertrand, N.A.J. Eady, J.N. Jones, J.M. Nagy, B. Jamart-Gregoire, E.L. Raven, K.A. Brown, Crystal structure of Mycobacterium tuberculosis catalase-peroxidase, J Biol Chem 279 (2004) 38991-38999.

[132] R.A. Ghiladi, G.M. Knudsen, K.F. Medzihradszky, P.R. Ortiz de Montellano, The Met-Tyr-Trp cross-link in Mycobacterium tuberculosis catalase-peroxidase (KatG): autocatalytic formation and effect on enzyme catalysis and spectroscopic properties, J Biol Chem 280 (2005) 22651-22663.

[133] C. Jakopitsch, D. Kolarich, G. Petutschnig, P.G. Furtmuller, C. Obinger, Distal side tryptophan, tyrosine and methionine in catalase-peroxidases are covalently linked in solution, FEBS Lett 552 (2003) 135-140.

[134] L.J. Donald, O.V. Krokhin, H.W. Duckworth, B. Wiseman, T. Deemagarn, R. Singh, J. Switala, X. Carpena, I. Fita, P.C. Loewen, Characterization of the catalase-peroxidase

KatG from Burkholderia pseudomallei by mass spectrometry, J Biol Chem 278 (2003) 35687-35692.

[135] R.A. Ghiladi, K.F. Medzihradszky, P.R. Ortiz de Montellano, Role of the Met-Tyr-Trp cross-link in Mycobacterium tuberculosis catalase-peroxidase (KatG) as revealed by KatG(M255I), Biochemistry-Us 44 (2005) 15093-15105.

[136] S.N. Kudalkar, R.A. Campbell, Y. Li, C.L. Varnado, C. Prescott, D.C. Goodwin, Enhancing the peroxidatic activity of KatG by deletion mutagenesis, J Inorg Biochem 116C (2012) 106-115.

[137] J. Vlasits, C. Jakopitsch, M. Bernroitner, M. Zamocky, P.G. Furtmuller, C. Obinger, Mechanisms of catalase activity of heme peroxidases, Arch Biochem Biophys 500 (2010) 74-81.

[138] X.B. Zhao, J. Suarez, A. Khajo, S.W. Yu, L. Metlitsky, R.S. Magliozzo, A radical on the met-tyr-trp modification required for catalase activity in catalase-peroxidase is established by isotopic labeling and site-directed mutagenesis, J Am Chem Soc 132 (2010) 8268.

[139] J. Suarez, K. Ranguelova, A.A. Jarzecki, J. Manzerova, V. Krymov, X.B. Zhao, S.W. Yu, L. Metlitsky, G.J. Gerfen, R.S. Magliozzo, An oxyferrous heme/protein-based radical intermediate is catalytically competent in the catalase reaction of mycobacterium tuberculosis catalase-peroxidase (KatG), J Biol Chem 284 (2009) 7017-7029.

[140] C. Jakopitsch, J. Vlasits, B. Wiseman, P.C. Loewen, C. Obinger, Redox intermediates in the catalase cycle of catalase-peroxidases from *Synechocystis PCC 6803, Burkholderia pseudomallei*, and *Mycobacterium tuberculosis*, Biochemistry-Us 46 (2007) 1183-1193.

[141] M. Zamocky, Phylogenetic relationships in class I of the superfamily of bacterial, fungal, and plant peroxidases, Eur J Biochem / FEBS 271 (2004) 3297-3309.

[142] R.D. Baker, C.O. Cook, D.C. Goodwin, Properties of catalase-peroxidase lacking its C-terminal domain, Biochem Biophys Res Commun 320 (2004) 833-839.

[143] X. Carpena, W. Melik-Adamyan, P.C. Loewen, I. Fita, Structure of the C-terminal domain of the catalase-peroxidase KatG from Escherichia coli, Acta Crystallogr D Biol Crystallogr 60 (2004) 1824-1832.

[144] R.D. Baker, C.O. Cook, D.C. Goodwin, Catalase-peroxidase active site restructuring by a distant and "inactive" domain, Biochemistry-Us 45 (2006) 7113-7121.

[145] S. Banerjee, M. Zamocky, P.G. Furtmuller, C. Obinger, Probing the two-domain structure of homodimeric prokaryotic and eukaryotic catalase-peroxidases, Biochim Biophys Acta 1804 (2010) 2136-2145.

[146] X. Carpena, J. Switala, S. Loprasert, S. Mongkolsuk, I. Fita, P.C. Loewen, Crystallization and preliminary X-ray analysis of the catalase-peroxidase KatG from Burkholderia pseudomallei, Acta Crystallogr D Biol Crystallogr 58 (2002) 2184-2186.

[147] J.A. Imlay, Cellular defenses against superoxide and hydrogen peroxide, Annu Rev Biochem 77 (2008) 755-776.

[148] P.C. Loewen, Bacterial catalases, Oxidative stress and the molecular biology of antioxidant defenses, Cold Spring Harbor Laboratory Press, New York, 1997

[149] C. Jakopitsch, M. Auer, A. Ivancich, F. Ruker, P.G. Furtmuller, C. Obinger, Total conversion of bifunctional catalase-peroxidase (KatG) to monofunctional peroxidase by exchange of a conserved distal side tyrosine, J Biol Chem 278 (2003) 20185-20191.

[150] S. Yu, S. Girotto, X. Zhao, R.S. Magliozzo, Rapid formation of compound II and a tyrosyl radical in the Y229F mutant of Mycobacterium tuberculosis catalase-peroxidase disrupts catalase but not peroxidase function, J Biol Chem 278 (2003) 44121-44127.

[151] Y. Li, D.C. Goodwin, Vital roles of an interhelical insertion in catalase-peroxidase bifunctionality, Biochem Biophys Res Commun 318 (2004) 970-976.

[152] S. More. "round-the-horn site-directed mutagensis-Openwetware, http://openwetware.org/wiki/%27Round-the-horn_site-directed_mutagenesis

[153] C.L. Varnado, K.M. Hertwig, R. Thomas, J.K. Roberts, D.C. Goodwin, Properties of a novel periplasmic catalase-peroxidase from Escherichia coli O157 : H7, Arch Biochem Biophys 421 (2004) 166-174.

[154] S.C. Gill, P.H. von Hippel, Calculation of protein extinction coefficients from amino acid sequence data, Anal Biochem 182 (1989) 319-326.

[155] J.E. Falk, Chromatography of Porphyrins and Metalloporphyrins, J Chromatogr 5 (1961) 277.

[156] S.L. Scott, W.J. Chen, A. Bakac, J.H. Espenson, Spectroscopic parameters, electrode-potentials, acid ionization-constants, and electron-exchange rates of the 2,2'-azinobis(3-ethylbenzothiazoline-6-sulfonate) radicals and ions, J Phys Chem-Us 97 (1993) 6710-6714.

[157] D.P. Nelson, L.A. Kiesow, Enthalpy of decomposition of hydrogen-peroxide by catalase at 25 degrees c, Anal Biochem 49 (1972) 474.

[158] A. Fersht, Structure and Mechanism in Protein Science: a Guide to Enzyme Catalysis and Proyein Folding. W.H. Freeman and Company, New York, 1999

[159] W.R.Hagen, Biomolecular EPR Spectroscopy, CRC Press, Boca Raton, FL, 2009

[160] W.R. Hagen,TU Delft: Biomolecular EPR Spectroscopy, http://www.bt.tudelft.nl/biomolecularEPRspectroscopy (2012)

[161] S.E. Jackson, A.R. Fersht, Folding of Chymotrypsin Inhibitor-2 .1. Evidence for a 2-State Transition, Biochemistry-Us 30 (1991) 10428-10435.

[162] C. Zentz, S. Pin, B. Alpert, Stationary and time-resolved circular-dichroism of hemoglobins, Method Enzymol 232 (1994) 247-266.

[163] G. Tsaprailis, D.W.S. Chan, A.M. English, Conformational states in denaturants of cytochrome c and horseradish peroxidases examined by fluorescence and circular dichroism, Biochemistry-Us 37 (1998) 2004-2016.

[164] M.R. Cheesman, C. Greenwood, A.J. Thomson, Magnetic Circular-Dichroism of Hemoproteins, Adv Inorg Chem Rad 36 (1991) 201-255.

[165] A. Ivancich, C. Jakopitsch, M. Auer, S. Un, C. Obinger, Protein-based radicals in the catalase-peroxidase of Synechocystis PCC6803: A multifrequency EPR investigation of wild-type and variants on the environment of the heme active site, J Am Chem Soc 125 (2003) 14093-14102.

[166] S. Chouchane, S. Girotto, S. Kapetanaki, J.P.M. Schelvis, S.W. Yu, R.S. Magliozzo, Analysis of heme structural heterogeneity in Mycobacterium tuberculosis catalase-peroxidase (KatG), J Biol Chem 278 (2003) 8154-8162.

[167] D.A. Svistunenko, J.A. Worrall, S.B. Chugh, S.C. Haigh, R.A. Ghiladi, P. Nicholls, Ferric haem forms of Mycobacterium tuberculosis catalase-peroxidase probed by EPR spectroscopy: Their stability and interplay with pH, Biochimie 94 (2012) 1274-1280.

[168] G.R. Sutherland, S.D. Aust, The effects of calcium on the thermal stability and activity of manganese peroxidase, Arch Biochem Biophys 332 (1996) 128-134.

[169] M. Sundaramoorthy, K. Kishi, M.H. Gold, T.L. Poulos, The crystal structure of manganese peroxidase from Phanerochaete chrysosporium at 2.06-A resolution, J Biol Chem 269 (1994) 32759-32767.

[170] Y. Nishizawa, Z. Nishio, K. Nakazono, M. Soma, E. Nakajima, M. Ugaki, T. Hibi, Enhanced resistance to blast (Magnaporthe grisea) in transgenic Japonica rice by constitutive expression of rice chitinase, Theoretical and Applied Genetics 99 (1999) 383-390.

[171] K. Soderhall, Special issue: Invertebrate immunity, Developmental and Comparative Immunology 23 (1999) 263-266.

[172] Y. Wang, D. Goodwin, Integral role of the I'-helix in the function of the "inactive" C-terminal domain of catalase-peroxidase (KatG). Biochimica et Biophysica Acta, 2012, In Press

[173] A. Fersht, Structure and Mechanism in Protein Science: a Guide to Enzyme Catalysis and Proyein Folding. W.H. Freeman and Company, New York, 1999

[174] J. Peterson, C. Vibat, R.B. Gennis, Identification of the axial heme ligands of cytochrome b556 in succinate: ubiquinone oxidoreductase from Escherichia coli, FEBS Lett, 355 (1994) 155-156.

[175] E.A. Berry, F.A. Walker, Bis-histidine-coordinated hemes in four-helix bundles: how the geometry of the bundle controls the axial imidazole plane orientations in transmembrane cytochromes of mitochondrial complexes II and III and related proteins, J. Biol. Inorg. Chem. 13 (2008) 481-498.

[176] G. Zoppellaro, K.L. Bren, A.A. Ensign, E. Harbitz, R. Kaur, H.P. Hersleth, U. Ryde, L. Hederstedt, K.K. Andersson, Review: studies of ferric heme proteins with highly

anisotropic/highly axial low spin (S = 1/2) electron paramagnetic resonance signals with bis-histidine and histidine-methionine axial iron coordination, Biopolymers 91 (2009) 1064-1082.

[177] G.R. Sutherland, L.S. Zapanta, M. Tien, S.D. Aust, Role of calcium in maintaining the heme environment of manganese peroxidase, Biochemistry-Us 36 (1997) 3654-3662.

[178] G. Nie, S.D. Aust, Spectral changes of lignin peroxidase during reversible inactivation, Biochemistry-Us 36 (1997) 5113-5119.

[179] G. Nie, S.D. Aust, Effect of calcium on the reversible thermal inactivation of lignin peroxidase, Arch Biochem Biophys 337 (1997) 225-231.

[180] D.J. Schuller, N. Ban, R.B. Huystee, A. McPherson, T.L. Poulos, The crystal structure of peanut peroxidase, Structure 4 (1996) 311-321.

[181] R. Moore, Toward the Understanding of Complex Biochemical Systems: the Significance of Global Protein Structure and Thorough Parametric Analysis 2008, Dissertation, Auburn University.

[182] A. Hillar, B. Peters, R. Pauls, A. Loboda, H. Zhang, A.G. Mauk, P.C. Loewen, Modulation of the activities of catalase-peroxidase HPI of Escherichia coli by site-directed mutagenesis, Biochemistry-Us 39 (2000) 5868-5875.

[183] G. Regelsberger, C. Jakopitsch, F. Ruker, D. Krois, G.A. Peschek, C. Obinger, Effect of distal cavity mutations on the formation of compound I in catalase-peroxidases, J Biol Chem 275 (2000) 22854-22861.

[184] J.E. Erman, L.B. Vitello, M.A. Miller, A. Shaw, K.A. Brown, J. Kraut, Histidine-52 is a critical residue for rapid formation of cytochrome-c peroxidase compound-I, Biochemistry-Us 32 (1993) 9798-9806.

[185] L.B. Vitello, J.E. Erman, M.A. Miller, J. Wang, J. Kraut, Effect of arginine-48 replacement on the reaction between cytochrome c peroxidase and hydrogen peroxide, Biochemistry-Us 32 (1993) 9807-9818.

[186] D.B. Goodin, D.E. McRee, The Asp-His-Fe triad of cytochrome c peroxidase controls the reduction potential, electronic structure, and coupling of the tryptophan free radical to the heme, Biochemistry-Us 32 (1993) 3313-3324.

[187] K.G. Welinder, B. Bjornholm, H.B. Dunford, Functions of electrostatic potentials and conserved distal and proximal His-Asp H-bonding networks in haem peroxidases, Biochem Soc Trans 23 (1995) 257-262.

[188] J.D. Satterlee, S.L. Alam, J.M. Mauro, J.E. Erman, T.L. Poulos, The effect of the Asn82-->Asp mutation in yeast cytochrome c peroxidase studied by proton NMR spectroscopy, Eur J Biochem / FEBS 224 (1994) 81-87.

[189] S.F. DeLauder, J.M. Mauro, T.L. Poulos, J.C. Williams, F.P. Schwarz, Thermodynamics of hydrogen cyanide and hydrogen fluoride binding to cytochrome c peroxidase and its Asn-82-->Asp mutant, Biochem J 302 (1994) 437-442.

[190] M. Tanaka, S. Nagano, K. Ishimori, I. Morishima, Hydrogen bond network in the distal site of peroxidases: spectroscopic properties of Asn70 --> Asp horseradish peroxidase mutant, Biochemistry-Us 36 (1997) 9791-9798.

[191] R.L. Moore, C.O. Cook, R. Williams, D.C. Goodwin, Substitution of strictly conserved Y111 in catalase-peroxidases: Impact of remote interdomain contacts on active site structure and catalytic performance, J Inorg Biochem. 102 (2008) 1819-1824.

[192] J.E. Erman, L.B. Vitello, M.A. Miller, A. Shaw, K.A. Brown, J. Kraut, Histidine 52 is a critical residue for rapid formation of cytochrome c peroxidase compound I, Biochemistry-Us 32 (1993) 9798-9806.

[193] N.L. Wengenack, M.P. Jensen, F. Rusnak, M.K. Stern, Mycobacterium tuberculosis KatG is a peroxynitritase, Biochem Biophys Res Commun, 256 (1999) 485-487.

[194] T. Sagawa, T. Yomo, S. Tsugawa, Y. Takeda, H. Ihara, E.K. Mitamura, I. Urabe, K. Ohkubo, A novel versatility of catalase I as a dioxygenase for indole-ring-opening dioxygenation, Chem Lett (1999) 339-340.

[195] P.C. Loewen (1997) Bacterial catalase. In Oxidative stress and the molecular biology of antioxidant defenses. pp 273-308, Cold Spring Harbor Laboratory Press, Plainview, N.Y

[196] E. Santoni, C. Jakopitsch, C. Obinger, G. Smulevich, Comparison between catalase-peroxidase and cytochrome c peroxidase. The role of the hydrogen-bond networks for protein stability and catalysis, Biochemistry-Us 43 (2004) 5792-5802.

[197] C. Jakopitsch, A. Ivancich, F. Schmuckenschlager, A. Wanasinghe, G. Poltl, P.G. Furtmuller, F. Ruker, C. Obinger, Influence of the unusual covalent adduct on the kinetics and formation of radical intermediates in synechocystis catalase peroxidase: a stopped-flow and EPR characterization of the MET275, TYR249, and ARG439 variants, J Biol Chem 279 (2004) 46082-46095.

[198] S.M. Kapetanaki, X.B. Zhao, S.W. Yu, R.S. Magliozzo, J.P.M. Schelvis, Modification of the active site of Mycobacterium tuberculosis KatG after disruption of the Met-Tyr-Trp cross-linked adduct, J Inorg Biochem 101 (2007) 422-433.

[199] C.L. Varnado, Enhancing expression of recombinant hemoproteins: progress toward understanding structure/function and therapeutic application (2006) Dissertation,

Auburn University.